



Swansea University
Prifysgol Abertawe

Dynamic Recrystallisation and Precipitation Kinetics of Haynes 282 During Thermal Processing

By

Luchao Liu

Faculty of Science and Engineering,

Swansea University, UK

Submitted to Swansea University in fulfilment of the requirements for
the Degree of Doctor of Philosophy

2023

Copyright: The Author, Luchao Liu, 2023.

Distributed under the terms of a Creative Commons Attribution 4.0 License
(CC BY 4.0).

Abstract

This PhD research work focused on the microstructural evolution during the thermal processing of a novel nickel-based superalloy Haynes 282. Two types of thermal processing methods, static heat treatment and dynamic hot compression test, were applied to Haynes 282 specimens. The static heat treatments, including nine treatments and a standard heat treatment, were conducted in the Carbolite CWF 1200 chamber furnace. Dynamic hot compression tests were conducted on a Gleeble 3500 system and consisted of nine tests with three different deformation temperatures and strain rates.

For static heat treatment, the grain size was characterised by optical and electron microscopy, and it was found that abnormal grain growth (AGG) was observed to dominate the early stage of grain growth for aging temperatures at 730°C and 830°C. Continuous grain growth (CGG) was observed in the later stage for aging temperature at 730°C and 830°C. No significant AGG was observed for aging temperature at 930°C.

The γ' precipitation analysis for static heat treatment was characterised by SEM and TEM. The results showed that the size of fine spherical γ' precipitates in standard treatment lay between 13.4nm-36.7nm with an average particle size of 22.0nm. For the designed treatments, in 730°C and 830°C groups, γ' size remained at a tertiary level while γ' evolved to secondary level in 930°C treatments. The precipitate coarsening correlated well with Ostwald Ripening theory and the size distribution correlated well with modified LSW models. Lastly, a diffusion-controlled coarsening mechanism which follows LSW theory was determined. And activation energy was calculated to be 238KJ/mol.

Specimens for dynamic hot compression test were characterised by optical camera and shadowgraph, and by SEM and EBSD. It was shown that elastic recovery occurred during the tests at 730°C and on samples deformed at 830°C with $0.05s^{-1}$ and $0.005s^{-1}$ strain rate. Regular stress-strain patterns were obtained from 930°C tests. However, the flow stress of 830°C tests acted differently, where it was larger at a lower strain rate in the early stage of deformation, while it acted opposite in the later stage. Besides, critical stress (σ_c) for 930°C was found at 519.5MPa, 345.3MPa and 300.5MPa for strain rate $0.05s^{-1}$, $0.005s^{-1}$ and $0.0005s^{-1}$ respectively. With respect to microstructural analysis, the grain size for 930°C was much smaller than other samples due to dynamic recrystallisation (DRX). According to grain orientation spread (GOS) maps, it was found that the recrystallisation level increases with the increases in temperature and with the decrease of strain rate. Eventually, geometrically necessary dislocation (GND) density was recorded, showing that GND tends to inhabit grain boundaries and GND density increased with the development of working hardening and initial DRX. GND was also found more sensitive to strain rate than deformation temperature.


Declaration

This work has not previously been accepted in substance for any degree and is not being concurrently submitted in candidature for any degree.

Signed..........

Date.....27/09/2022.....

This thesis is the result of my own investigations, except where otherwise stated. Other sources are acknowledged by footnotes giving explicit references. A bibliography is appended.

Signed..........

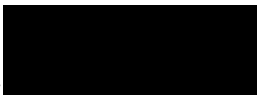
Date.....27/09/2022.....

I hereby give consent for my thesis, if accepted, to be available for photocopying and for inter-library loan, and for the title and summary to be made available to outside organisations.

Signed..........

Date.....27/09/2022.....

The University's ethical procedures have been followed and, where appropriate, that ethical approval has been granted.

Signed..........

Date.....27/09/2022.....

Contents Page

Abstract	ii
Declaration	iii
Contents Page.....	iv
Acknowledgement	vii
List of Tables.....	viii
List of Figures	x
Chapter 1 Introduction	1
Chapter 2 Literature Review	3
2.1 Nickel-based Superalloy	3
2.1.1 Chemical Composition of Nickel Alloys	4
2.1.2 Microstructures of Nickel Alloys.....	12
2.1.3 Defects in Nickel Alloys	17
2.1.4 Fatigue Property of Nickel Alloys	24
2.1.5 Creep Property of Nickel Alloys.....	26
2.1.6 Heat Treatments of Nickel Alloys.....	31
2.2 Nickel alloy Haynes 282.....	35
2.2.1 The Chemical Composition of Haynes 282	35
2.2.2 Metallurgical Microstructure	36
2.2.3 Heat Treatment.....	37
2.2.4 Applications	39
2.3 Microstructure Evolution and Modelling During Thermo-Mechanical Processing for Nickel-based Superalloy	40
2.3.1 Precipitation Evolution and Modelling.....	40
2.3.2 Grain Growth, Recovery and Recrystallisation	43
2.4 Summary.....	48

Chapter 3 Experimental Procedures.....	49
3.1 Materials Used	49
3.2 Static Heat Treatment.....	51
3.3 Dynamic Hot Compression Test	53
3.4 Metallographic Preparation.....	55
3.4.1 Cutting and Mounting	55
3.4.2 Grinding and Polishing	56
3.4.3 Etching and Further Polish.....	56
3.4.4 TEM Sample Preparation.....	59
3.5 Characterisation Techniques	61
3.5.1 Optical Microscope (OM).....	61
3.5.2 Scanning Electron Microscope (SEM)	62
3.5.3 Electron Backscattered Diffraction (EBSD)	63
3.5.4 Transmission Electron Microscope (TEM).....	65
3.6 Measurement Methods.....	67
3.6.1 Grain Size Measurement.....	67
3.6.2 Precipitation Measurement	71
Chapter 4 Results	73
4.1 Grain Evolution in Static Heat Treatments	73
4.2 Precipitation Coarsening in Static Heat Treatments	82
4.3 Dynamic Hot Compression.....	86
4.3.1 Mechanical Response.....	86
4.3.2 Grain Characterisation Results	91
Chapter 5 Discussion	93
5.1 Grain Size Evolution.....	93
5.2 Precipitation Coarsening Mechanism	95
5.3 Dynamic Recrystallisation	100

5.3.1 EBSD Analysis.....	102
5.3.2 GND Analysis	105
5.4 General Comments.....	109
Chapter 6 Conclusions	116
Chapter 7 Future Work.....	119
References.....	121

Acknowledgement

I would like to express my gratitude to my two major PhD supervisors, Prof. Soran Biroasca and Dr Will Harrison. Soran provided me with various research skill training and presentations and was always kind and patient with me. Will took over after Soran left the university and provided me with valuable advice and encouragement, particularly on Gleeble tests, which were crucial in completing my PhD work. He also guided me through the thesis writing process and made arrangements for my viva.

I am also thankful to the lab staff who provided me with equipment trainings and assistance, including Peter Davies, James Russell, Yubiao Niu, and Gareth Davies. AIM also deserves recognition for providing access to and management of the facilities.

I am grateful to my fellow PhD students. Thank Steve and Dane for the help and advice on Gleeble; Gang, Ali and Diween for the introduction in my first year.

Special thanks go to Rongsheng Cai, who assisted me with TEM works in Manchester, and Yuchen Gu, who shared his knowledge and laboratory consumables with me. Yuchen also recommended me for a part-time RA job, which provided valuable working experience during my PhD.

Lastly, I must acknowledge my parents for their unwavering support, both mentally and financially. Without their help, none of this would have been possible. I also want to express my deepest appreciation and love to my wife, Dr Yini Du, who has been my pillar of support throughout the pandemic and my PhD journey.

List of Tables

Table 2.1 The compositions (in weight%) of some common cast superalloys	7
Table 2.2 The compositions (in weight%) of some common wrought superalloys	9
Table 2.3 Role of alloying elements in Nickel superalloys	11
Table 2.4 Phases in Nickel Superalloys	13
Table 2.5 Chemical composition of CMSX-4 nickel superalloy	15
Table 2.6 Typical stress relieving and annealing cycles for wrought heat-resisting alloys. [7].	32
Table 2.7 Typical solution treating and aging cycles for wrought heat-resisting alloys	33
Table 2.8 Typical solution treating and aging cycles for some cast precipitation-hardened nickel-base superalloys	34
Table 3.1 Hot compression test parameters	53
Table 3.2 Chemical compositions of etchants.....	57
Table 3.3 Criteria to determine grain size in ASTM standards.....	67
Table 3.4 ASTM E112-13 Grain Size Relationships Computed for Uniform, Randomly Oriented, Equiaxed Grains[9]	71
Table 4.1 Values obtained and calculated in Jeffries Planimetric method	77
Table 4.2 Interception method results for 3 images	79
Table 4.3 Summary of interception method.....	79
Table 4.4 A further calculation using equation 3.7	79
Table 4.5 Summarised ASTM E112-13 grain size No. corresponding to Figure 4.7	81
Table 4.6 Precipitate measurements summary of 9 designed heat treatments	84
Table 4.7 Results of grain size calculated by interception method horizontally	92

Table 5.1 Activation energy for coarsening of γ' precipitates in similar nickel base alloys [24]	
.....	100
Table 5.2 SFE of metals and alloys at room temperature[32].	101

List of Figures

Figure 2.1 Face-centred cubic (FCC) structure.....	3
Figure 2.2 Crystal structure of Ni-Al system.....	12
Figure 2.3 Cuboidal γ' precipitates morphology of CMSX-4 superalloy [1]	15
Figure 2.4 Scanning electron microscopic image of the superalloy RR1000 showing extensive precipitation of the TCP phase.....	17
Figure 2.5 Label v represents the vacancy and label i represents a self-interstitial atom.....	18
Figure 2.6 The atom on the left is a substitutional atom and atom on the right is an interstitial atom.....	19
Figure 2.7 Schematic of (a) a cubic lattice; (b) positive edge dislocation line DC and extra half plane ABCD; (c) left-handed screw dislocation; (d) the helical atoms in screw dislocation ..	20
Figure 2.8 Transmission Electron Microscope image of CMSX-4 single-crystal superalloy, deformed to 0.04% strain in 1890 h at 750 °C and 450MPa. Note the localization of $\langle 110 \rangle \{111\}$ dislocation activity in a limited number of γ channels. The foil normal is $\{111\}$	22
Figure 2.9 Illustration of various faults possible in the	24
Figure 2.10 (a) image of a persistent slip band in a fatigued copper; (b) TEM image of persistent slip band in single crystal nickel alloy CMSX-4 fatigued at 850°C	26
Figure 2.11 Creep curves for nominally pure nickel tested at 371°C	28
Figure 2.12 Creep curves for nickel doped with a small fraction of particles ThO ₂ ; $\sigma = 28$ MPa. The time to rupture, T_r , is given for each creep curve	28
Figure 2.13 Variation of the (a) minimum creep rate and (b) life to rupture for several	

polycrystalline superalloys with varying fractions of the γ' phase.....	29
Figure 2.14 The relationships between the percentage difference in atomic size of solute and solvent atoms and the creep resistance at 500°C	30
Figure 2.15 Variation of the secondary creep rate of nickel with cobalt and chromium content during creep at 500°C	30
Figure 2.16 Typical microstructure of Haynes 282 alloy. (a) As solution annealed Haynes 282; (b) Aged Haynes 282 alloy	36
Figure 2.17 (a) SEM image of etched Haynes 282 alloy to highlight the grain boundary carbides after first step of the heat treatment cycle; (b) Haynes 282 etched to highlight the γ' phase after the second step of the heat treatment	37
Figure 2.18 Equilibrium phase diagram of Haynes 282 (a) diagram in normal temperature scale; (b) a magnified temperature scale diagram to show minor precipitate phases	38
Figure 2.19 Typical γ' crystal lattice created by CrystalMaker software showing a FCC structure with Ni atoms at centre and Al atoms at corner	40
Figure 2.20 Schematic for AGG and CGG occurring in annealed magnesium	44
Figure 2.21 Schematic illustrates the widely recognised categories of DRX and their difference	46
Figure 2.22 Histograms illustrate the difference between general hot deformation process with a DDRX controlled process, (a) and (b) show the single to multiple peaks when applying different deformation parameters.....	47
Figure 3.1 Diagram of parameters of ring-roll forged Haynes 282	50
Figure 3.2 Temperature drop during last pass of ring rolling process	50
Figure 3.3 Round and rectangular bar samples.....	50

Figure 3.4 Carbolite CWF 1200 laboratory chamber furnace	52
Figure 3.5 Schematics of post heat treatment, (a) Standard treatment; (b) Designed 1-step-aging treatment	52
Figure 3.6 Thermocouple welder	54
Figure 3.7 Barrelled samples	56
Figure 3.8 Kristall 680 Electrolytic Polisher and Etcher	57
Figure 3.9 Hitachi Broadbeam IM4000 Milling System and flat milling illustration	58
Figure 3.10 diagram of different situations and their preparation philosophies	59
Figure 3.11 Mechanical punch for cutting the disk	60
Figure 3.12 Julabo 900F external chiller and Tenupol-5 Twin-Jet polisher	61
Figure 3.13 Zeiss Primotech microscope(left) and Zeiss Compound microscope(right)	62
Figure 3.14 Schematic of set up of EBSD system	64
Figure 3.15 A spherical Kikuchi map and a flat Kikuchi pattern	65
Figure 3.16 FEI Talos F200X TEM/STEM system based in AIM Swansea University	66
Figure 3.17 example of Jeffries Planimetric Method[7]	69
Figure 3.18 A grain size comparison chart for ocular lens, used with a microscope[8].	69
Figure 3.19 Example of Heyn / Hilliard / Abrams Intercept Method with (a) grains counting and (b) grain boundaries counting	70
Figure 3.20 STEM bright field image of standard treatment sample	72
Figure 4.1 Optical images of (a) as-received sample with columnar grains; (b) sample solution treated at 1121°C for 30mins with equiaxed microstructure	74
Figure 4.2 Optical image revealing the grain evolution of standard heat treatment after solution treatment	75

Figure 4.3 (a) solutioned sample captured under SEM showing a microstructure free of boundary carbides; (b) grain boundary carbides and a large transgranular carbide spotted after standard heat treatment	75
Figure 4.4 Image of standard treated sample analysed by Jeffries Planimetric Method	76
Figure 4.5 Comparison method to determine the grain size	77
Figure 4.6 Image with interception line and red dots indicating grain boundary intersections	78
Figure 4.7 OM images of 9 1-step aging heat treatments, (a) 730°C/4h; (b)830°C/4h; (c) 930°C/4h; (d) 730°C/8h; (e) 830°C/8h; (f) 930°C/8h; (g) 730°C/16h ; (h) 830°C/16h; (i) 930°C/16h	80
Figure 4.8 Diagram of grain size evolution for 1-step heat treatments	82
Figure 4.9 SEM images of γ' morphology and distribution of 9 heat treatments(a) 730°C/4h; (b)830°C/4h; (c) 930°C/4h; (d) 730°C/8h; (e) 830°C/8h; (f) 930°C/8h; (g) 730°C/16h ; (h) 830°C/16h; (i) 930°C/16h	83
Figure 4.10 TEM characterization of γ' precipitates after 730°C aging process, (a) 4 hours; (b) 8 hours; (c) 16 hours	84
Figure 4.11 Precipitation size versus aging time with size distribution at different temperatures	85
Figure 4.12 Engineering stress-strain curve of hot compression tests at (a) 730°C, (b) 830°C, (c) 930°C	88
Figure 4.13 Work hardening rate against true stress at 930°C with different strain rate	89
Figure 4.14 Optical images of deformed samples	90
Figure 4.15 Shadowgraph data compares the shape of deformed samples with different strain	

rate at (a) 730°C; (b) 830°C; (c) 930°C.	90
Figure 4.16 Band contrast images of microstructure at centre of hot compression samples, rows from top to bottom corresponds to strain rate at 0.05s – 1, 0.005s – 1, 0.0005s – 1, and column from left to right corresponds deformation temperature at 730°C, 830°C, 930°C.	91
Figure 5.1 The effects of aging time on γ' precipitates size at different temperatures in logarithm	98
Figure 5.2 Arrhenius equation by plotting $\ln(K)$ versus $1/T$ illustrating precipitation growth in Haynes 282 alloy.....	99
Figure 5.3 IPF maps of microstructure at centre of hot compression samples, rows from top to bottom corresponds to strain rate at 0.05s – 1, 0.005s – 1, 0.0005s – 1, and column from left to right corresponds deformation temperature at 730°C, 830°C, 930°C.	103
Figure 5.4 Close-up images from 930°C tests at 0.05s – 1 strain rate, (a) IPF map; (b) Grain Orientation Spread (GOS) map.....	104
Figure 5.5 GOS maps showing the difference in grain orientation under different deformation temperature and strain rate.....	104
Figure 5.6 HUE histograms for GOS maps with yellow dot line separates recrystallised grain and sub-grains and dark dot line separates sub-grains with deformed grains.....	105
Figure 5.7 IPF and GND maps for strain rate of 0.05s – 1 and deformation temperature at (a) (b) 730°C, (c) (d) 830°C and (e) (f) 930°C respectively	107
Figure 5.8 The distribution of GND density at strain rate of 0.05s – 1, (a) 730°C; (b) 830°C; (c) 930°C.....	107
Figure 5.9 IPF and GND maps for deformation temperature of 830°C and strain rate at (a) (b) 0.05s – 1, (C) (d) 0.005s – 1 and (e) (f) 0.0005s – 1 respectively	108

Figure 5.10 The distribution of GND density at deformation temperature of 830°C and strain rate at (a) 0.05s – 1, (b) 0.005s – 1 and (c) 0.0005s – 1 respectively	108
Figure 5.11 Diagrams represent $\ln \varepsilon - \ln (\sigma)$ and $\ln \varepsilon - \sigma$ at different strain (0.1, 0.2, 0.3 and 0.4) were generated using Arrhenius-type constitutive modelling, Figure (a) (b) were drawn out of 930°C tests, which showed a linear relationship between strain rate and true stress; Figure (c) (d) were drawn out of 830°C tests, and these curves cannot provide constant slopes for further activation energy calculation.	115

Chapter 1 Introduction

In the last century, the demand for exploration of high-temperature materials raised with the rapid development of turbine engines for aircraft. Thereafter, in the 1950s, nickel-based superalloys first emerged and brought significant impact in the aerospace industry. The application of nickel-based superalloys in aerospace significantly improved the performance and capability of aircraft. As a higher-temperature material, nickel-based superalloy has a working temperature up to 800°C and is capable of application in the combustor and high-pressure compressor of a turbine engine. In addition, turbines are not only applied in aerospace industries but also in electricity generation plants. Similarly, the increase in population and electric appliances in the last century creates a huge amount of power consumption and has led to a soaring expenditure of coal fuel and carbon emissions. Therefore, the improvement of power generation efficiency is essential. The application of nickel-based superalloys in the turbine of power generators brought a unique impact in improving generation efficiency and decreasing carbon emissions. Consequently, the investigation of nickel-based superalloys is significant for energy conservation and sustainable development. Overall, in the presented works, the driving force of the investigation includes the understanding of the effects of thermal processing on microstructure evolution combined with commercial and economic concerns.

In this study, a newly developed nickel-based superalloy Haynes 282 was investigated. Haynes 282 was received from Rolls-Royce plc in a ring roll forged condition. And subsequently, two sets of samples were prepared, rectangular bars and round bars. Both sets of samples were subjected to solution treatment prior to static heat treatment and dynamic Gleeble hot compression tests for rectangular and round samples respectively. It should be noted that a rectangular sample was also prepared in as-received condition for comparison purposes. Sample preparations, static heat treatments and dynamic hot compression tests were carried out within the Material Research Centre (MRC) at Swansea University. Characterisations and post-data analysis were carried out with the assistance and management of the Advanced Imaging

of Materials (AIM). Techniques for characterisation included OM (optical microscope), SEM (scanning electron microscope), Energy Dispersive X-ray Spectroscopy (EDS), EBSD (electron backscattered diffraction) and TEM (transmission electron microscope).

The thesis consists of nine chapters. Chapter 1, introduction, briefly discusses the background of the importance of the application of nickel-based superalloys in the aerospace and power generation industry, research background and motivations and outlines the thesis layout. Chapter 2 is the literature review that gives the fundamental understanding of the topics involved in this thesis, e.g., the basic information of nickel-based superalloys, details about Haynes 282 superalloy and reviews of theories and research about thermal processing of nickel alloys. Experimental procedures are explained in Chapter 3. This chapter details the information on materials and methodologies used in experiments and tests. Furthermore, a comprehensive introduction of the characterisation technologies applied in this research is also reported. Chapter 4 and 5 present the results and discussion of static heat treatments and dynamic hot compression tests respectively. The investigation of grain evolution of Haynes 282 after static heat treatments is reported. In Chapter 4, the methods for grain size measurement are compared, and the results of grain size measurement are presented firstly. Followed by the description of precipitation size measurement and characterisation. Finally, the mechanical and microscopic results of dynamic hot compression tests are presented. Chapter 5 focuses on the discussion of grain evolution mechanism, γ' precipitation analysis and numerical modelling. Furthermore, the analysis of grain size evolution, grain misorientation spread analysis (GOS) and geometrically necessary dislocation (GND) are presented, and dynamic recrystallisation (DRX) mechanism is discussed. Subsequently, a general comment is placed to explain the contribution of this work compared to other researchers around the world. The main conclusions are highlighted again and summarised in Chapter 6. The suggestion for future work is given in Chapter 7 according to the limitations of current works and the achievements of other nickel-based superalloys from other research.

Chapter 2 Literature Review

2.1 Nickel-based Superalloy

Nickel is quite abundant on earth, which ranks behind Oxygen, Silicon, Aluminum and Iron and takes the fifth place. In the periodic table of elements, Nickel is placed at the first row of the D block of transition metals. Its atomic weight is 58.71 and its five stable isotopes are weighted at 58,60,61,62 and 64 and take up 67.7%, 26.2%, 1.25%, 3.66% and 1.16%, respectively. [1]

From room temperature to melting point, 1455 °C, nickel exhibits a face-centred cubic (FCC), see Figure 2.1. This determines the limitation of the temperature capability of nickel and its alloy.

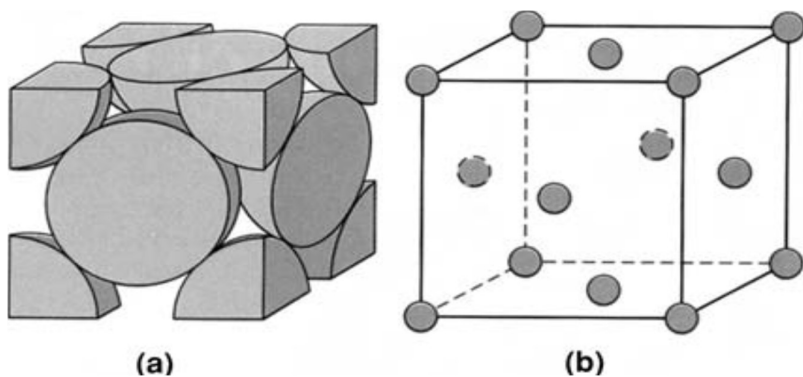


Figure 2.1 Face-centred cubic (FCC) structure [1]

The density of nickel under ambient conditions is 8907 kg/m^3 . Thus, compared with other metals used for aerospace applications, for example, Ti (4508 kg/m^3) and Al (2698 kg/m^3), nickel is quite dense. This is a consequence of a small interatomic distance, arising from the strong cohesion provided by the outer d electrons – a characteristic of the transition metals.

2.1.1 Chemical Composition of Nickel Alloys

The composition of some nickel-based superalloys can be seen in Tables 2.1 (cast alloys) and 2.2 (wrought alloys), there are more than ten elements that can be found in those superalloys[1]. However, many regularities can be identified despite of the complex nature of nickel-based alloys. Chromium, cobalt, aluminium and titanium take up a significant percentage, and a small amount of boron, zirconium, and carbon are also contained in the superalloys. Besides, rhenium, tungsten, tantalum, hafnium, ruthenium, molybdenum and niobium are also included, but not in all superalloys. Some alloys such as Incoloy800, Incoloy801, Incoloy802 and Incoloy706 include a significant amount of iron, thus they are referred to as nickel-iron superalloys. Table 2.3 listed the role of alloying elements and details are presented below.

Three groups of elements can be categorised according to the phase where these elements stabilize [1,2].

- (1) The first group of elements contains cobalt, chromium, molybdenum, ruthenium and rhenium. These elements are preferred to stabilize in the gamma phase, denoted γ , and they exhibit an FCC structure. The gamma phase is a continuous matrix phase and other phases will reside within it. Moreover, in nearly all cases, these elements act as solid solution strengtheners in γ phase and they have similar atomic radii to that of nickel.
- (2) The second group of elements includes aluminium, titanium and tantalum. These elements have larger atomic radii than nickel. And these elements combined with nickel form the gamma prime (γ') phase which is precipitated in γ phase. Besides, the phase that is rich in niobium will form a γ'' phase instead of γ' phase.
- (3) The third group of elements are titanium, tantalum and hafnium. And these elements combine with carbon will form MC carbides, combines with boron to form borides. Both MC carbides and borides will reside on the γ grain boundary.

The roles of chemical elements in nickel alloys are provided below:

Cobalt can be found in many Nickel-based superalloys, such as Haynes 282, Inconel 740H, Waspaloy and Haynes 263. As listed in Table 2.3, Cobalt is an important solid-solution strengthener element and provides alloys with desired elevated temperature properties and corrosion (sulfidation) resistant properties. Besides, Cobalt can benefit the controlling the solvus temperature of γ' , which will maintain the alloy's thermal stability.

Chromium plays an important role in environmental degradation resistance in all true superalloys. By forming Cr_2O_3 , Cr can provide superalloys with the resistance of oxidation and hot corrosion. The amount of Cr in superalloys is limited by the propensity of the σ TCP phase. According to the information provided in Tables 2.1 and 2.2, the weight percentage of Cr in various nickel-based alloys ranges from 2% (CMSX-6, CMSX-10, and PWA1497) to 23% (Inconel 690). Typically, nickel-based superalloys contain chromium content within the range of 6 to 22 wt%. Chromium is the major element that can provide hot corrosion resistance, but Titanium and other elements may supplement the Chromium effects [3,4].

Molybdenum strengthens the γ phase and aids creep resistance due to its faster diffusion than Ni. Mo is a TCP former and can also be detrimental to oxidation. Mo lowers the solvus temperature significantly when substituted for Tungsten. This suggests that Mo acts as a γ -stabilizer. However, opposing findings showed Mo and V moderately increase γ' solvus temperature and both stabilize the γ' -phase [5].

Niobium is the weakest of the γ' formers but is often added due to its benefit to oxidation resistance as grain boundary δ -phase acts as a diffusion barrier. Additions of Nb also stabilise the γ' phase in a similar way to that of Ta. Meanwhile, Nb additions need to be carefully considered to deter the formation of the delta (δ) phase.

Titanium is also a strong γ' former and can readily replace Al as a substitutional strengthener. When titanium is added to nickel alloys, it forms a solid solution with the nickel matrix, resulting in the strengthening of the alloy. This strengthening effect is due to the size and chemical similarity between titanium and nickel atoms, which allows titanium atoms to substitute for some of the nickel atoms in the crystal lattice [1,7]. Ti has also been seen to improve mechanical properties. High additions of the element can decrease the material's melting temperature and are detrimental to the oxidation resistance through the formation of rutile TiO₂ [6].

Aluminium is the most important partitioning element for γ' formation as both Ni and Al elements have the same crystal structure and can be exchanged mutually in a solid solution. As can be seen in Table 2.3, the roles of Al in nickel-based alloys include providing oxidation resistance, hardening precipitates and/or intermetallics and forming γ' Ni-Al system. Furthermore, the Ni-Al system is an FCC structure and exists in numerous solid phases.

The characteristics of Ni-Al system are outlined below:

- (1) A significant degree of directional, covalent bonding which gives a precise stoichiometric relationship between the number of nickel and aluminium atoms in each cell.
- (2) A phase which contains Ni-Al crystals structures rather than Ni-Ni or Al-Al. This results in a strong chemical order where typical structures include Ni_3Al , $NiAl$, Ni_2Al_3 , $NiAl_3$ and Ni_2Al_9 . The γ' phase generally takes the form of which is Ni_3Al , of ordered $L1_2$ with Al at the corners.

The ordered nature of the precipitate phase was reviewed when the ternary phase has a composition of Ni-Al-X, in which X represents an element, for example, Co, Cr, Mo or W. For this ordered structure the γ' is extended in a direction which depends highly on the solubility of the element X in the γ' phase.

Other elements that can be used in Nickel alloys also play an important role in strengthening mechanical properties. Details are shown in the Table 2.3.

Table 2.1 The compositions (in weight%) of some common cast superalloys [1]

Alloy	Cr	Co	Mo	W	Al	Ti	Ta	Nb	Re	Ru	Hf	C	B	Zr	Ni
AM1	7.0	8.0	2.0	5.0	5.0	1.8	8.0	1.0	—	—	—	—	—	—	Bal
AM3	8.0	5.5	2.25	5.0	6.0	2.0	3.5	—	—	—	—	—	—	—	Bal
CM186LC	6.0	9.3	0.5	8.4	5.7	0.7	3.4	—	3.0	—	1.4	0.07	0.015	0.005	Bal
CM247LC	8.0	9.3	0.5	9.5	5.6	0.7	3.2	—	—	—	1.4	0.07	0.015	0.010	Bal
CMSX-2	8.0	5.0	0.6	8.0	5.6	1.0	6.0	—	—	—	—	—	—	—	Bal
CMSX-3	8.0	4.8	0.6	8.0	5.6	1.0	6.3	—	—	—	0.1	—	—	—	Bal
CMSX-4	6.5	9.6	0.6	6.4	5.6	1.0	6.5	—	3.0	—	0.1	—	—	—	Bal
CMSX-6	10.0	5.0	3.0	—	4.8	4.7	6.0	—	—	—	0.1	—	—	—	Bal
CMSX-10	2.0	3.0	0.4	5.0	5.7	0.2	8.0	—	6.0	—	0.03	—	—	—	Bal
EPM-102	2.0	16.5	2.0	6.0	5.55	—	8.25	—	5.95	3.0	0.15	0.03	—	—	Bal
GTD-111	14.0	9.5	1.5	3.8	3.0	5.0	3.15	0.07	—	—	—	0.10	0.014	0.007	Bal
GTD-222	22.5	19.1	—	2.0	1.2	2.3	0.94	0.8	—	—	—	0.08	0.004	0.02	Bal
IN100	10.0	15.0	3.0	—	5.5	4.7	—	—	—	—	—	0.18	0.014	0.06	Bal
IN-713LC	12.0	—	4.5	—	5.9	0.6	—	2.0	—	—	—	0.05	0.01	0.10	Bal
IN-738LC	16.0	8.5	1.75	2.6	3.4	3.4	1.75	0.9	—	—	—	0.11	0.01	0.04	Bal
IN-792	12.4	9.2	1.9	3.9	3.5	3.9	4.2	—	—	—	—	0.07	0.016	0.018	Bal
IN-939	22.4	19.0	—	2.0	1.9	3.7	—	1.0	—	—	—	0.15	0.009	0.10	Bal
Mar-M002	8.0	10.0	—	10.0	5.5	1.5	2.6	—	—	—	1.5	0.15	0.015	0.03	Bal
Mar-M246	9.0	10.0	2.5	10.0	5.5	1.5	1.5	—	—	—	1.5	0.15	0.015	0.05	Bal
Mar-M247	8.0	10.0	0.6	10.0	5.5	1.0	3.0	—	—	—	1.5	0.15	0.015	0.03	Bal
Mar-M200Hf	8.0	9.0	—	12.0	5.0	1.9	—	1.0	—	—	2.0	0.13	0.015	0.03	Bal
Mar-M421	15.0	10.8	1.8	3.3	4.5	1.6	—	2.3	—	—	—	0.18	0.019	0.04	Bal
MC2	8.0	5.0	2.0	8.0	5.0	1.5	6.0	—	—	—	0.1	—	—	—	Bal
MC-NG	4.0	—	1.0	5.0	6.0	0.5	5.0	—	4.0	4.0	0.1	—	—	—	Bal
MX4	2.0	16.5	2.0	6.0	5.55	—	8.25	—	5.95	3.0	0.15	0.03	—	—	Bal

Table 2.1 (cont.)

Alloy	Cr	Co	Mo	W	Al	Ti	Ta	Nb	Re	Ru	Hf	C	B	Zr	Ni

Table 2.2 The compositions (in weight%) of some common wrought superalloys [1]

Alloy	Cr	Co	Mo	W	Nb	Al	Ti	Ta	Fe	Hf	C	B	Zr	Ni
Alloy 10	11.5	15	2.3	5.9	1.7	3.8	3.9	0.75	—	—	0.030	0.020	0.05	Bal
Astroloy	15.0	17.0	5.3	—	—	4.0	3.5	—	—	—	0.06	0.030	—	Bal
C-263	16	15	3	1.25	—	2.50	5.0	—	—	—	0.025	0.018	—	Bal
Hastelloy S	15.5	—	14.5	—	—	0.3	—	—	1.0	—	—	0.009	—	Bal
Hastelloy X	22.0	1.5	9.0	0.6	—	0.25	—	—	18.5	—	0.10	—	—	Bal
Haynes 230	22.0	—	2.0	14.0	—	0.3	—	—	—	—	0.10	—	—	Bal
Haynes 242	8.0	2.5	25.0	—	—	0.25	—	—	2.0	—	0.15	0.003	—	Bal
Haynes R-41	19.0	11.0	10.0	—	—	1.5	3.1	—	5.0	—	0.09	0.006	—	Bal
Incoloy 800	21.0	—	—	—	—	0.38	0.38	—	45.7	—	0.05	—	—	Bal
Incoloy 801	20.5	—	—	—	—	—	1.13	—	46.3	—	0.05	—	—	Bal
Incoloy 802	21.0	—	—	—	—	0.58	0.75	—	44.8	—	0.35	—	—	Bal
Incoloy 909	—	13.0	—	—	4.7	0.03	1.5	—	42.0	—	0.01	—	—	Bal
Incoloy 925	20.5	—	—	—	—	0.20	2.1	—	29.0	—	0.01	—	—	Bal
Inconel 600	15.5	—	—	—	—	—	—	—	8.0	—	0.08	—	—	Bal
Inconel 601	23.0	—	—	—	—	1.4	—	—	14.1	—	0.05	—	—	Bal
Inconel 617	22.0	12.5	9.0	—	—	1.0	0.3	—	—	—	0.07	—	—	Bal
Inconel 625	21.5	—	9.0	—	3.6	0.2	0.2	—	2.5	—	0.05	—	—	Bal
Inconel 690	29.0	—	—	—	—	—	—	—	9.0	—	0.025	—	—	Bal
Inconel 706	16.0	—	—	—	2.9	0.2	1.8	—	40.0	—	0.03	—	—	Bal
Inconel 718	19.0	—	3.0	—	5.1	0.5	0.9	—	18.5	—	0.04	—	—	Bal
Inconel 738	16.0	8.5	1.75	2.6	0.9	3.4	3.4	1.7	—	—	0.11	0.01	0.05	Bal
Inconel 740	25.0	20.0	0.5	—	2.0	0.9	1.8	—	0.7	—	0.03	—	—	Bal
Inconel X750	15.5	—	—	—	1.0	0.7	2.5	—	7.0	—	0.04	—	—	Bal
LSHR	13	21	2.7	4.3	1.5	3.5	3.5	1.6	—	—	0.030	0.030	0.050	Bal
ME3	13.1	18.2	3.8	1.9	1.4	3.5	3.5	2.7	—	—	0.030	0.030	0.050	Bal
MERL-76	12.4	18.6	3.3	—	1.4	0.2	4.3	—	—	0.35	0.050	0.03	0.06	Bal
Nimonic 75	19.5	—	—	—	—	—	0.4	—	3.0	—	0.10	—	—	Bal
Nimonic 80A	19.5	—	—	—	—	1.4	2.4	—	—	—	0.06	0.003	0.06	Bal
Nimonic 90	19.5	16.5	—	—	—	1.5	2.5	—	—	—	0.07	0.003	0.06	Bal
Nimonic 105	15.0	20.0	5.0	—	—	4.7	1.2	—	—	—	0.13	0.005	0.10	Bal
Nimonic 115	14.3	13.2	—	—	—	4.9	3.7	—	—	—	0.15	0.160	0.04	Bal
Nimonic 263	20.0	20.0	5.9	—	—	0.5	2.1	—	—	—	0.06	0.001	0.02	Bal
Nimonic 901	12.5	—	5.75	—	—	0.35	2.9	—	—	—	0.05	—	—	Bal

Table 2.2 (cont.)

Alloy	Cr	Co	Mo	W	Nb	Al	Ti	Ta	Fe	Hf	C	B	Zr	Ni
Waspaloy	19.5	19.5	4.5	—	—	1.5	5.0	—	—	—	0.08	0.008	—	0.01

Table 2.3 Role of alloying elements in Nickel superalloys [7]

Effect(a)	Iron-base	Cobalt-base	Nickel-base
Solid-solution strengtheners	Cr, Mo	Nb, Cr, Mo, Ni, W, Ta	Co, Cr, Fe, Mo, W, Ta, Re
fcc matrix stabilizers	C, W, Ni	Ni	...
Carbide form:			
MC	Ti	Ti	W, Ta, Ti, Mo, Nb, Hf
M ₇ C ₃	...	Cr	Cr
M ₂₃ C ₆	Cr	Cr	Cr, Mo, W
M ₆ C	Mo	Mo, W	Mo, W, Nb
Carbonitrides: M(CN)	C, N	C, N	C, N
Promotes general precipitation of carbides	P
Forms γ' Ni ₃ (Al, Ti)	Al, Ni, Ti	...	Al, Ti
Retards formation of hexagonal η (Ni ₃ Ti)	Al, Zr
Raises solvus temperature of γ'	Co
Hardening precipitates and/or intermetallics	Al, Ti, Nb	Al, Mo, Ti(b), W, Ta	Al, Ti, Nb
Oxidation resistance	Cr	Al, Cr	Al, Cr, Y, La, Ce
Improve hot corrosion resistance	La, Y	La, Y, Th	La, Th
Sulfidation resistance	Cr	Cr	Cr, Co, Si
Improves creep properties	B	...	B, Ta
Increases rupture strength	B	B, Zr	B(c)
Grain-boundary refiners	B, C, Zr, Hf
Facilitates working	...	Ni ₃ Ti	...
Retard γ' coarsening	Re

(a) Not all these effects necessarily occur in a given alloy. (b) Hardening by precipitation of Ni₃Ti also occurs if sufficient Ni is present. (c) If present in large amounts, borides are formed.

2.1.2 Microstructures of Nickel Alloys

The microstructure of nickel and its superalloys vary according to different chemical compositions. Table 2.4 shows the details of the phase that can be observed in nickel-based superalloy. Generally, there are three main phases that can be found in a Nickel-based superalloy, described below.

The Gamma Phase

The gamma phase or γ phase, is a disordered and matrix phase of nickel-based alloys. A high percentage of solid-solution elements can be found in this phase, such as cobalt, iron, chromium, molybdenum, and tungsten [7]. The stability of the γ phase is important since any phase transformations will lead to a poor elevated temperature property.

The Gamma Prime Phase

The γ' phase, also known as the Gamma prime phase, is a structured phase resulting from aluminium and titanium precipitation reaction with nickel [7]. Typically, it has coherence with the γ matrix and is crucial for enhancing the high-temperature capabilities of nickel-based superalloys. Additionally, it plays a vital role in strengthening these alloys. The γ' phase has a notable characteristic of the Ni-Al system, in which Nickel atoms are located in the cell face centre and aluminium atoms are at the cell corners (see figure 2.2). This crystal structure is also noted as $L1_2$. Although, the Ni-Al system exhibits multiple combinations except Ni-Al such as Ni-Ni and Al-Al, the Ni-Al crystal structure is preferred. Therefore, the γ' phase is referred to as the ordered phase distinguished from the disordered γ phase (FCC phase).

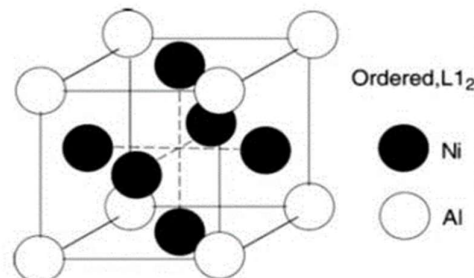
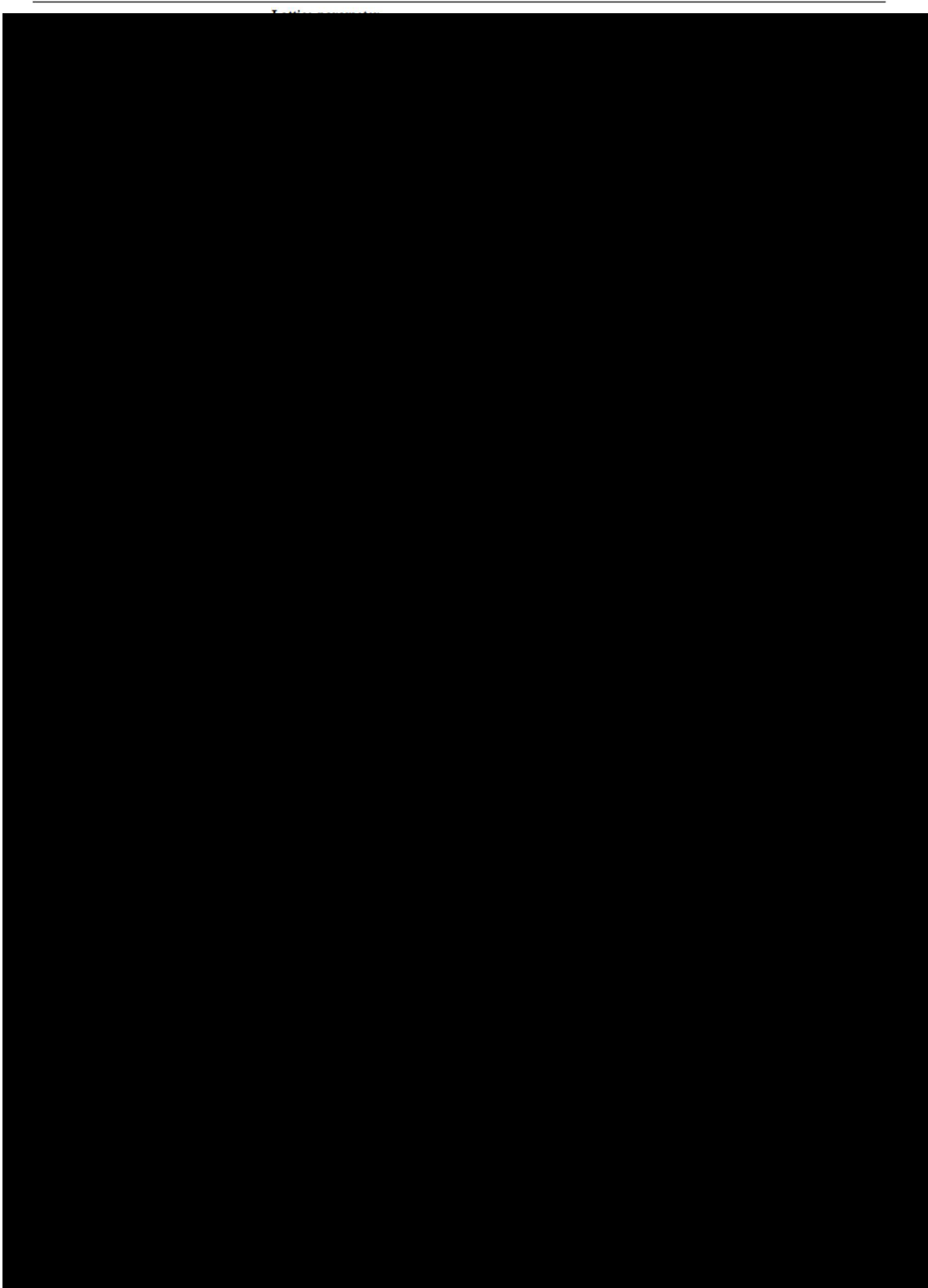


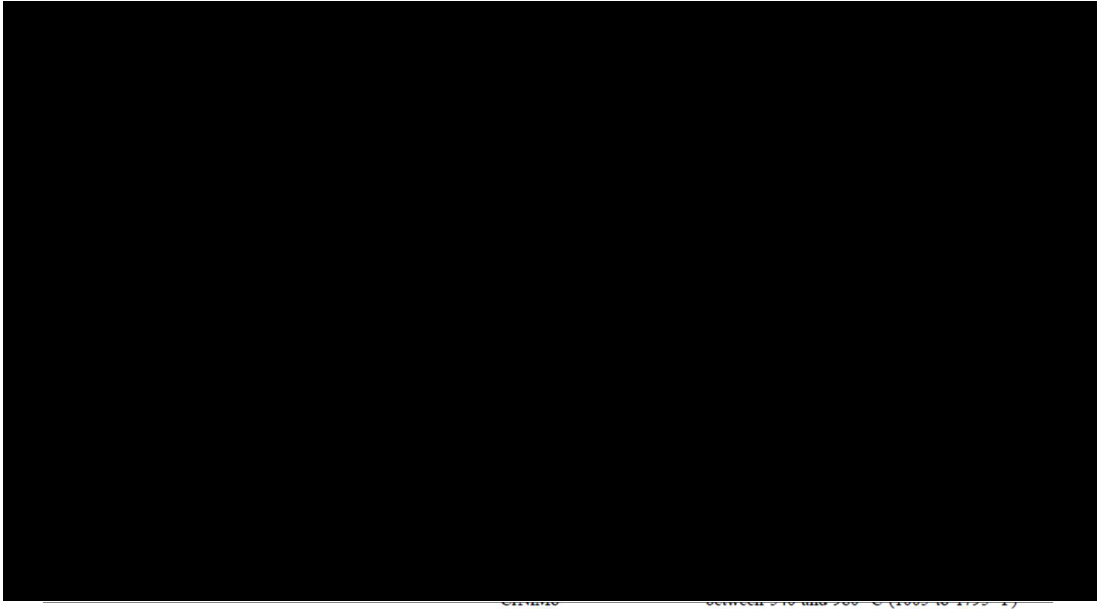
Figure 2.2 Crystal structure of Ni-Al system [1]

Table 2.4 Phases in Nickel Superalloys [7]



(continued)

Table 2.4 Cont.



As described in Table 2.4, The morphology of γ' phase varies from spherical to cuboidal. Spherical shape γ' phase can be found in some older iron-nickel superalloys such as Nimonic 80A and Wasploy. And in recently developed Nickel-based superalloys, the γ' phase is generally cuboidal. Previous experiments had shown that the variation in shapes is caused by the molybdenum concentration and the ratio of aluminium/titanium. In summary, the higher the percentage of γ' strengthening elements such as Al, Ti and Ta, the higher of γ' fraction and the more likely γ' would exhibit a cuboidal morphology. An illustration is CMSX-4, a nickel-based superalloy recognised for its relatively high concentration of γ' strengthening elements, comprising 6.5wt% Ta, 5.6wt% Al, and 1.0wt% Ti. Detailed information regarding these compositional proportions can be found in Table 2.5, while Figure 2.3 provides further illustration of its γ' morphology. Moreover, the shape of γ' evolves in a sequence of spherical>globular>blocky>cuboidal with the increase of γ/γ' misfit [1,7]. The research of Ricks et al. [8] investigated the formation of γ' precipitates in various nickel-based superalloys during heat treatment. They observed a sequence of morphological changes that progressed from spheres to cubes, arrays of cubes, and eventually solid-state dendrites as coarsening occurred due to aging. The authors found no significant difference in the morphology

development between positive and negative misfitting alloys. However, negative misfitting alloys showed better-defined $\{001\}$ facets, and interfacial dislocation networks developed earlier in the γ' growth sequence. Interestingly, the size at which the γ' particles deviate from the spherical shape and the heat treatment severity required to form cuboidal arrays depend on the lattice misfit. Therefore, the particle size needs to be larger for low misfit alloys before the effects of misfit strain can influence the particle shape.

Besides, the crystal structure, lattice parameters and chemical composition of other phases in Nickel-based superalloys are also given in this table.

Table 2.5 Chemical composition of CMSX-4 nickel superalloy

Element	Ni	Co	Cr	Ta	W	Al	Re	Ti	Mo	Hf
(wt%)	60	9.6	6.5	6.5	6.4	5.6	3.0	1.0	0.6	0.1

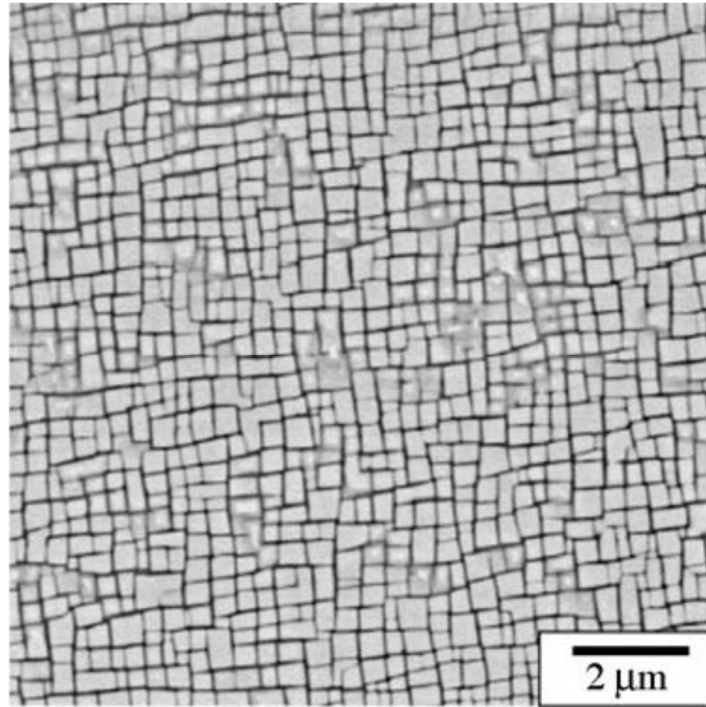


Figure 2.3 Cuboidal γ' precipitates morphology of CMSX-4 superalloy [1]

Carbides and Borides.

Carbon usually takes up 0.2wt% in nickel-based superalloys and it combines with some reactive elements like titanium, tantalum and hafnium to form metal carbides (MC). After heat treatment and service, MC is likely to decompose and generate other carbides such as $M_{23}C_6$ and M_6C , which often form at the grain boundaries. Borides are formed through the combination of elements such as chromium or molybdenum. Also, borides tend to segregate to the γ phase grain boundaries. Generally speaking, small amounts of borides are beneficial to creep-rupture property.

Other phases including gamma double prime phase (γ'' phase), TCP (topologically close-packed) phase etc.

γ'' phase can be found in a few Nickel-Iron superalloys such as IN718 and IN706, which is normally nickel combined with niobium. In this kind of alloy, the strengthening precipitate is body-centred tetragonal (BCT) ordered compound rather than γ' [1]. γ'' phase has high strength at low-to-intermediate temperatures, but when the temperature goes up to 1200 °F (649°C), γ'' phase will become unstable.

The TCP phase is characterised by a unique atomic arrangement where the atoms are closely packed. It can be both beneficial and detrimental to the alloy depending on the specific application and alloy composition. Figure 2.4 gives an example of grain boundary TCP phase. Effects caused by grain boundary TCP phase includes embrittlement, intergranular corrosion, decreased grain cohesion and reduced mechanical properties.[1]

It is worth mentioning that excessive quantities of Cr, Mo, W and Re promote the precipitation of intermetallic phases which are rich in these elements. The resulting phases have a number of distinct characteristics:

- (1) A high and uniform packing density of atoms;
- (2) A degree of non-metallic, directional bonding;
- (3) Complex crystal structures, each built up of distinct tessellated layers consisting of

arrays of hexagons, pentagons and triangles stacked into a limited number of so-called Kasper co-ordination polyhedral.

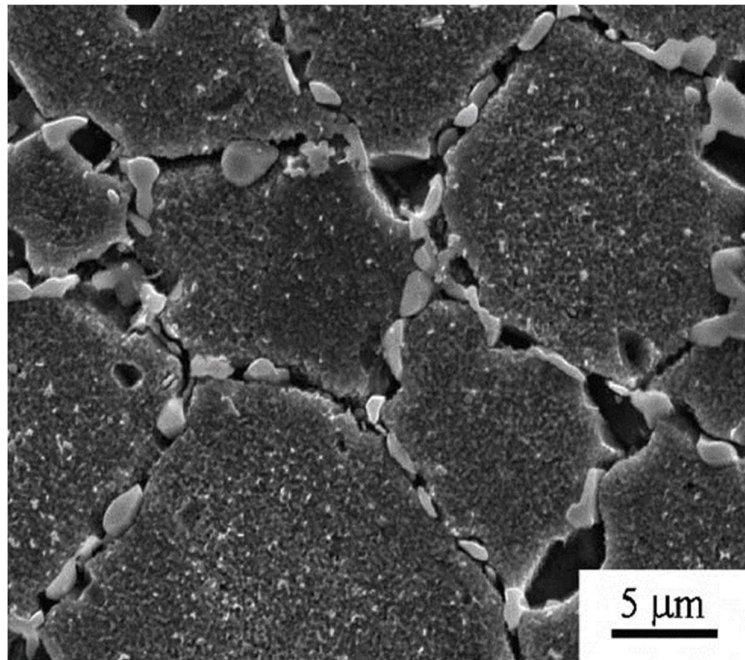


Figure 2.4 Scanning electron microscopic image of the superalloy RR1000 showing extensive precipitation of the grain boundary TCP phase [1]

2.1.3 Defects in Nickel Alloys

Considering different phase orientations, the face-centred cubic crystal structure in nickel-based superalloy consists of two types of stacking sequences, which are ABABAB... and ABCABC.... For $\{100\}$ and $\{110\}$ planes, the stacking sequence is ABABAB.... This type of stacking sequence is also can be found in hexagonal close-packed crystal structures. For $\{111\}$ planes in FCC structure, its stacking sequence is ABCABC... This kind of stacking sequence is considered a perfect lattice, however, as a crystal, nickel-based superalloys have a variety of defects, which can be categorized into point defects, linear defects and planar defects. Every defect will cause local distortion, affect the structure arrangement and end up affecting the material's properties [1,8].

Point Defects

In crystalline metals, point defects are divided into intrinsic defects and extrinsic defects. For intrinsic defects, it includes vacancy and self-interstitial atoms. The vacancy is caused by the removal of one atom from its original position. And the self-interstitial atom is a consequence of the emergence of an unexpected atom in a non-lattice position (see Figure 2.5) [8]

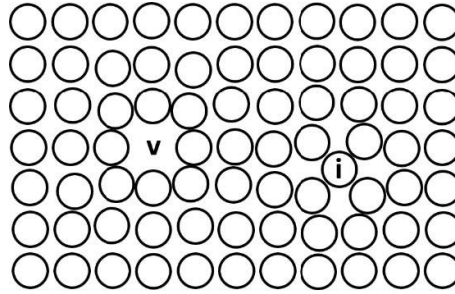


Figure 2.5 Label v represents the vacancy and label i represents a self-interstitial atom [8]

Extrinsic defects are formed by the introduction of impurity atoms. Impurity atoms can be categorized into substitutional atoms and interstitial atoms. A substitutional atom defect is defined as impurity atoms replacing the lattice position that belongs to the original atom. In nickel-based superalloy, it is described as Al atoms located on Ni atoms site. And when impurity atoms show up in a non-lattice position, this defect is defined as interstitial atom defect (see Figure 2.6). It is similar to the interstitial in intrinsic defects, but it is caused by the introduction of impurity atoms.

Undoubtedly, all the point defects mentioned will influence both the mechanical and physical properties of the materials. And the bigger size atom is introduced the higher distortion will be caused. However, point defects will be less significant when compared with volume defects such as precipitates and voids.

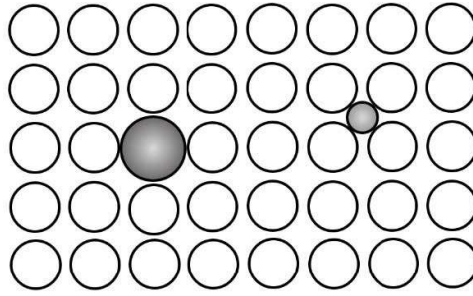


Figure 2.6 The atom on the left is a substitutional atom and atom on the right is an interstitial atom [8]

Line Defects-dislocation

Line defects are usually recognized as dislocations. For crystalline materials, dislocations occur in two different ways, edge dislocation and screw dislocation. Edge dislocations can be described as adding an extra half plane between two planes, and you can see from Figure 2.7, the distortion decreases with the increase of the distance to line DC. And for the extra half plane above line DC, it is called positive edge dislocation, symbolled by \perp . And a negative edge dislocation is formed by inserting the extra half plane below line DC, symbolled by \top .

Screw dislocation is formed by offsetting an atom plane without inserting an extra half plane. Normally, it can be illustrated as a “spiral staircase” and is a single surface helicoid. Screw dislocation has two types of deformation geometry, right-hand side (RHS) and left-hand side (LHS). Figure 2.7 (c) shows the LHS screw dislocation.

In FCC metals such as Nickel superalloys, the dislocation slip system is $a/2\langle 1\bar{1}0 \rangle\{111\}$, therefore, the burgers vector is $a/\sqrt{2}$. Such a dislocation in γ phase is dissociated into two partial dislocations, and this has been confirmed occurs in this form,

$$a/2\langle 1\bar{1}0 \rangle\{111\} \rightarrow a/6\langle 2\bar{1}1 \rangle\{111\} + a/6\langle 1\bar{2}1 \rangle\{111\}.$$

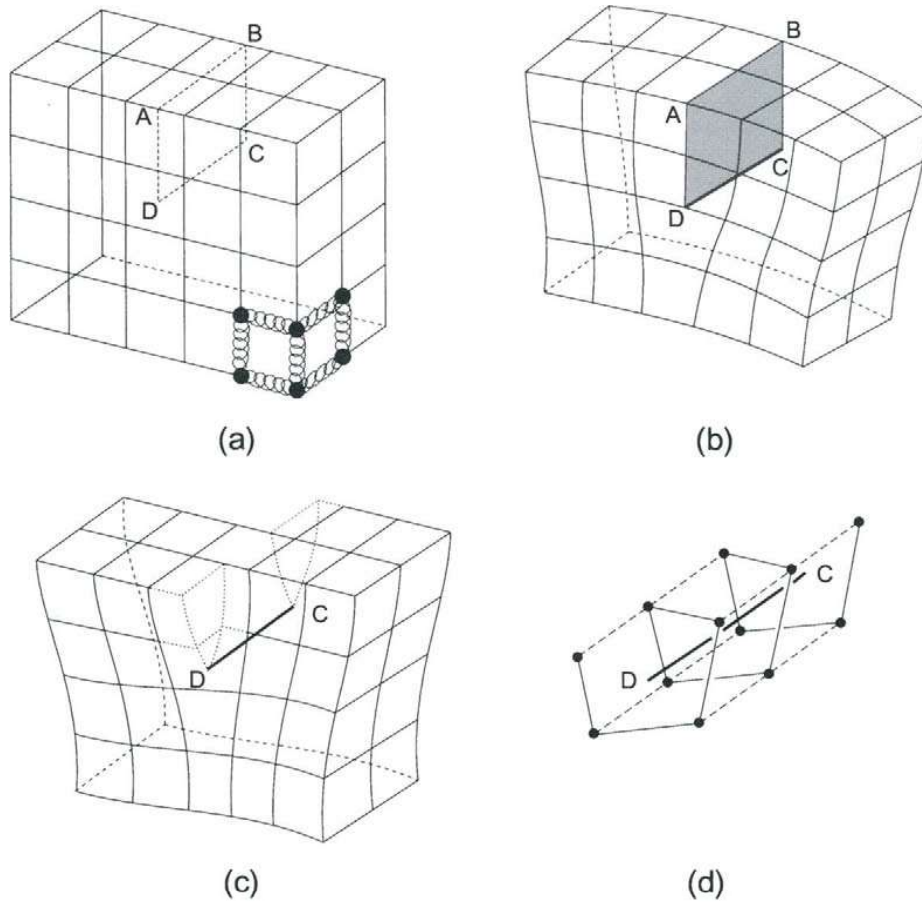


Figure 2.7 Schematic of (a) a cubic lattice; (b) positive edge dislocation line DC and extra half plane ABCD; (c) left-handed screw dislocation; (d) the helical atoms in screw dislocation [8]

As for γ' phase, the situation can be more complex. As a result of the ordering reaction in $L1_2$ structure, the burgers vector in γ' is longer than that in γ . Therefore, this makes the dislocation dissociation more complex in γ' phase. The possible dissociations are shown below:

- (i) dissociation by CSF, APB and CSF on $\{111\}$ planes,

$$a\langle \bar{1}01 \rangle \rightarrow a/6\langle \bar{1}\bar{1}2 \rangle + a/6\langle \bar{2}11 \rangle + a/6\langle \bar{2}11 \rangle + a/6\langle \bar{1}\bar{1}2 \rangle.$$

(ii) dissociation by APB, CSF and SISF on $\{111\}$ planes,

$$a\langle \bar{1}01 \rangle \rightarrow a/6\langle \bar{1}\bar{1}2 \rangle + a/6\langle \bar{2}11 \rangle + a/6\langle \bar{1}2\bar{1} \rangle + a/6\langle 1\bar{2}1 \rangle + a/6\langle \bar{1}\bar{1}2 \rangle + a/6\langle \bar{2}11 \rangle.$$

(iii) dissociation by APB on $\{111\}$ planes,

$$a\langle \bar{1}01 \rangle \rightarrow a/2\langle \bar{1}01 \rangle + a/2\langle \bar{1}01 \rangle$$

(iv) dissociation by SISF on $\{111\}$ planes,

$$a\langle \bar{1}01 \rangle \rightarrow a/3\langle \bar{1}\bar{1}2 \rangle + a/3\langle \bar{2}11 \rangle +$$

(v) dissociation by SISF and SESF on $\{111\}$ planes,

$$a\langle \bar{2}11 \rangle \rightarrow a/3\langle 1\bar{2}1 \rangle + a/3\langle \bar{1}\bar{1}2 \rangle + a/3\langle \bar{2}11 \rangle + a/3\langle \bar{2}11 \rangle$$

(vi) dissociation by APB on $\{010\}$ planes,

$$a\langle \bar{1}01 \rangle \rightarrow a/2\langle \bar{1}01 \rangle + a/2\langle \bar{1}01 \rangle$$

And here noted, complex stacking fault (CSF), anti-phase boundary (APB), superlattice intrinsic stacking fault (SISF) and superlattice extrinsic stacking fault (SESF). These are all planar defects which will be discussed in the next part.

The dislocation reaction shown in scheme (v) has been characterized in single crystal nickel superalloy CMSX-4 at a temperature of about 750°C, on condition that enough stress is applied to make primary creep happen. Figure 2.8 is the Transmission Electron Microscope (TEM) image of the dislocation mentioned above.

For dislocation dissociation (i) and (iii), they can occur when γ' or $\gamma + \gamma'$ alloys are deformed at the strain rates characteristic of a tension test. But practically, these dissociations will be more complicated than those given. Any super dislocation does not usually slip on one plane,

instead, in this case, the dislocation occurs on both $\{111\}$ and $\{101\}$ planes. This phenomenon is termed Kear-Wilsdorf Lock. As for the other dissociations, no evidence was found to support schemes (ii) and (iv) [8-15].

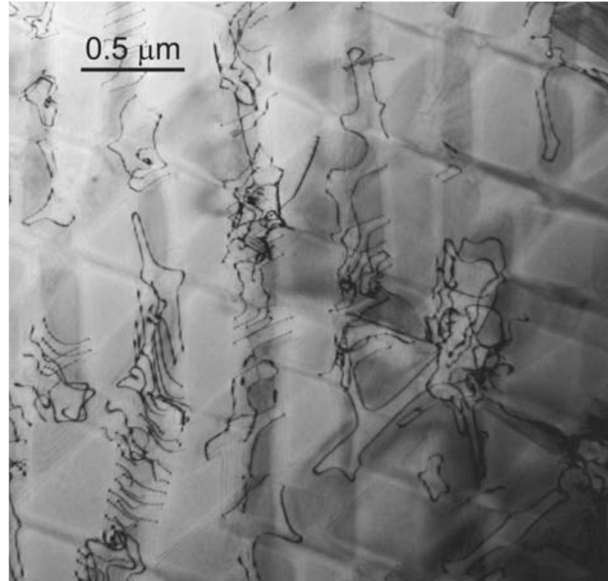


Figure 2.8 Transmission Electron Microscope image of CMSX-4 single-crystal superalloy, deformed to 0.04% strain in 1890 h at 750 °C and 450MPa. Note the localization of $\langle 1\bar{1}0 \rangle \{111\}$ dislocation activity in a limited number of γ channels. The foil normal is $\{111\}$ [1].

Planar Defects-stacking Fault

Planar defects in FCC structure are commonly known as stacking faults. Stacking faults are not expected on planes $\{100\}$ and $\{110\}$. A stacking fault is caused by interrupting the stacking sequence ABCABCABC... [9]. Hence, on plane $\{111\}$ there are two possible stacking fault sequences. Similar to point defects, there are two kinds of stacking faults, intrinsic and extrinsic. The removal of one plane introduces an intrinsic stacking fault and the addition of one plane introduces an extrinsic stacking fault [8].

The presence of stacking faults can play an important role in the plasticity of crystals. It should

be noted, for example, that the intrinsic fault in the face-centred cubic structure can be produced by a sliding process. If, say, an A layer is slid into a B position and all the layers above are moved in the same way, i.e., B to C , C to A , A to B , etc., then the new sequence $ABCBCAB...$ is identical to that discussed above [8].

Another important planar defect is called anti-phase boundary (APB). An anti-phase boundary can be described as when two γ' perfect crystals are bonded together, an APB can separate the two perfect lattices. Adjacent to the APB, the atoms arrangement is different from the original order. To be exact, the forbidden Ni-Ni and Al-Al are formed at the anti-phase boundary, thus the number of Ni-Al is reduced.

Three other planar defects were found and defined by former researchers such as Kear and his co-workers [10, 11]. For example, in a Ni_3Al $L1_2$ structure (figure 2.9 (a)), the top layer is sheared by $a/2 \langle \bar{2}11 \rangle$, see figure 2.9 (b), an APB is formed. If the top layer is sheared by $a/3 \langle \bar{2}11 \rangle$, see Figure 2.9 (c), the top Al atoms are now directly above the bottom Al atoms. The stacking sequence $ABCABCABC...$ changes to $ABCACABCABC...$. This transform is equivalent to removing one single $\{111\}$ plane. Therefore, on the analogy of the intrinsic stacking fault in γ phase, this can be referred to as a superlattice intrinsic stacking fault (SISF). The stacking fault energy (SFE) of SISF is low as it creates no adjacent distortion and SFE is about $10 \text{ mJ}/\text{m}^2$. Or, if shearing the top layer by $a/6 \langle \bar{1}\bar{1}2 \rangle$, the stacking fault vector of the FCC structure, see Figure 2.9 (d), so that the top Al atoms shift directly above the bottom Ni atoms. This gives rise to the complex stacking fault (CSF). CSF creates location distortion and has a high SFE which is estimated to be about $250 \text{ mJ}/\text{m}^2$. The last planer defect is called superlattice extrinsic stacking fault (SESF) which is not shown in Figure 2.9. SESF, rather than removing a $\{111\}$ plane, introduces an extra $\{111\}$ plane to the crystal structure without creating adjacent violation, so SFE is low [1,8,12].

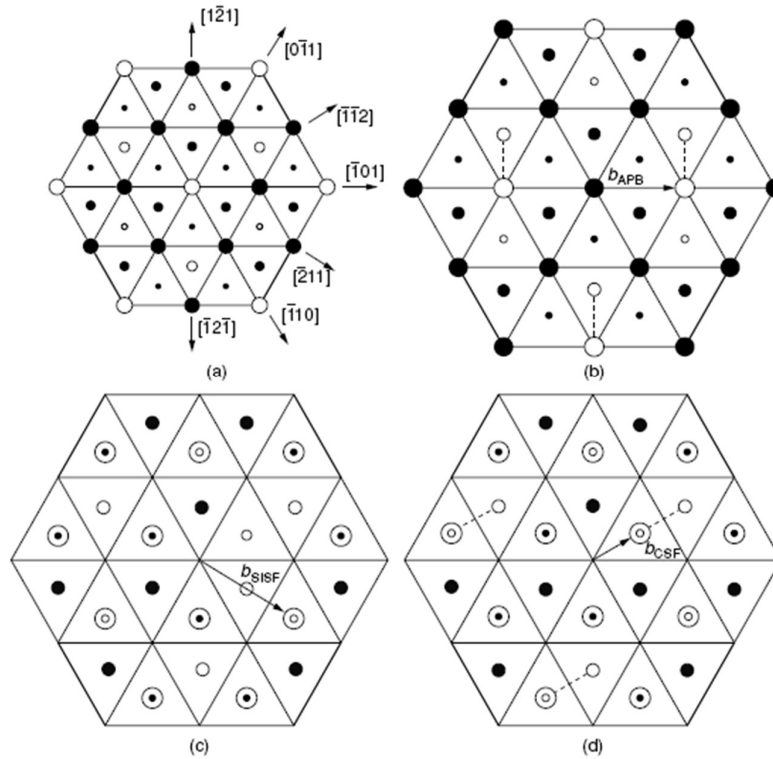


Figure 2.9 Illustration of various faults possible in the $L1_2$ structure formed by shearing $\{111\}$ planes past one another: (a) three successive $\{111\}$ planes, unfaulted; (b) an anti-phase boundary (APB); (c) superlattice intrinsic stacking fault (SISF); (d) stacking fault (CSF). Note that the large, medium and small circles represent atoms in the top, middle and bottom planes, respectively [8].

2.1.4 Fatigue Properties of Nickel Alloys

In service, superalloy components are subjected to cyclic loading and fatigue performance is one of the most significant properties that limit service life. Cyclic strain localization and fatigue crack initiation are closely related to the irreversible slip of dislocations under cyclic loading. This irreversible slip comes from the fact that the displacement imparted by the motion of dislocation in the forward loading cycle is not completely recovered in the reverse loading

cycle [12]. A parameter of slip irreversibility can be used to quantify the irreversible dislocation slip. The value of slip irreversibility is in the range of 0 to 1. There are many factors that can influence dislocation slip, thus influencing slip irreversibility.

In general, such factors can be divided into two types. The first type of factor is related to the microstructure features, such as grain boundaries and the morphology, size and distribution of precipitates. These factors can be labelled as intrinsic or internal variables. The second type includes applied fatigue testing conditions such as stress amplitude, temperature, cyclic frequency and environmental effects. These factors can be labelled as external variables. Therefore, slip irreversibility is a function of these external and internal or extrinsic variables. Apparently, it is difficult to include all variables in a quantitative characterisation of slip irreversibility. In practice, most current definitions of slip irreversibility are based on the shear strain carried by the irreversible slip of dislocations [13-17]. Mughrabi [12] defines slip irreversibility as the ratio of irreversible plastic shear strain to the cumulative total plastic shear strain due to the irreversible slip of dislocations under cyclic loading.

The irreversible slip of dislocations will cause the development of an inhomogeneous distribution of plastic deformation (or cyclic strain localization) and the resulting local microstructure changes, leading to permanent fatigue damage. Among all microstructure changes, persistent slip band formation is the most important one and has been the subject of extensive studies [18]. Persistent slip bands can be defined as a local deformation zone that fulfils the following three conditions [19]. 1) There is a cyclic strain localization in the zone. 2) Its dislocation structure differs from that in the surrounding matrix. 3) In single crystal and surface grains (if in polycrystals), the zone ends on the specimen surface in intrusions and extrusions. Extrusions are thin ribbons of metal extruded at the specimen surface from persistent slip bands under cyclic loading [20].

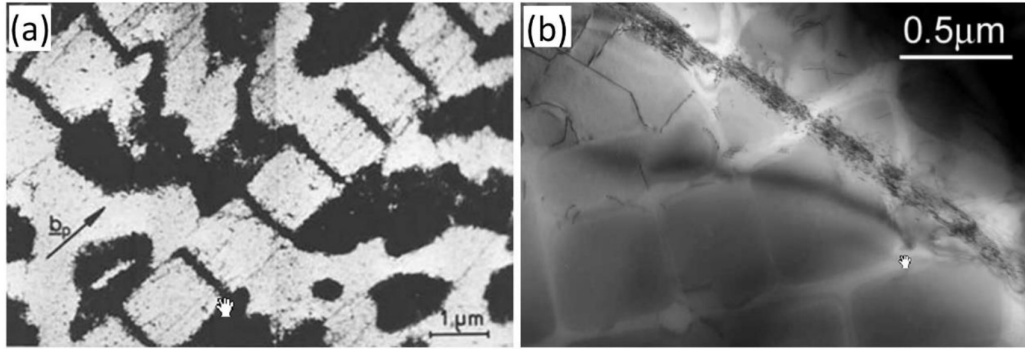


Figure 2.10 (a) image of a persistent slip band in a fatigued copper; (b) TEM image of persistent slip band in single crystal nickel alloy CMSX-4 fatigued at 850°C [14, 21].

Figure 2.10. (a) shows the morphology of persistent slip bands formed within a fatigued copper specimen. The dislocation density within persistent slip bands is very high compared to that of the surrounding matrix, indicating the inhomogeneity of cyclic deformation or cyclic strain localization. It can be seen that these persistent slip bands have a ladder dislocation structure. However, the specific morphology of persistent slip bands may depend on specific alloys and the associated testing conditions. Therefore, the ladder structure frequently observed in pure copper is not always observed in other alloys [13,21]. Figure 2.10. (b) shows the persistent slip band in single crystal nickel-based superalloy CMSX-4. The dislocation density within the persistent slip band is very high, while the dislocation density in the surrounding area is very low, indicating severe strain localization within the persistent slip band. The persistent slip band in this alloy does not have the typical ladder structure of PSB in copper as shown in Figure 2.10 (a).

2.1.5 Creep Properties of Nickel Alloys

Creep property is another important factor that will influence the performance of the alloys. Figure 2.11 below shows the creep behaviour of pure nickel under constant load conditions at 371 °C and stresses between 147 and 220MPa. As can be seen from the graph, pure nickel is

quite stress sensitive. There is a rapid ascending part at the beginning of each curve, which is noted as a primary creep; and the following steady state is referred to as secondary creep; in the last part of the curve, the strain rate continues to grow until its fracture occurs. There was another investigation about the nickel polycrystalline nickel dispersion-strengthened with a small fraction of ThO_2 particles, the loading is fixed at 28 MPa, and the temperature is diverse.

From Figure 2.12, it can be seen that the creep strain is sensitive to temperature as well, and particularly, an increase of 25°C can double the creep strain. The steady-state creep behaviour is the main part of creep life, which is the secondary creep. Creep is a quite slow procedure, and the steady state creep behaviour can be described as a balance between hardening and softening, or dislocation annihilation and multiplication [22-24]. On condition that the temperature is high enough, creep occurs in pure metals such as nickel by a combined climb-plus-glide mechanism – if a gliding dislocation becomes pinned, then a small amount of climb can release it, allowing further glide to occur. Dislocation glide is then responsible for the majority of the deformation, although the average velocity is determined by the climb step [23].

There are two ways to enhance the creep property, which are precipitation hardening and solid solution strengthening. γ' phase is a precipitated phase which is formed by alloying with Al and Ti. The presence of γ' phase has a significant effect on the creep performance of nickel-based superalloy. Studies have been conducted by Gibbons and Hopkins [25] regarding the influence of the percentage of Al and Ti on the creep behaviour, in other words, the influence of the volume fraction of γ' phase on the creep behaviour. As can be seen from Figure 2.13, on condition that the stress is not too high, the creep property is better with the increase of γ' fraction.

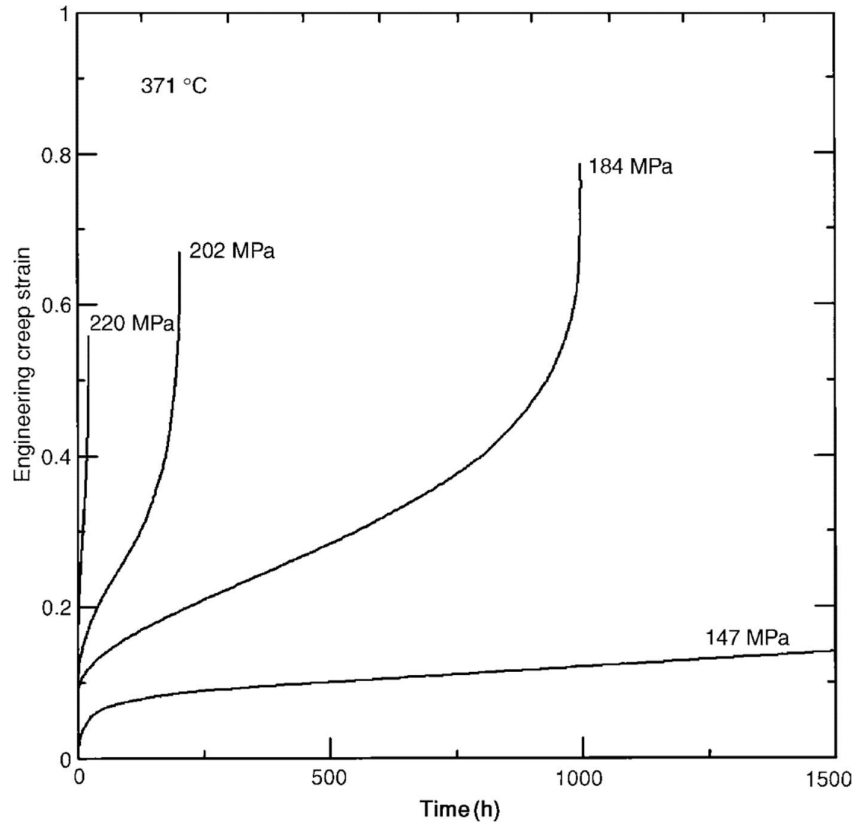


Figure 2.11 Creep curves for nominally pure nickel tested at 371°C [49]

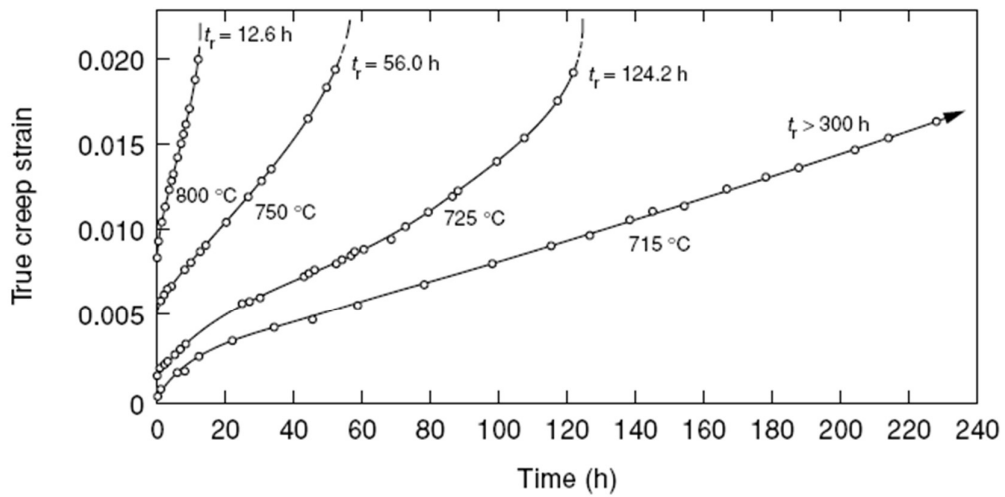


Figure 2.12 Creep curves for nickel doped with a small fraction of particles ThO_2 ; $\sigma = 28$ MPa. The time to rupture, T_r , is given for each creep curve [52]

In the case of solid solution strengthening, some investigations are also made to study the influence of different atoms on creep behaviour. A study conducted by J. P. Dennison et. [26] has stated that a strong correlation exists between the creep-strengthening increment and the percentage difference in atomic size between the solute and solvent (nickel) atoms. See Figure 2.14 below. It can be seen that a larger percentage difference in atomic size provides better creep resistance. Additionally, an inquiry into the correlation between creep property and alloying weight concentration was conducted by J. P. Dennison et. [26] As shown in Figure 2.15, it is apparent that the level of creep strengthening rises with the amount of solute incorporated.

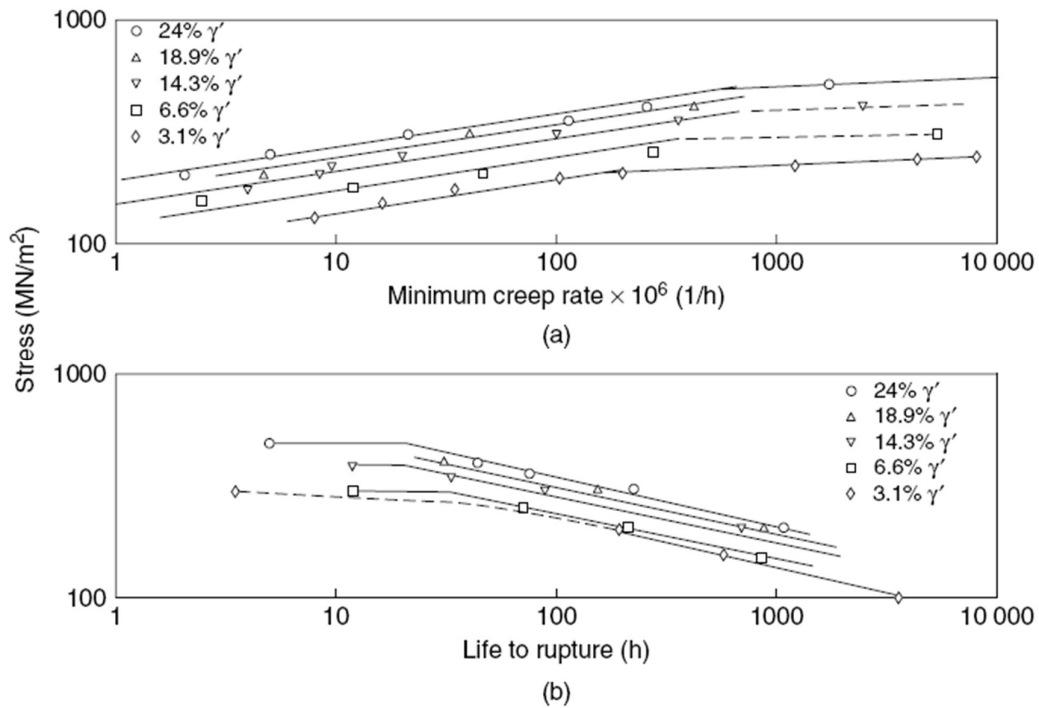


Figure 2.13 Variation of the (a) minimum creep rate and (b) life to rupture for several polycrystalline superalloys with varying fractions of the γ' phase [25]

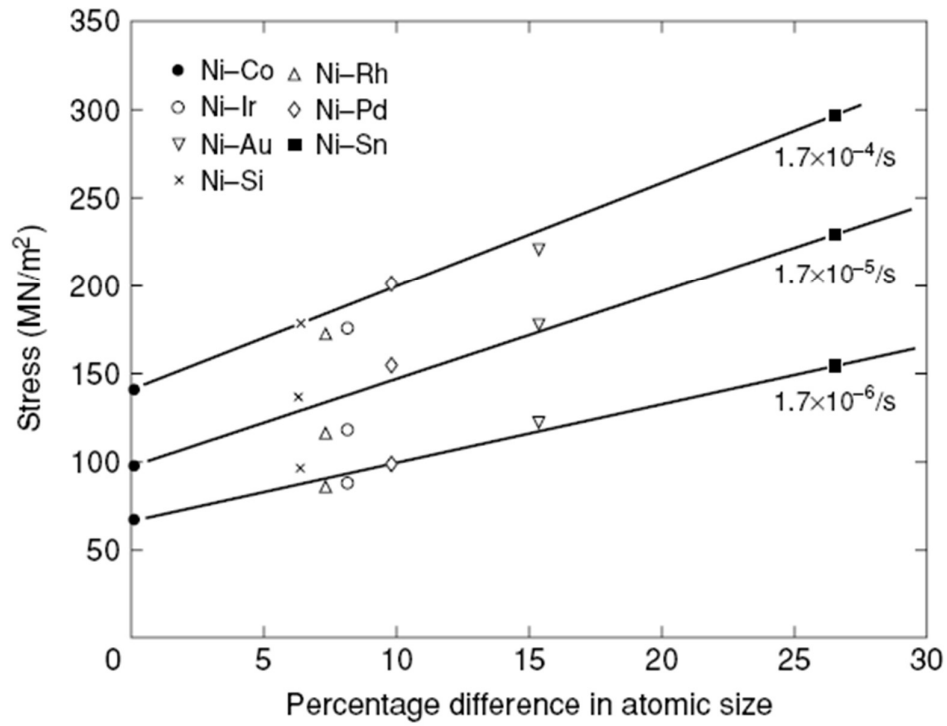


Figure 2.14 The relationships between the percentage difference in atomic size of solute and solvent atoms and the creep resistance at 500°C [26]

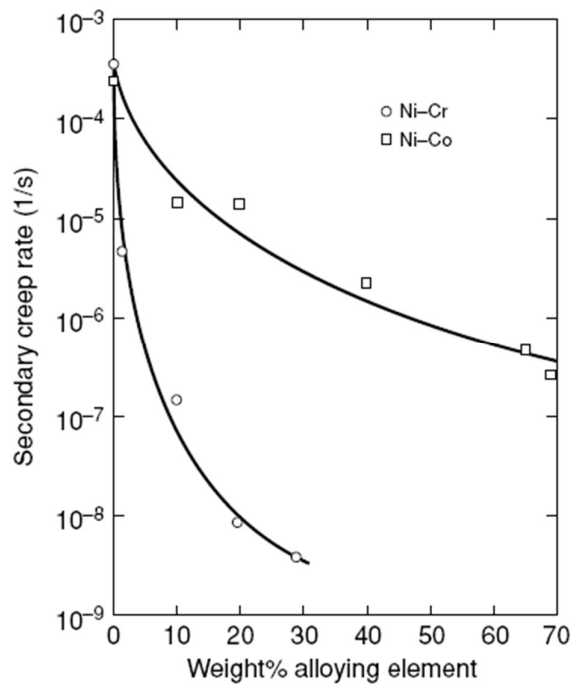


Figure 2.15 Variation of the secondary creep rate of nickel with cobalt and chromium content during creep at 500°C [30]

2.1.6 Heat Treatments of Nickel Alloys

Prior to the application of materials, heat treatment is an essential procedure. It can achieve [7]:

- a. stress reduction;
- b. movement of atoms and rearrangement of the existing alloy elements;
- c. acceleration of grain growth;
- d. promotion of new grains to form;
- e. the dissolution of phases;
- f. the formation of new phases;
- g. introduction of new atoms and change the chemistry on the surface.

There are many kinds of heat treatment methods, the most common methods are stress relieving, in-process annealing, full annealing, solution annealing, coating diffusion and precipitate(age) hardening.

Stress Relieving

The time and temperature cycles for stress relief may vary considerably, depending on the metallurgical characteristics of the alloy and on the type of residual stresses developed by previous fabricating processes. Stress-relieving temperatures are usually below the annealing or recrystallisation temperature. Tables 2.6, 2.7 and 2.8 provide an overview of representative stress relieving, annealing, solution and aging temperatures employed in the heat treatment of both wrought and cast nickel-based alloys. It is evident from Table 2.6 that the usual cycles for certain wrought superalloys, but temperatures that deviate by at least 45°F (25°C) from those listed are generally acceptable. Notably, stress relief is not a typical heat treatment technique for cast nickel-based superalloys.

Table 2.6 Typical stress relieving and annealing cycles for wrought heat-resisting alloys. [7].

Alloy	Stress relieving			Annealing(a)		
	Temperature		Holding time per inch of section, h	Temperature		Holding time per inch of section, h
	°C	°F		°C	°F	
Iron-base and iron-nickel-chromium alloys						
19-9 DL	675(b)	1250(b)	4	980	1800	1
A-286	(c)	(c)	...	980	1800	1
Discaloy	(c)	(c)	...	1035	1900	1
Nickel-base alloys						
Astroloy	(c)	(c)	...	1135	2075	4
Hastelloy X	(c)	(c)	...	1175	2150	1
Incoloy 800	870	1600	1½	980	1800	¼
Incoloy 800H	1175	2150	...
Incoloy 825	980	1800	...
Incoloy 901	(c)	(c)	...	1095	2000	2
Inconel 600	900	1650	1	1010	1850	¼(d)
Inconel 601	980	1800	...
Inconel 625	870	1600	1	980	1800	1
Inconel 690	1040	1900	½
Inconel 718	(c)	(c)	...	955	1750	1
Inconel X-750	880(e)	1625(e)	...	1035	1900	½
Nimonic 80A	(c)	(c)	...	1080	1975	2
Nimonic 90	(c)	(c)	...	1080	1975	2
Rene 41	(c)	(c)	...	1080	1975	2
Udimet 500	(c)	(c)	...	1080	1975	4
Udimet 700	(c)	(c)	...	1135	2075	4
Waspaloy	(c)	(c)	...	1010	1850	4

Full Annealing

When applied to superalloys, annealing implies full annealing, that is, complete recrystallization and the attainment of maximum softness. The practice is only applicable to wrought alloys of the non-hardening type. For the majority of the hardenable alloys, annealing cycles are the same as those used for solution treatment. However, the two treatments serve different purposes. Solution treatment has the intent to dissolve the second phase for subsequent reprecipitation. Annealing is used mainly to increase ductility (and reduce hardness) to facilitate forming or machining, prepare for welding, relieve stresses after welding, produce specific microstructures, or soften age-hardened structures by re-solution of second phases. Annealing may be used to homogenize a cast ingot. Annealing practices vary considerably among different organizations. Full annealing or solution treating requires high temperatures, typically ranging from 1800 to 2250 °F (982 to 1232 °C), or even up to 2400 °F (1316 °C) for single-crystal superalloys. However, achieving temperatures above 2200 °F (1204 °C) can be challenging and expensive. Some representative annealing temperatures of nickel-based alloys

are given in Table 2.6. The table reveals that the general practice for annealing these alloys encompasses a temperature range spanning from 955°C to 1175°C. To ensure the integrity of the material, it is crucial to prevent melting during annealing at high or even lower temperatures, as the segregation of alloying elements during solidification can significantly reduce the melting temperature.

Table 2.7 Typical solution treating and aging cycles for wrought heat-resisting alloys [7].

Alloy	Solution treating				Aging			
	Temperature		Time, h	Cooling procedure	Temperature		Time, h	Cooling procedure
	°C	°F			°C	°F		
Iron-base alloys								
A-286	980	1800	1	Oil quench	720	1325	16	Air cool
Discaloy	1010	1850	2	Oil quench	730	1350	20	Air cool
					650	1200	20	Air cool
N-155	1175	2150	1	Water quench	815	1500	4	Air cool
Nickel-base alloys								
Astroloy	1175	2150	4	Air cool	845	1550	24	Air cool
	1080	1975	4	Air cool	760	1400	16	Air cool
Hastelloy S	1065	1950	½	Rapid quench
Hastelloy X	1175	2150	1	(a)
Inconel 901	1095	2000	2	Water quench	790	1450	2	Air cool
					720	1325	24	Air cool
Inconel 600	1120	2050	2	Air cool
Inconel 601	1150	2100	1	Air cool
Inconel 617	1175	2150	2	(a)
Inconel 625	1150	2100	2	(a)
Inconel 706	925–1010	1700–1850	845	1550	3	Air cool
					720	1325	8	Furnace cool
					620	1150	8	Air cool
	925–1010	1700–1850	730	1350	8	Furnace cool
					620	1150	8	Air cool
Inconel 718	980	1800	1	Air cool	720	1325	8	Furnace cool
					620	1150	8	Air cool
Inconel X-750 (AMS 5667)	855	1625	24	Air cool	705	1300	20	Air cool
Inconel X-750 (AMS 5668)	1150	2100	2	Air cool	845	1550	24	Air cool
					705	1300	20	Air cool
Nimonic 80A	1080	1975	8	Air cool	705	1300	16	Air cool
Nimonic 90	1080	1975	8	Air cool	705	1300	16	Air cool
Rene 41	1065	1950	½	Air cool	760	1400	16	Air cool
Udimet 500	1080	1975	4	Air cool	845	1550	24	Air cool
					760	1400	16	Air cool
Udimet 700	1175	2150	4	Air cool	845	1550	24	Air cool
	1080	1975	4	Air cool	760	1400	16	Air cool
Waspaloy	1080	1975	4	Air cool	845	1550	24	Air cool
					760	1400	16	Air cool

Solution Annealing

Solution treating is intended to dissolve second phases, like carbides specifically in nickel-based superalloy, to produce maximum corrosion resistance or to prepare an alloy for subsequent aging. Additionally, it will homogenize microstructure prior to aging and/or fully recrystallize a wrought structure for maximum ductility. Actual production solution treatment

may not fully dissolve all second phases in precipitation-hardened alloys. Typical solution treating cycles are given in Tables 2.7 and 2.8. Although, a relatively low solution temperature is spotted at 855°C for Inconel X-750 (AMS 5667) alloy. The solution temperatures for nickel-based alloys lie generally between 1000°C to 1200°C.

Precipitation (age) Hardening

Precipitation treatments are intended to bring out desirable strengthening precipitates and control other secondary phases, including carbides and detrimental topologically close-packed (TCP) phases. Precipitation treatments also can serve to stress relieve. Typical precipitation (aging) cycles are also given in Tables 2.7 and 2.8.

Table 2.8 Typical solution treating and aging cycles for some cast precipitation-hardened nickel-base superalloys [7].

Alloy	Heat treatment (temperature/duration in h/cooling)
Polycrystalline (conventional) castings	
B-1900/B-1900 + Hf	1080 °C (1975 °F)/4/AC + 900 °C (1650 °F)/10/AC
IN-100	1080 °C (1975 °F)/4/AC + 870 °C (1600 °F)/12/AC
IN-713	As-cast
IN-718	1095 °C (2000 °F)/1/AC + 955 °C (1750 °F)/1/AC + 720 °C (1325 °F)/8/FC + 620 °C (1150 °F)/8/AC
IN-718 with hot isostatic pressing (HIP)	1150 °C (2100 °F)/4/FC + 1190 °C (2175 °F)/4/15 ksi (HIP) + 870 °C (1600 °F)/10/AC + 955 °C (1750 °F)/1/AC + 730 °C (1350 °F)/8/FC + 665 °C (1225 °F)/8/AC
IN-738	1120 °C (2050 °F)/2/AC + 845 °C (1550 °F)/24/AC
IN-792	1120 °C (2050 °F)/4/RAC + 1080 °C (1975 °F)/4/AC + 845 °C (1550 °F)/24/AC
IN-939	1160 °C (2120 °F)/4/RAC + 1000 °C (1830 °F)/6/RAC + 900 °C (1650 °F)/24/AC + 700 °C (1290 °F)/16/AC
MAR-M-246 + Hf	1220 °C (2230 °F)/2/AC + 870 °C (1600 °F)/24/AC
MAR-M-247	1080 °C (1975 °F)/4/AC + 870 °C (1600 °F)/20/AC
Rene 41	1065 °C (1950 °F)/3/AC + 1120 °C (2050 °F)/0.5/AC + 900 °C (1650 °F)/4/AC
Rene 77	1163 °C (2125 °F)/4/AC + 1080 °C (1975 °F)/4/AC + 925 °C (1700 °F)/24/AC + 760 °C (1400 °F)/16/AC
Rene 80	1220 °C (2225 °F)/2/GFQ + 1095 °C (2000 °F)/4/GFQ + 1050 °C (1925 °F)/4/AC + 845 °C (1550 °F)/16/AC
Udimet 500	1150 °C (2100 °F)/4/AC + 1080 °C (1975 °F)/4/AC + 760 °C (1400 °F)/16/AC
Udimet 700	1175 °C (2150 °F)/4/AC + 1080 °C (1975 °F)/4/AC + 845 °C (1550 °F)/24/AC + 760 °C (1400 °F)/16/AC
Waspaloy	1080 °C (1975 °F)/4/AC + 845 °C (1550 °F)/4/AC + 760 °C (1400 °F)/16/AC
Directionally-solidified (DS) castings	
DS MAR-M-247	1230 °C (2250 °F)/2/GFQ + 980 °C (1800 °F)/5/AC + 870 °C (1600 °F)/20/AC
DS MAR-M-200 + Hf	1230 °C (2250 °F)/4/GFQ + 1080 °C (1975 °F)/4/AC + 870 °C (1600 °F)/32/AC
DS Rene 80H	1190 °C (2175 °F)/2/GFQ + 1080 °C (1975 °F)/4/AC + 870 °C (1600 °F)/16/AC
Single-crystal castings	
CMSX-2	1315 °C (2400 °F)/3/GFQ + 980 °C (1800 °F)/5/AC + 870 °C (1600 °F)/20/AC
PWA 1480	1290 °C (2350 °F)/4/GFQ + 1080 °C (1975 °F)/4/AC + 870 °C (1600 °F)/32/AC
Rene N4	1270 °C (2320 °F)/2/GFQ + 1080 °C (1975 °F)/4/AC + 900 °C (1650 °F)/16/AC

2.2 Nickel alloy Haynes 282

Precipitation-strengthened alloys provide strength and properties that cannot be offered by solid solution alloys. While precipitation heat treatment may add intricacy to the manufacturing process, it can significantly enhance the creep property of the age-hardened γ' alloy, which can exceed twice that of the solid solution alloy in a given temperature range [27]. HAYNES® 282® alloy (UNS N07208) is a new precipitate strengthened superalloy developed for high temperature structural applications, especially those in aero and land-based gas turbine engines. It possesses a unique combination of creep strength, thermal stability, weldability, and fabricability not found in currently available commercial alloys. The new alloy has excellent creep strength in the temperature range of 1200 to 1700°F (649 to 927°C), surpassing that of Waspaloy, and approaching that of R-41 alloy [28],[29]. This surprising combination of properties has created great interest in advanced ultra-supercritical steam (A-USC) applications, both for turbines and other components. However, 282 alloy is more than a nickel alloy for A-USC applications alone, having already been adopted for hot section parts in gas turbines for aircraft and power generation, and creating a base for improved product availability in the future [28]. In this chapter, the basic metallurgy and properties of HAYNES 282 alloy are provided, together with information about environmental resistance, weldability, and casting of the alloy.

2.2.1 The Chemical Composition of Haynes 282

The chemical composition of Haynes 282 is shown in the Table 2.9 below,

Table 2.9 Chemical composition of Haynes 282(wt%) [27]

Element	Ni	Cr	Co	Mo	Ti	Al	Fe	Mn	Si	C	B
(wt%)	57	20	10	8.5	2.1	1.5	1.5max.	0.3max.	0.15max	0.06	0.005max.

The Ni content of all these alloys provides a relatively noble face-centred cubic (γ) base with excellent solubility for many alloying elements that bring useful metallurgical properties. At 20% Cr, 282 alloy has adequate Cr content balanced for operating at temperatures below the γ' solvus temperature of 997°C (1827°F). The judicious addition of 10% Co helps to control the γ' solvus, and Co is on the low end of the range for other alloys in this class since Co is a relatively costly element. At a combined Al + Ti content of 3.6 wt%, Haynes 282 achieves about 19 vol % γ' phase in the fully aged condition. Mo is an important solid solution strengthening element for providing excellent creep strength, especially in exposures near the higher end of the expected temperature range. Minor alloying additions that provide enhanced mechanical properties are C and B [29].

2.2.2 Metallurgical Microstructure

Like other alloys, Haynes 282 is a multiphase material, in which the FCC (γ) phase is the matrix distributing with carbides, γ' precipitates and other minor phases. The typical microstructure of Haynes 282 is shown in Figure 2.16. After solution treatment, Haynes 282 has a relatively equiaxed γ phase which is free of secondary phase, but some annealing twins and carbides are indicated, see figure 2.16(a). Because of the solution annealing temperature is higher than the solvus of $M_{23}C_6$, the grain boundary is quite clear. The blocky carbides are rich in Titanium and possibly disperse during deformation.

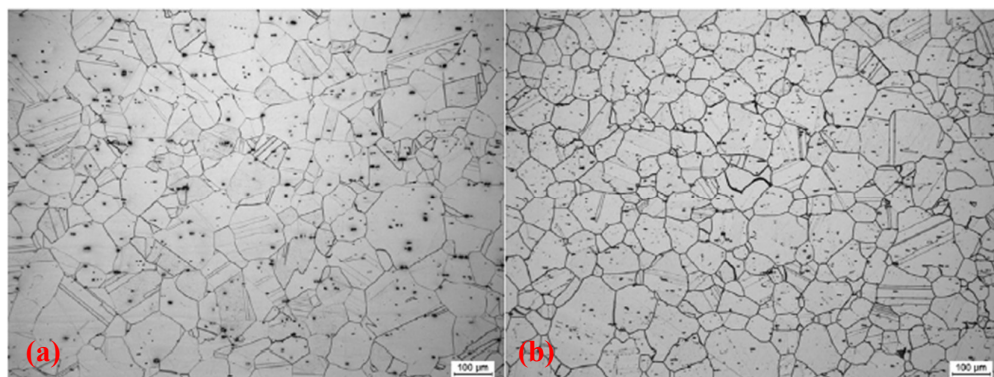


Figure 2.16 Typical microstructure of Haynes 282 alloy. (a) As solution annealed Haynes 282; (b) Aged Haynes 282 alloy [27].

2.2.3 Heat Treatment

HAYNES 282 alloy is provided in the solution-annealed condition, in which it is readily formable. The typical solution-annealing temperature is in the range of 2050 to 2100°F (1121 to 1149°C). After component fabrication, a two-step age hardening treatment is required to put the alloy into the high-strength condition. The treatment includes 1850°F (1010°C) / 2 hours / AC (air cool) + 1450°F (788°C) / 8 hours / AC.

The first step of the aging process targets the formation of chromium-rich M_6C carbides at the grain boundaries and be ready for the transformation to $M_{23}C_6$. Microscopic image is given in Figure 2.17(a) showing carbides are formed at grain boundary. Since this step of the heat treatment is above the γ' solvus temperature of 997°C (1827°F), no γ' phase precipitates in this part. The second step aims to form and stabilize γ' and to form $M_{23}C_6$. The 2-step aging process offers an optimized morphology for the best combination of mechanical properties. Air cooling at each step helps to achieve improved consistency of properties.

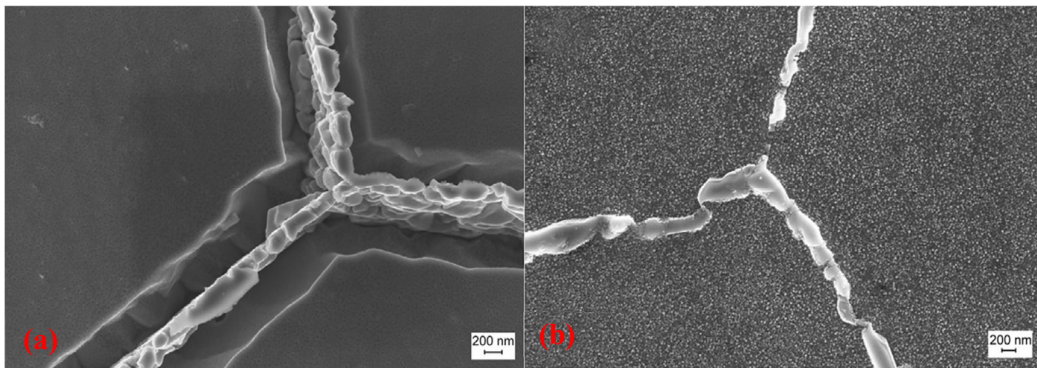


Figure 2.17 (a) SEM image of etched Haynes 282 alloy to highlight the grain boundary carbides after first step of the heat treatment cycle; (b) Haynes 282 etched to highlight the γ' phase after the second step of the heat treatment [51]

A single-step treatment of 800°C (1475°F)/6–8 h/AC can provide similar creep properties up to about 750°C (1382°F), but that does not quite match the full strength from the two-step aging process at the highest temperatures (ie, 750–900°C (1382–1652°F)). The single-step aging will lead to the precipitation of γ' phase, which serves the same purpose as the second step of in two-step treatment.

A group of equilibrium phase diagrams was calculated by Y. Yang et al [28], see Figure 2.18. It can be seen that the melting temperature of Haynes 282 is about 1300°C–1380°C. The γ' precipitates from γ matrix below 1000°C and stabilized at about 800°C. Mu phase, better known as μ phase or TCP phase, forms below 800°C. The magnified diagram illustrates precipitate evolution in small quantities such as carbides and borides. It is noticed that MX exists until the melting temperature. M_3B_2 precipitates out just below melting at 1250°C. Then M_6C forms from 1100°C and starts to transforming $M_{23}C_6$ from around 800°C, hence, $M_{23}C_6$ precipitates out from 800°C

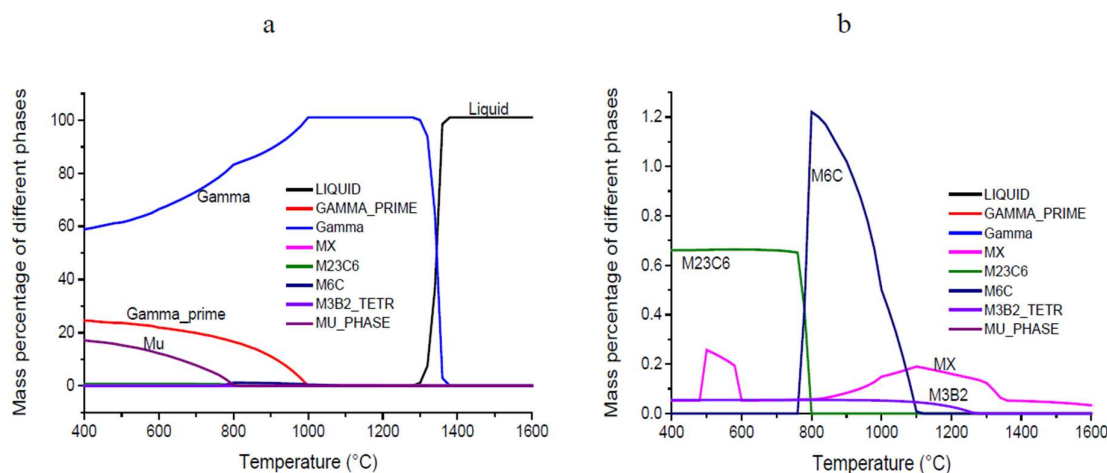


Figure 2.18 Equilibrium phase diagram of Haynes 282 (a) diagram in normal temperature scale; (b) a magnified temperature scale diagram to show minor precipitate phases [28]

2.2.4 Applications

The features of HAYNES 282 alloy make it suitable for critical gas turbine applications, such as sheet fabrications, seamless and flash butt-welded rings, and cases found in compressors, combustor, and turbine sections. In augmented aircraft gas turbines, the new alloy will be useful for exhaust and nozzle components. In land-based gas turbines, HAYNES 282 alloy is a good candidate for transition sections and other hot-gas-path components.

2.3 Microstructure Evolution and Modelling During Thermo-Mechanical Processing for Nickel-based Superalloy

2.3.1 Precipitation Evolution and Modelling

Nickel alloys are well-known as precipitation strengthened materials. This is attributed to the introduction of γ' strengthening elements such as Al, Ti and Ta. As described in Chapter 2.1, these elements replace the lattice position of Ni, therefore, creating lattice distortion and strengthening effects. The lattice of a typical γ' crystal generated by CrystalMaker software is shown Figure 2.19 below. Since the thermal stability mainly depends on the resistance of the precipitate coarsening. Hence, studying precipitation evolution after different kinds of post heat treatment has always been a popular topic for nickel superalloys.

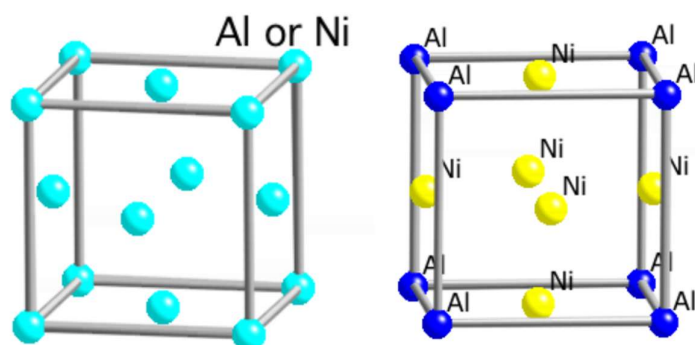


Figure 2.19 Typical γ' crystal lattice created by CrystalMaker software showing a FCC structure with Ni atoms at centre and Al atoms at corner

Extensive work has been undertaken regards the precipitation coarsening behaviour of nickel-based superalloys. According to previous studies, after extended thermal exposure, not only the has occurrence of coarsening been captured, but also changes in morphology and distribution have been recorded and proven to be hazardous to mechanical properties [31-33].

These changes are originally driven by the minimization of system free energy such as interfacial energy and elastic energy [30]. In order to achieve this, smaller γ' particles tend to dissolve into the matrix and precipitate out again onto larger ones, this phenomenon is known as Ostwald Ripening [31]. In addition, the coarsened γ' precipitates are oriented along the direction of the lowest Young's modulus (i.e. $\langle 100 \rangle$ direction in most cubic materials) to minimize the energy associated with lattice coherent strain [36,37].

The Ostwald Ripening process has been used to describe the coarsening of γ' precipitates. And the LSW theory proposed by Lifshitz and Slyozov and Wagner [32] has also been used to explain the coarsening kinetics of γ' precipitates [30]. The classic LSW theory was built based on the assumption that: (a) the particles are in forms of spherical in a liquid system; (b) the space between particles is large enough to avoid any inter-particle reaction accrue; (c) the volume fraction is low, preferably close to zero [36,38]. In spite of that zero volume fraction is impossible to achieve in alloys and sometimes it is relatively high, previous studies proved that the classic LSW theory is applicable to most Nickel alloys [34,39]. In addition, validations and modifications have also been made to LSW theory. A modified LSW theory (MLSW) was raised by Ardell [33], which proposed that with the increase of precipitates volume fraction, particle growth rate increases and the distribution of particle size becomes broader. Davies et al. found a Lifshitz-Slyozov encounter modified (LSEM) model [34] and suggested that the particle growth rate increase to a small extent and particle size distribution becomes broader. Both classic or modified LSW theories apply to a matrix-diffusion-controlled precipitation mechanism and agree that the precipitates coarsening can be described by a power law:

$$(R_t^n - R_0^n) \propto t \quad (1)$$

where R_t is the average particle radius at time t , R_0 is the average particle radius at $t=0$, n is a temporal exponent and its value is decided by a different precipitation mechanism. The matrix-diffusion-controlled precipitation mechanism is a process by which the diffusion of elements

from the matrix to the γ' phase strengthens the coherence of the precipitates. In this mechanism, interfaces between the matrix and precipitate phases play a crucial role in controlling the growth of the γ' phase. The diffusion of elements from the matrix to the γ' phase leads to a change in the chemical composition of the γ' phase, causing it to grow and strengthen the material. According to the research conducted by Yuting et al., In the case of a precipitation mechanism controlled by matrix diffusion, $n=3$ [30]. Therefore, the expression of classic LSW theory is:

$$R_t^3 - R_0^3 = Kt \quad (2)$$

K is the coarsening rate constant which can be defined in Arrhenius equation:

$$K = A \exp \frac{Ea}{RT} \quad (3)$$

Where A is a constant, Ea is the activation energy of precipitation growth, R is the gas constant and T is the aging temperature. This equation can also be written as:

$$\ln K = -\frac{Ea}{RT} + \ln A \quad (4)$$

Ardell and Ozolins proposed a new volume fraction independent coarsening model, which is called Trans-Interface Diffusion Control (TIDC) coarsening model. This model involves the diffusion of solutes through the ordered γ/γ' interface rather than through the disordered γ matrix [35]. They raised that the coarsening by TIDC model is much slower than classic LSW models, therefore, the TIDC model follows a power law that the $n=2$,

$$R_t^2 - R_0^2 = K_i t \quad (5)$$

Where K_i is the coarsening rate for TIDC model, and the rest of the parameters are the same as in equation (2).

Comparative works have been done between LSW model and TIDC model. The outcomes suggested that the LSW model is superior to TIDC model in describing the coarsening behaviour of γ' precipitation, which means that the coarsening of γ' precipitation is mainly controlled by volume diffusion rather than Trans-Interface diffusion. However, Yuting Wu et al. found that the γ' coarsening can be divided into two stages which include an LSWM model controlled early stage and a TIDC controlled later stage. The study was conducted on a Ni_3Al -based alloy and activation energy was calculated for the early stage at 174.2kJ/mol and 186.3kJ/mol for later stage, respectively [36].

2.3.2 Grain Growth, Recovery and Recrystallisation

Grain Growth

As an essential microstructure feature, grain has a significant effect on most mechanical properties. For example, hardness, yield strength, tensile strength, fracture resistance, fatigue and creep properties, etc. Grain growth is achieved by grain boundary movement and usually happens under elevated temperatures. The mechanical properties are all enhanced by smaller grains. Fine (smaller) grains create more grain boundary area, and therefore more hindering borders for dislocation movement. This is well known as Grain Boundary Strengthening (or Hall-Petch Strengthening) [37]. The driving force for grain growth depends on the grain boundary energy as small grain stores higher energy than bigger ones. The decrease in total grain boundary area leads to an attendant reduction in total energy [38]. However, this common theory can be interrupted and divided into normal or continuous grain growth (CGG) and abnormal or discontinuous grain growth (AGG). AGG happens when a subset of grains possess higher grain boundary energy, or lower local particle density [39]. An example is given below showing the difference between CGG and AGG. Generally, materials that tend to be dominated by AGG have one or more following features. (1) Possess enough amount of secondary phase precipitates or inclusions; (2) Possess high anisotropy in solid-solid grain boundary energy or solid-liquid interfacial energy; (3) High chemical disequilibrium [40]. As a precipitate-

strengthened and carbide enriched material, Nickel alloy is observed to have AGG behaviours [41].

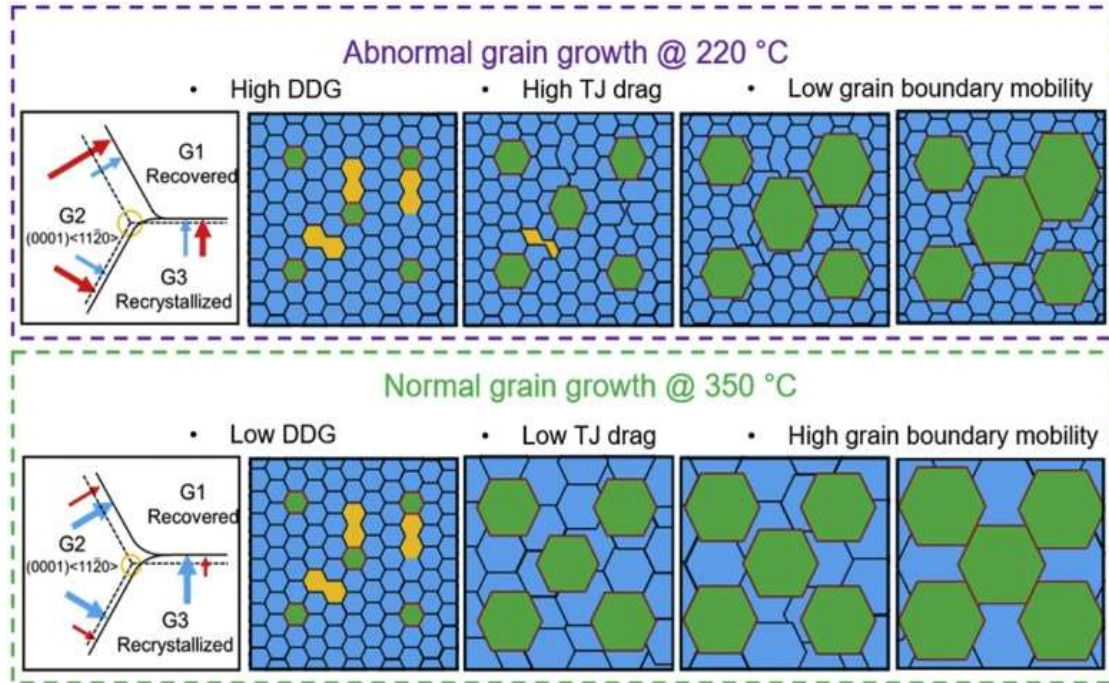


Figure 2.20 Schematic for AGG and CGG occurring in annealed magnesium [50]

Recovery and Recrystallisation

Recovery and recrystallisation normally occur during plastic deformation or annealing. Together with grain growth, recovery and recrystallisation are the major phenomena in plastic deformation and annealing, and they are all driven by stored energy. Recovery happens when deformed grains try to reduce stored internal strain energy by removing or rearranging defects in crystal structures [38]. Recovery leads to a reduction in material strength and an increase in ductility.

Different from recovery, recrystallisation is a “re-construction” of grains. It is the formation of new, strain-free and equiaxed grains. Normally, the recrystallisation temperature is equal to about $0.3T_m$, where T_m is the absolute melting temperature. The recrystallisation temperature and melting temperature are listed in Table 2.10. It can be seen from the table that the

recrystallisation temperature for nickel is 370°C, which is $\approx 0.26 T_m$. Recrystallisation temperature can reach $0.7T_m$ by alloying.

Table 2.10 Recrystallisation and melting temperature for various metals [38]

Metals	Recrystallisation Temperature		Melting temperature	
	°C	°F	°C	°F
Lead	-4	25	327	620
Tin	-4	25	232	450
Nickel	370	700	1455	2651
Aluminum	80	176	660	1220
Copper	120	250	1085	1985
Brass (60Cu 40Zn)	475	887	900	1652
Iron	450	840	1538	2800
Tungsten	1200	2200	3410	6170
Zinc	10	50	420	788

Moreover, recrystallisation can be divided into static recrystallisation (SRX) and dynamic recrystallisation (DRX) [42]. Specifically, SRX refers to recrystallisation which occurs during annealing and DRX occurs during plastic deformation.

DRX has been studied for decades and is categorized into discontinuous and continuous recrystallization (DDRX and CDRX), and geometric dynamic recrystallization (GDRX) (the names and abbreviations may differ from different researchers). When it is not noticed specifically, DRX normally refers to DDRX. DDRX occurs on alloys with low or medium stacking fault energy (SFE) during hot deformation. It has the following main characteristics which have been investigated by experiments:

- (1) Critical strain (ϵ_c) is lower than peak strain (ϵ_p) and reached its critical point before DDRX happens [43];

- (2) The stress-strain response may exhibit either singular or multiple peaks, based on factors such as the initial grain size (D_0), applied strain rate ($\dot{\epsilon}$), and deformation temperature (T), see figure 2.22 [49,51];
- (3) The nucleation of DDRX usually begins at the pre-existing grain boundary, and when there is a large difference between the initial grain size and the recrystallized grain size, a necklace structure of equiaxed grains is formed [44];
- (4) The recrystallization kinetics are accelerated with the decrease of initial grain size, strain rate and the increase of deformation temperature [51,53];
- (5) During DDRX, grain refinement as well as grain coarsening occurs dependent on the initial grain size and deformation conditions. A power-law relationship between the steady-state grain size and the Zener-Holomon parameter (or stress) is generally observed [45].

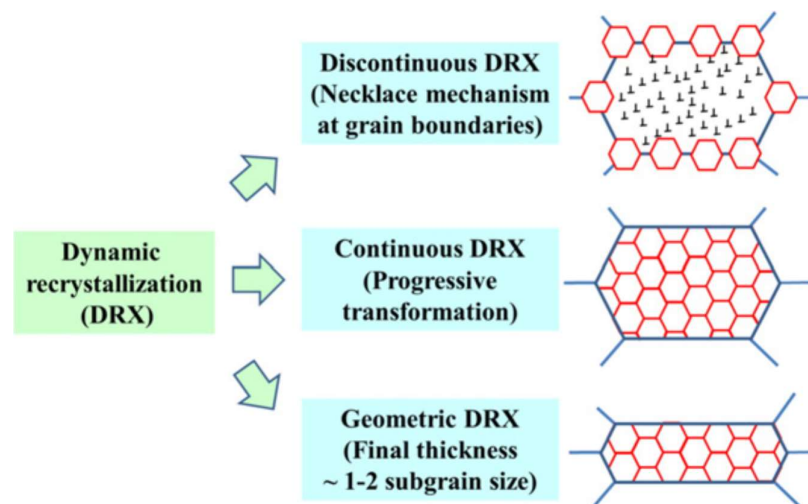


Figure 2.21 Schematic illustrates the widely recognised categories of DRX and their difference [42]

Nickel alloys are known as relatively low stacking fault energy materials [46]. Therefore, DDRX is the dominating DRX type in Nickel alloys.

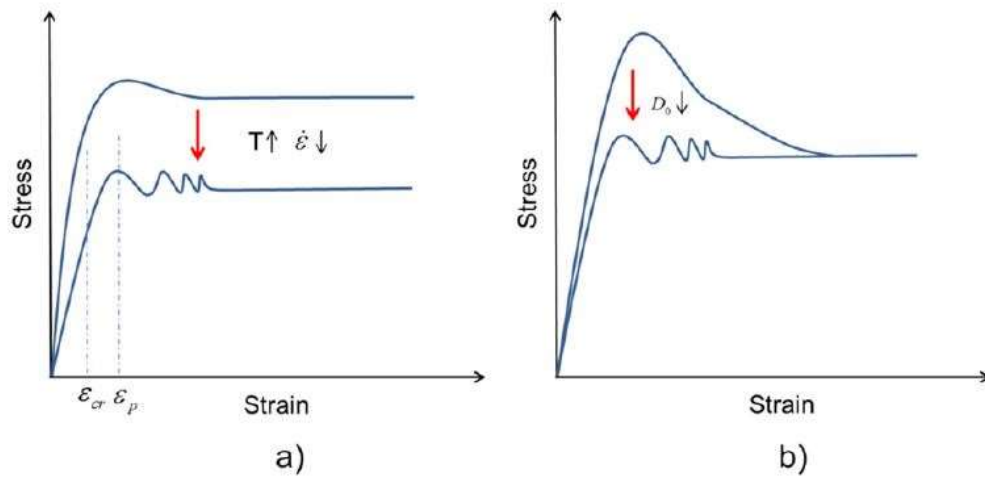


Figure 2.22 Histograms illustrate the difference between general hot deformation process with a DDRX controlled process, (a) and (b) show the single to multiple peaks when applying different deformation parameters [42]

2.4 Summary

Nickel-based superalloy has various categories with various applications. Given the inherent characteristics of nickel, it is deemed more suitable for use in aerospace engines. Therefore, the stability under elevated temperatures is vital for nickel-based superalloy. Haynes 282, as a relatively newly developed nickel alloy in the past decades, possesses desirable weldability and fabricability compared with similar alloys such as Waspalloy. Reviewing the literature, plenty of research has been conducted on Haynes 282 regarding its formation, heat treatments, microstructure evolutions and hot deformations. Nonetheless, it has been observed that the description of precipitation evolution is insufficient, and the activation energy required for precipitate coarsening to occur has yet to be determined. In addition, hot deformation and the DRX mechanism of Haynes 282 at lower temperature was investigated by Emil Eriksson et al [47]. Their research well-presented the microstructure evolution of Haynes 282 underwent a series of hot compression tests between 1000°C-1100°C. Nevertheless, the determination of the Zener-Hollomon parameter and activation energy at various strains is yet to be established through further analysis. Therefore, the objective of this study is to conduct a comprehensive examination of the microstructural evolution in Haynes 282 alloy, which will be elaborated in Chapters 4 to 6.

Chapter 3 Experimental Procedures

The experimental procedure includes heat treatments, sample preparations, characterisations, hot compression testing and data analysis techniques. As mentioned in previous chapters, the aim of the study is to obtain a better understanding of post heat treatment effects on microstructure and mechanical properties and to reveal the dynamic recrystallisation mechanism of the alloy. The experiments consist of both static and dynamic tests at elevated temperatures. All these experiments were carried out at Swansea University

3.1 Materials Used

The material, Haynes 282, was produced by hot ring rolling and received in as-forged condition without any post-treatment. The chemical composition of this alloy was detailed in the literature review. Haynes 282 specimen was received from Rolls-Royce plc and the processing history was detailed subsequently. The specimen was in the form of a quadrant of a ring roll forging of 600mm OD x 525mm ID x 203mm, see Figure 3.1. The ring was rolled in two passes. The first pass pre-rolled it to 350mm ID x 465mm OD x 206mm tall, and the second pass rolled it to 525mm ID (rolling time is 65 seconds). Prior to the second pass, the ring was reheated to 1150°C before being transferred to the mandrel. The temperature was measured in-situ at a corner of the ring using an IP pyrometer and the temperature drop during the last pass was shown in Figure 3.2. Then, two sets of samples were prepared after receiving from Rolls-Royce, rectangular bars of dimensions 39mm(L)*10mm(W)*10mm(H) for either further sample preparations or static heat treatment and round bars of dimensions 10mm(D)*15mm(H) for solution treatment and Gleeble hot compression tests.

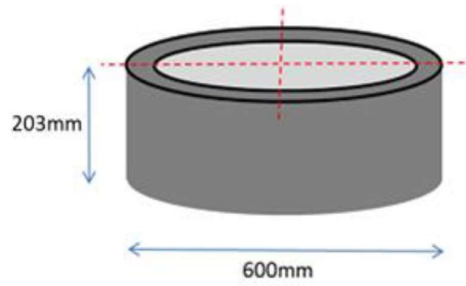


Figure 3.1 Diagram of parameters of ring-roll forged Haynes 282

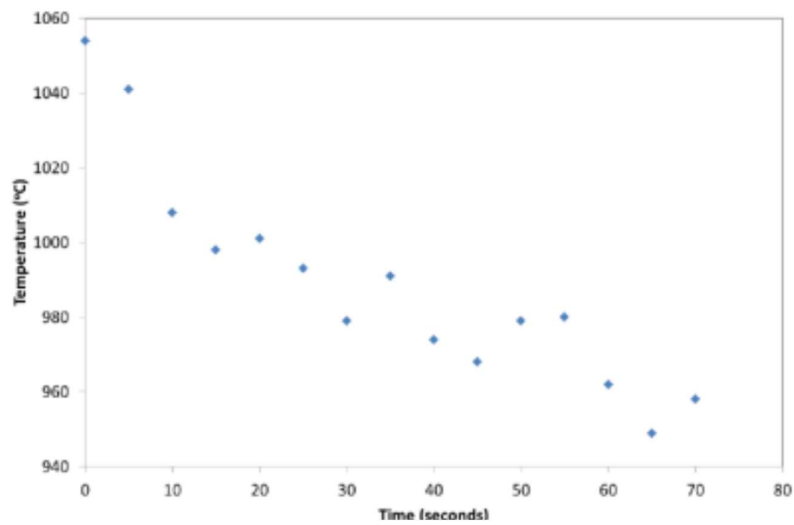


Figure 3.2 Temperature drop during last pass of ring rolling process



Figure 3.3 Round and rectangular bar samples

3.2 Static Heat Treatment

The heat treatments were conducted on nickel rectangular bars in as-received condition and using Carbolite CWF 1200 chamber furnace, see Figure 3.4. In this project, the conventional post heat treatment for Haynes 282 that is applied in industry and nine 1 step-aging at 730°C, 830°C and 930°C for 4, 8 and 16 hours were conducted as illustrated in figure 3.5. The heat treatment building strategy and parameter determination will be explained in the next chapter.

Prior to a heat treatment, a K-type thermocouple was inserted into the furnace from the top and placed as close as possible to the sample. Therefore, it had to be hanging inside the furnace, with ceramic wool acting both as a thermal insulator and as a support to fix the thermocouple in the desired position. Hence, it was not possible to place the thermocouple in direct contact with the sample. Instead, the thermocouple was between 2 and 5 mm from the sample. Due to the small size of the samples, to facilitate their insertion and extraction with the tongs, each one of them was placed on top of a ceramic crucible. The schematics below show the process of two types of static heat treatment. The furnace was heated up at maximum power rate, average heating rate lies between 12°C/min-14°C/min. The samples were then put into the furnace once the temperature was stabilised. It is worth mentioning that the samples were taken out successively when aging time reached 4 hours, 8 hours and 16 hours, followed by air cooling. And it should be mentioned that, in order to obtain a γ' -free microstructure, water quench cooling is essential after every solution treatment. For each solution treatment, samples were put into cooling water immediately after taking out from the furnace, so that the precipitation of γ' cannot occur and a supersaturated solid solution is obtained. Samples were soaked in cooling water until samples were cooled completely, this takes about 1min for a treatment.



Figure 3.4 Carbolite CWF 1200 laboratory chamber furnace

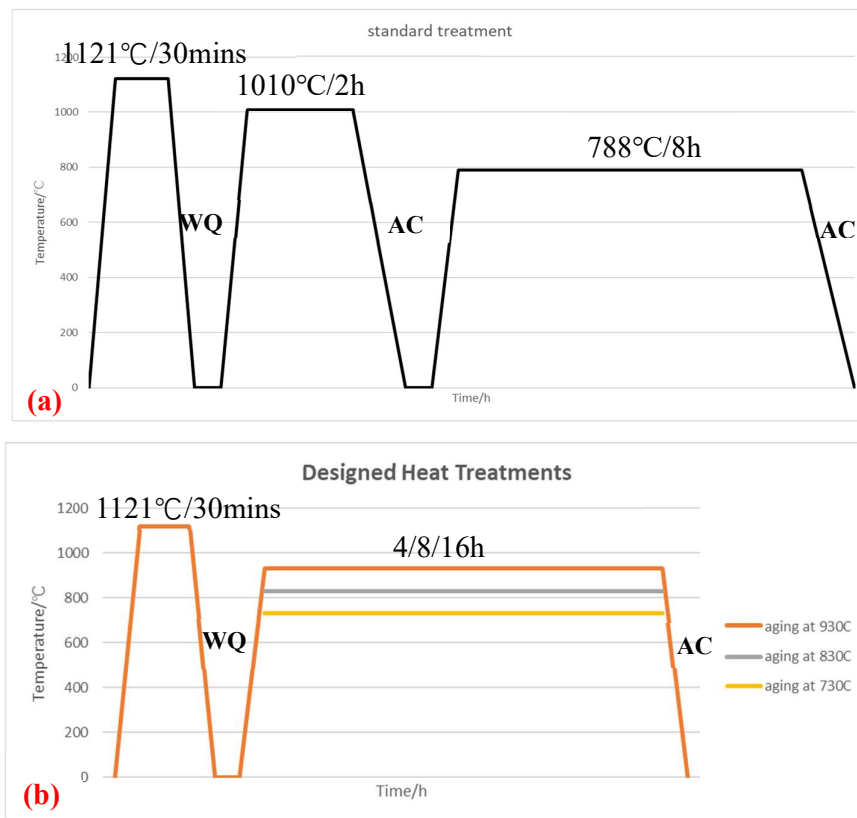


Figure3.5 Schematics of post heat treatment, (a) Standard treatment;
(b) Designed 1-step-aging treatment

3.3 Dynamic Hot Compression Test

The hot compression test was carried out on nickel round bars in solution-treated condition and using Gleeble 3500 system. Nine single-pass gleeble tests were designed, the temperature range is between 730°C to 930°C and the engineering strain rate used is up to $0.05s^{-1}$. Parameter details are shown in Table 3.1.

Table 3.1 Hot compression test parameters

Temperature	730°C	830°C	930°C
Heating rate	$\sim 8^{\circ}\text{C/s}$		
Dwell time	10s	100s	1000s
Stroke rate	0.75mm/s	0.075mm/s	0.0075mm/s
Strain rate	$0.05s^{-1}$	$0.005s^{-1}$	$0.0005s^{-1}$

Before the test, the surface of the samples was ground using 120 grit size paper to remove oxidation and inclusion formed during heat treatment and machining process. Besides, a clean surface provides desired conductivity between the samples and thermocouples as the thermocouple wire needs to be welded onto the sample. A thermocouple welder, shown in Figure 3.6, was used and a voltage of 30v was applied. Prior to sample placement, a conductivity check between the machine and anvils ends is necessary, because a bad conductivity would cause a heating delay or even a test abortion. The sample welded with thermocouple wires was then mounted on a sample holder that can be fitted beside the test chamber. A layer of tantalum foil with nickel paste was placed between the sample and anvils to maximize friction during compression. In order to place the sample in position, a small force (about 10kgf) was applied to catch the samples from the holder. Once the sample is firmly caught by anvils, the holder will be removed and the chamber is ready to close.

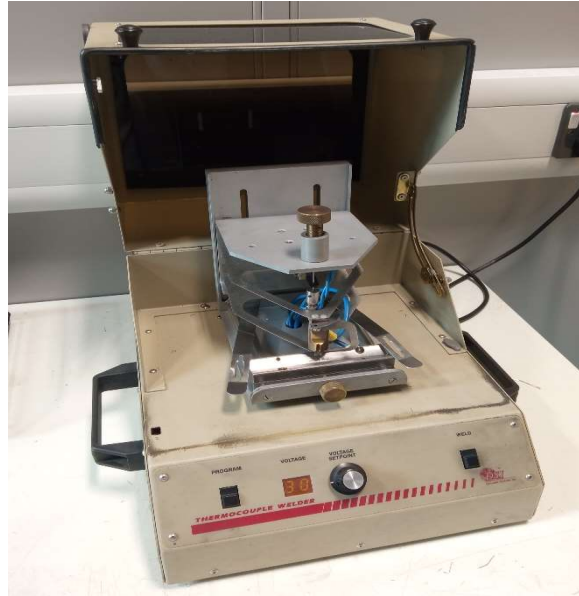


Figure 3.6 Thermocouple welder

The test can be divided into 3 stages. 1) Heating up. The first stage was to heat the sample up to its designated point. The data acquisition frequency is 1.0Hz. A default force of 60kgf was applied in the first 10s, and then the sample was heated to target temperature at a maximum heating rate (about 8°C/s). During heating up, two parameters from the machine should be always monitored, PowAngle and OilTemp. PowAngle represents the condition of conductivity. If the PowAngle remains constantly high such as 70%-100%, it means the sample is struggling to reach its target temperature, which means poor conductivity. As for OilTemp, its temperature will get higher with multiple tests and the machine would get too hot to run. The maximum OilTemp is 40°C according to the lab code; 2) Hot compression. The second stage was compressing the sample to reach 0.5 engineering strain at the designated temperature. The data acquisition frequency was 2.0Hz. The process will be held for 1s after reaching the target temperature and then start compressing. The engineering strain rate were $0.05s^{-1}$, $0.005s^{-1}$ and $0.0005s^{-1}$, corresponding to 10s, 100s and 1000s dwell time. Once the test reaches 0.5 engineering strain, the compression stops and the process will be held for 1s before cooling down; 3) Cooling down. Chamber can be opened once the test was finished and air cooling

was applied for this stage. This took 20s, 25s and 30s for the sample to cool down to 500°C corresponding to the target temperature of 730°C, 830°C and 930°C respectively. Fully cooling to room temperature took approximately 5 mins.

3.4 Metallographic Preparation

Sample preparation is a huge topic, it is not only consisting multiple procedures but also varies with different materials of the sample and different characterisation techniques. In this project, samples were prepared in different ways according to different testing histories and different characterisation techniques applied afterwards. For this part, the preparation procedures will be described based on the general metallographic preparation sequence.

The samples of static heat treatment are rectangular bars, see Figure 3.3, and were examined by OM (optical microscope), SEM (scanning electron microscope), EBSD (electron backscattered diffraction) and TEM (transmission electron microscope). Samples after dynamic hot compression testing were in a barrel shape and were only examined by EBSD.

3.4.1 Cutting and Mounting

Bars were machine cut at the rectangular end into a small square sheet. The sheet thickness was about 4~5mm to avoid materials waste and ensure there was enough material for grinding and polishing processes. The barrel samples from hot compression tests were cut from the top middle so that the whole cross section surface can be characterized, as shown in Figure 3.7. A vertical cutting mode and 3800rpm speed of the cutting wheel were applied. Square sheet samples were then hot mounted in conductive Bakelite using Buehler SimpliMet 1000. The mounting process included 4mins heating ramp, 10mins holding time at 180°C and 4mins cooling.



Figure 3.7 Barrelled samples

3.4.2 Grinding and Polishing

The mounted samples were then ready for grinding. The grinding followed a sequence of 300, 600, 900 and 1200 grit. After the final 1200 grit grinding, the samples were OM checked to ensure there is no undesired scratches. Polishing is carried out with an initial polish using $1\mu\text{m}$ diamond paste and a final polish using $0.05\mu\text{m}$ colloidal silica suspension. Both polish step takes minimum of 20 mins depending on characterisation techniques applied afterwards. For example, 20 mins will be enough for SEM imaging and 30mins would be needed if EBSD is required. Lastly, an OM check is necessary, again, to make sure the sample surface is free of scratches.

3.4.3 Etching and Further Polish

To reveal specific microstructure features, there are two types of etchants used in this project.

1) Kalling's reagent No. 2 etchant is used on Haynes 282 alloy to show its grain boundaries. The chemical composition of Kalling's reagent No. 2 is stated in Table 3.2. Moreover, Kalling's

reagent No. 2 etches the grain boundaries and γ' precipitates. During etching, the specimen was directly smeared the etchant on top of the sample while holding it flat, the etching time was between 10 and 20 seconds. This method, compared with immersion, proved to be more advantageous as the sample surface is visible so that can avoid over etching. Also, to avoid over etching, the sample needs to be rinsed immediately with water and then to be dried with ethanol.

Table 3.2 Chemical compositions of etchants

Etchant	Chemical composition	Etching method
Kalling's reagent No.2	1g $CuCl_2$ +20mL HCl+ 20mL C_2H_6O	Smear or immersion
10% Phosphoric Acid	10% phosphoric acid + 90% H_2O	Electric etching

2) The second etchant used is 10% phosphoric acid to reveal the γ' precipitates. Different from Kalling's reagent No. 2, phosphoric acid can remove γ matrix to show the γ' precipitates. A Kristall 680 Electrolytic etcher with an external etching unit is used, see Figure 3.8. The etching



Figure 3.8 Kristall 680 Electrolytic Polisher and Etcher

is carried out at a voltage of 10V and run time of 1-2mins depending on the conductivity of the sample.[1]

Further polish is needed if the sample is being taken to EBSD analysis. There are two types of such polish techniques available in the lab, vibration polish and ion milling polish. In this project, ion milling polish is used as it is more efficient than vibration polish. The ion milling process was performed on Hitachi Broadbeam Ion miller in flat milling mode to obtain high quality EBSD characterisation. The sample was polished by an ion beam to obtain a perfectly flat surface. Since nickel alloys are relatively hard, a milling time of 10mins and a milling voltage of 6kV were selected. Also, a rotated stage and 80° beam angle were used.

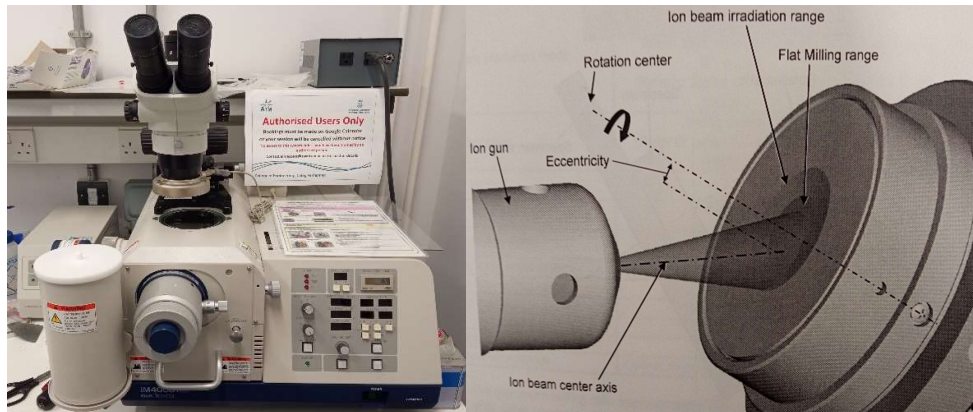


Figure 3.9 Hitachi Broadbeam IM4000 Milling System and flat milling illustration

3.4.4 TEM Sample Preparation

TEM sample preparation is a lot more complicated than SEM sample preparation. The first thing to consider is what kind of specimen is needed. This refers to whether it is a self-support disk or on a grid. The diagram below summarizes the different preparation methods. In this project, self-support disks were made.

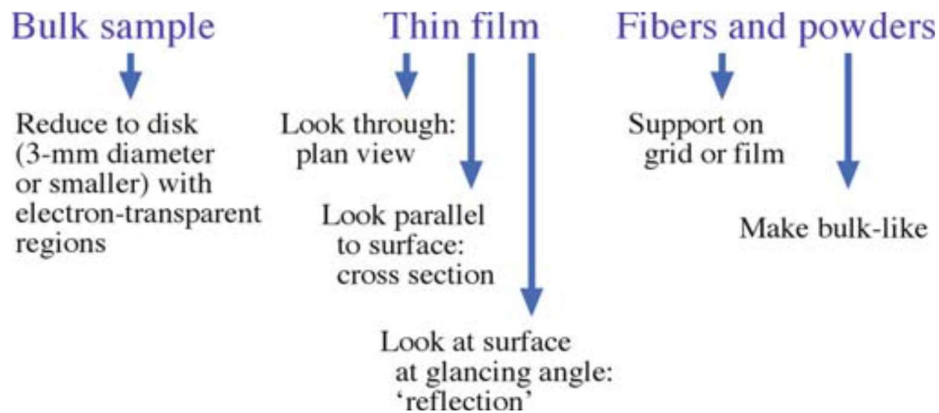


Figure 3.10 Diagram of different situations and their preparation philosophies [2]

The process of making self-support disks includes three steps.

- 1) Initial thinning. A slice of material with a thickness of 100-200 μ m was made first. Usually, the slices are obtained using a chemical wire/string saw, razor blade or diamond wafering saw depending on the ductility of the materials. The slices were made using a cutting machine with a thinner cutting wheel, and then the slice was fitted onto a grinding holder using wax and paper ground down to 100-200 μ m.
- 2) Second step is cutting a 3mm disk from slices. Methods include mechanical punch, spark erosion and grinding drill. It should be noted that all mechanical thinning will introduce surface damage. In this project, a mechanical punch was used, see Figure 3.11.

3) Last step is final thinning. A mechanical dimpler was used to thin the disk centre area further down to 50 μ m ideally. The final thinning process was achieved either by electropolishing or ion milling. Electropolishing was applied in this project as it is more efficient than Ion milling. The electropolishing system consists of a Julabo 900F external chiller and a Tenupol-5 twin-jet polisher, see Figure 3.12. A twin-jet polisher can pump electrolytes onto both sides of the disk. A light pipe can detect the perforation and stop the process. Once polishing was finished, the disk was taken out and rinsed with ethanol immediately to avoid further etching caused by residual electrolytes [2]. The electrolyte, 30% perchloric acid, was carefully poured into the tub, and then the chiller will start to bring the temperature down to -20°C. The polish can only proceed once the target temperature is reached. The polishing process used a voltage of 20V, a light stop value at 150mA and dual step mode was applied with an initial flow rate of 15 for 15 seconds followed by a final flow rate of 10.

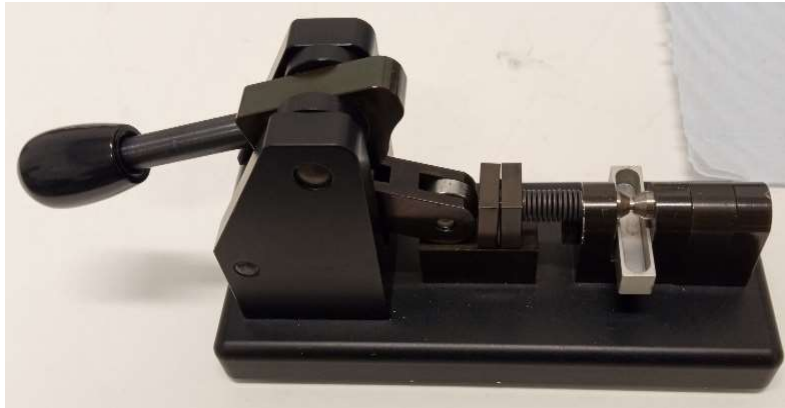


Figure 3.11 Mechanical punch for disk cutting



Figure 3.12 Julabo 900F external chiller and Tenupol-5 Twin-Jet polisher

3.5 Characterisation Techniques

Several characterisation techniques were applied in this project, these include, as mentioned in the sample preparation part, OM (optical microscope), SEM (scanning electron microscope), EBSD (electron backscattered diffraction) and TEM (transmission electron microscope). The microscope and technique details will be explained. All these facility training and management were provided by AIM (Advanced Imaging of Materials) at Swansea University.

3.5.1 Optical Microscope (OM)

OM was used either for the examination of sample preparation or for grain size analysis. The microscope used for sample examination is a Zeiss Primotech with magnification capability of 10x, 20x and 50x. This microscope was used between grindings and polishings to ensure a

perfect surface.

Grain characterisation was carried out on a Zeiss Compound Microscope fitted with Zeiss ZEN core software. This software is fitted with a grain size analysis function. The Intercept method was attempted. This method draws several straight lines across the image, then the grains that are intercepted with those lines will be counted. And finally, the average grain size in the area will be calculated. Figure 3.13 shows the OM microscopes based in Swansea University.



Figure 3.13 Zeiss Primotech microscope(left) and Zeiss Compound microscope(right)

3.5.2 Scanning Electron Microscope (SEM)

The SEM used in this project is a JEOL FSM-7800F microscope equipped with a Field Emission Gun (FEG). The microscope, part of the Advanced Imaging of Materials (AIM) at Swansea University, is fitted with EDX, WDS and EBSD detectors, and is capable of high-resolution characterisation. In this project, the JEOL SEM is used to characterise γ' precipitates.

Besides, the key parameters include working distance, accelerating voltage, probe current and probe size. Working distance is the distance between the pole piece of the final lens to the

sample. Working distance will affect the image quality geometrically. Accelerating voltage determines the strength of the electron signal, the higher the voltage the stronger the signal. And stronger signal will provide more information from the subsurface. The probe current will directly influence the brightness of the image, the higher the current the brighter the image. Probe size is determined by the gun source. Probe size limits the image resolution, the smaller the size the higher the resolution. For FEG the probe size is about 0.2nm. In this project, SEM high resolution images were obtained using working distance between 5mm-10mm, accelerating voltage range 5kV-10kV, probe current 6nA-8nA.

3.5.3 Electron Backscattered Diffraction (EBSD)

EBSD is a characterisation technique that relies on SEM. It provides various information about the crystallographic nature of the sample. For example, phase determination, grain orientation, grain size distribution, recrystallization fraction, grain boundary misorientation, etc. The SEM characterisation makes use of the secondary electrons while the EBSD makes use of backscattered electrons. The backscattered electrons go deeper into the surface than secondary electrons, and they will be diffracted from the sample and collected by a charge couple device (CCD) camera. The schematic illustration in Figure 3.14 shows the general set up of an EBSD system[3]. The phosphor screen can transfer the diffracted electron into light that is able to be recorded by the camera. Apart from the screen and camera, an EBSD detector also equips several silicon diodes. The diodes, also called Forward Scatter Detectors (FSD), are tools for previewing the microstructure to select a region for EBSD data collection.

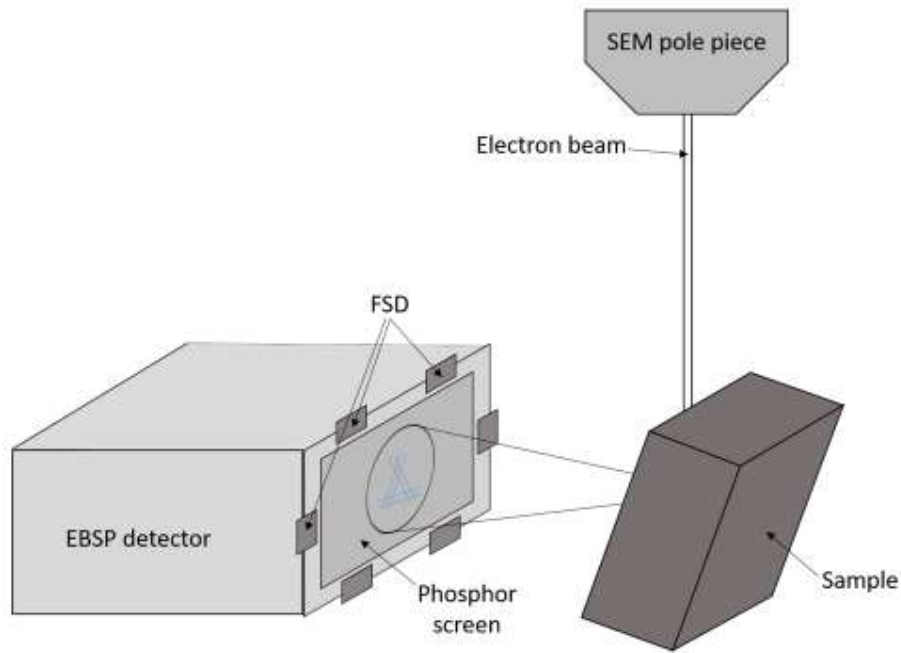


Figure 3.14 Schematic of set up of EBSD system [3]

As mentioned, EBSD uses diffracted information, and hence, Bragg's law plays an important role in this technique. When the electrons reach the surface and subsurface, they interact with crystal lattices and be diffracted. The incident angle between some electrons and crystal plane satisfies the Bragg equation:

$$n\lambda = 2d \sin \theta \quad (3.1)$$

where n is an integer, λ is beam wavelength, d is interplanar space and θ is the electron incident angle. Those electrons will be diffracted in all directions and form diffractive cones and conical rings. Then, the phosphor screen intercepts with those cones and a flat Kikuchi pattern is formed, see Figure 3.15. The Kikuchi patterns are the projection of spherical Kikuchi maps and the curved Kikuchi bands approximate straight bands as the incident angle θ is small ($\sim 20^\circ$)[4].

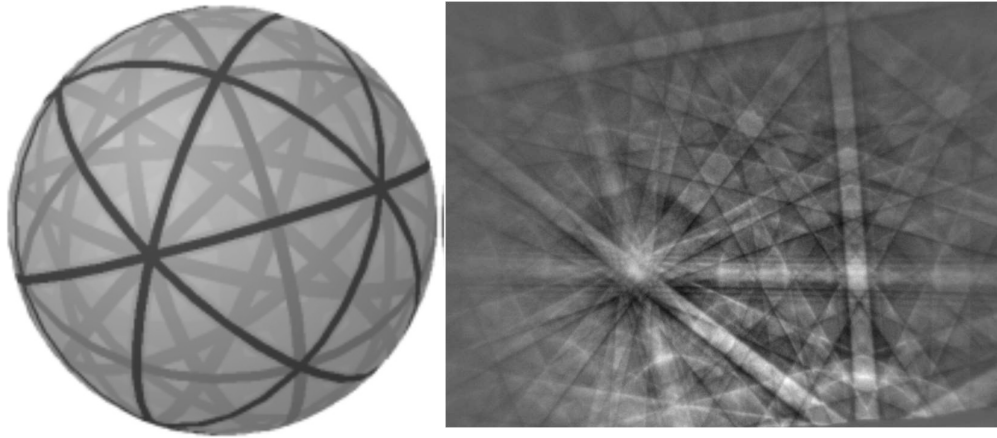


Figure 3.15 A spherical Kikuchi map and a flat Kikuchi pattern [4]

Subsequently, the raw Kikuchi pattern on the phosphor screen is recorded by a CCD camera and converted to the Aztec software for acquisition. Prior to the acquisition, there is a final processing which includes a Hough Transform and an optimization to ensure the accuracy of the pattern index.

In this project, EBSD analysis horizontally tilted sample 70° , in which the incident angle of the electrons is 20° . SEM working distance was set at about 18mm-20mm, accelerating voltage at 20kV, probe current at 14A, EBSD mapping step size of $2.0\mu\text{m}$.

3.5.4 Transmission Electron Microscope (TEM)

TEM is a powerful technique that can achieve super high resolution at the atomic level ($2\sim 3.5\text{\AA}$). Different from SEM, electrons in TEM penetrate thin samples, are captured by a fluorescent screen, and are recorded by a CCD camera. Therefore, the sample preparation and electronic system are different from SEM as well. First, the samples of TEM are normally a thin 3mm disk, thin film or powders on a grid as mentioned in part 3.4.4. In addition, the maximum accelerating voltage is 200 kV and the beam energy range is between 40 keV and 200 keV. Thus the accelerated electrons can penetrate the sample with a certain thickness.

Lastly, similar to EBSD, TEM collects information from diffracted electrons as well. In this study, TEM was used to characterize γ' precipitates (tertiary γ' to be exact) to conduct precipitation size analysis. TEM characterisation was carried out on an FEI Talos F200X TEM/STEM system, as shown in Figure 3.16. A single tilt sample holder and an accelerating voltage of 200kV were used. [5]

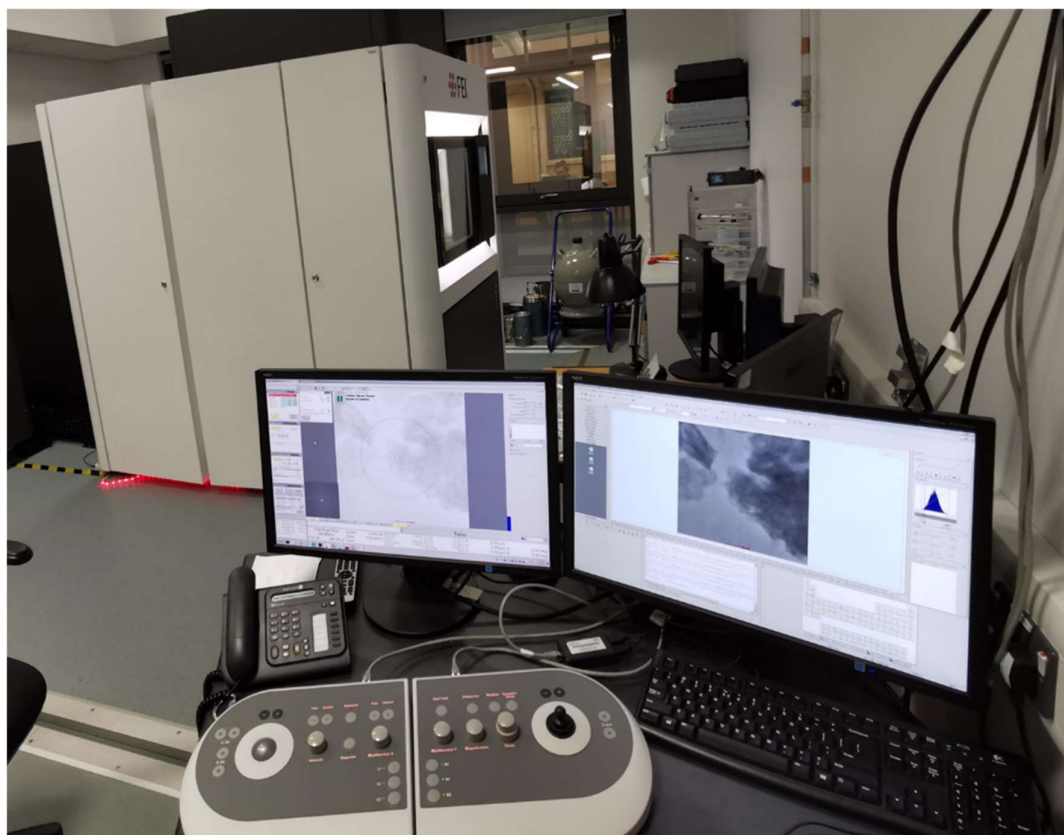


Figure 3.16 FEI Talos F200X TEM/STEM system based in AIM Swansea

3.6 Measurement Methods

3.6.1 Grain Size Measurement

The grain characterisation and size analysis were performed by OM with Zeiss ZEN Core software. An ASTM standard was applied to present the results of grain sizes. The ASTM grain size standard can be expressed by the equation below,

$$n = 2^{G-1} \quad (3.2)$$

where n is the number of grains per in^2 at 100X, and G is the ASTM grain size number. However, there are several different criteria within the ASTM standard. See table 3.3 below, it shows several standards that are commonly used.

Table 3.3 Criteria to determine grain size in ASTM standards[6]

ASTM E 112	For equiaxed, single grain structures
ASTM E 930	For grain structures with an occasional very large grain
ASTM E 1181	For characterising duplex grain structures
ASTM E 1382	Standard test methods for determining average grain size using semiautomatic and automatic image analysis

As can be seen from Table 3.3, ASTM E 112 series applies for equiaxed and single grain structure materials such as single crystal silicon, single grain metals (nickel-based superalloys or titanium alloys) and single crystal semi-conductors; ASTM E 930 applies for materials that have occasional very large grain, for example, polycrystalline metals such as aluminium, copper and steel, Ceramics and polycrystalline alloys such as nickel-based superalloys, titanium alloys and aluminium alloys. In the case of materials exhibiting duplex grain structures, including dual-phase steels, dual-phase titanium alloys, and duplex stainless steels, the

utilization of the ASTM E 1181 standard represents an optimal choice. Finally, the ASTM E 1382 standard is used when image analysis software is applied.

Overall, the ASTM E 112 criterion is preferred for Haynes 282 grain size analysis, since compared to materials that have large grains, Haynes 282 possesses a relatively equiaxed grain structure, especially for samples after solution treatment.

There are 3 ways to measure the grain size through Zeiss software.

(1) Jeffries Planimetric Method. This is the first grain size measurement method that was created in 1916 by Zay Jeffries[6]. The method is defined and correlated with ASTM standard via the following equations.

$$N_A = f \left(n_1 + \frac{n_2}{2} \right) \quad (3.3)$$

$$A = \frac{1}{N_A} \quad (3.4)$$

$$G = (-3.322 \log_{10} A) - 2.955 \quad (3.5)$$

n_1 : number of grains completely inside the test circle

n_2 : number of grains intercepting the circle

f : Jeffries Multiplier=magnification² / circle area

A : average grain area

Figure 3.17 is an example of Jeffries Planimetric method[7]. It is demonstrated that a circle is drawn and crossed grains, then n_1 and n_2 can be counted as 68 and 41 respectively. Assume that the magnification and circle area is known, and then the ASTM size number G can be calculated.

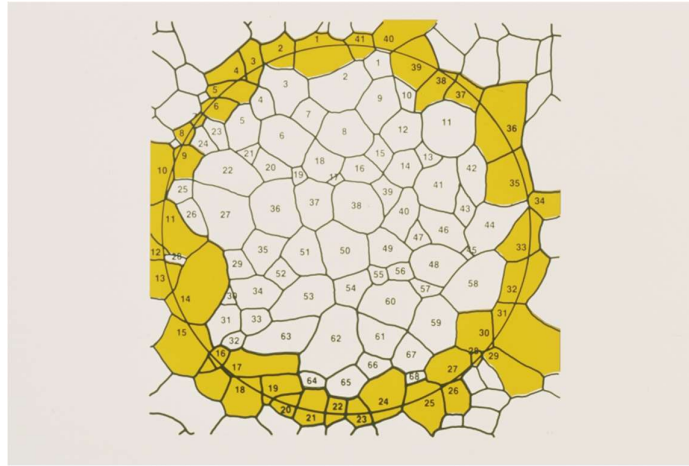


Figure 3.17 example of Jeffries Planimetric Method[7]

(2) **Comparison method** was first developed to simplify the Planimetric method. A comparison chart of copper at 75X was first added in the 1930s and with decades of development, various charts were added. An example size chart is given in Figure 3.18, this is an 8 charts ocular lens and can be used with a microscope for visual comparison[8]. However, the comparison in this study is achieved using Zeiss ZEN Core software.

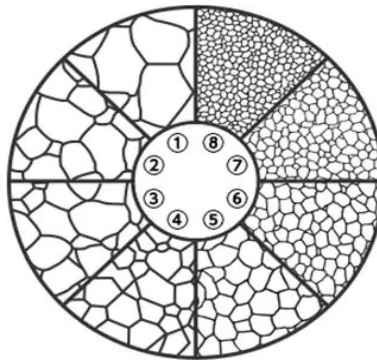


Figure 3.18 A grain size comparison chart for ocular lens, used with a microscope[8].

(3) Heyn / Hilliard / Abrams Intercept Method is normally known as the interception method. Examples are given in Figure 3.19, in which several lines or circles are drawn and the grain size can be calculated either through (a) counting (N) the grains intercepted by the lines or (b) counting (P) the grain boundaries intersections[7].

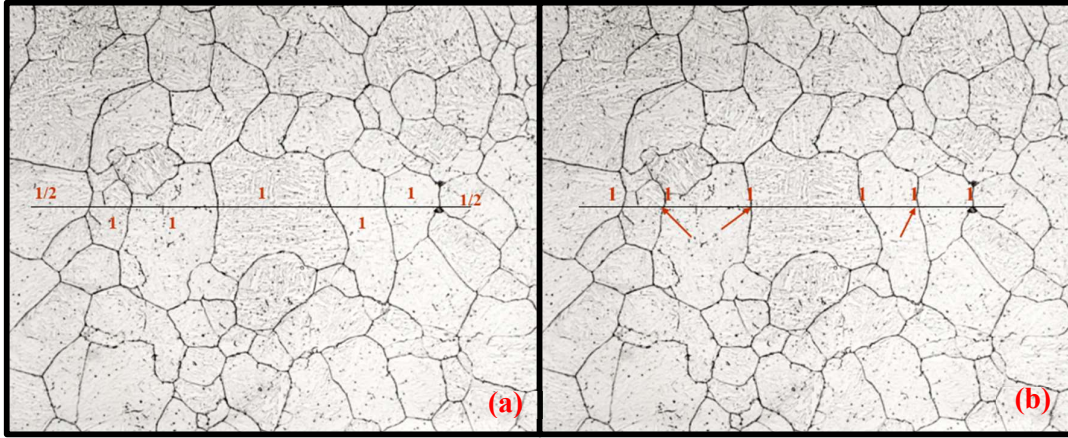


Figure 3.19 Example of Heyn / Hilliard / Abrams Intercept Method with (a) grains counting and (b) grain boundaries counting [7]

The ASTM grain size number can be calculated by the following equations[6].

$$l = \frac{1}{N_L} = \frac{1}{P_L} \quad (3.6)$$

$$G = [6.644 \log_{10}(N_L \text{ or } P_L)] - 3.288 \quad (3.7)$$

$$G = (-6.644 \log_{10} l) - 3.288 \quad (3.8)$$

l : Mean Lineal Interception

N_L : Number of grains intercepted (N) divided by true line length

P_L : Number of grain boundaries intersections (P) divided by true line length

A grain size table correlated with actual sizes is listed below[9].

Table 3.4 ASTM E112-13 Grain Size Relationships Computed for Uniform, Randomly Oriented, Equiaxed Grains[9]

Grain Size No. G	N_A Grains/Unit Area		\bar{A} Average Grain Area		\bar{d} Average Diameter		\bar{L} Mean Intercept		\bar{R}_L
	No./in. ² at 100X	No./mm ² at 1X	mm ²	μm ²	mm	μm	mm	μm	
00	0.25	3.88	0.2581	258064	0.5080	508.0	0.4525	452.5	2.21
0	0.50	7.75	0.1290	129032	0.3592	359.2	0.3200	320.0	3.12
0.5	0.71	10.96	0.0912	91239	0.3021	302.1	0.2691	269.1	3.72
1.0	1.00	15.50	0.0645	64516	0.2540	254.0	0.2263	226.3	4.42
1.5	1.41	21.92	0.0456	45620	0.2136	213.6	0.1903	190.3	5.26
2.0	2.00	31.00	0.0323	32258	0.1796	179.6	0.1600	160.0	6.25
2.5	2.83	43.84	0.0228	22810	0.1510	151.0	0.1345	134.5	7.43
3.0	4.00	62.00	0.0161	16129	0.1270	127.0	0.1131	113.1	8.84
3.5	5.66	87.68	0.0114	11405	0.1068	106.8	0.0951	95.1	10.51
4.0	8.00	124.00	0.00806	8065	0.0898	89.8	0.0800	80.0	12.50
4.5	11.31	175.36	0.00570	5703	0.0755	75.5	0.0673	67.3	14.87
5.0	16.00	248.00	0.00403	4032	0.0635	63.5	0.0566	56.6	17.68
5.5	22.63	350.73	0.00285	2851	0.0534	53.4	0.0476	47.6	21.02
6.0	32.00	496.00	0.00202	2016	0.0449	44.9	0.0400	40.0	25.00
6.5	45.25	701.45	0.00143	1426	0.0378	37.8	0.0336	33.6	29.73
7.0	64.00	992.00	0.00101	1008	0.0318	31.8	0.0283	28.3	35.36
7.5	90.51	1402.9	0.00071	713	0.0267	26.7	0.0238	23.8	42.04
8.0	128.00	1984.0	0.00050	504	0.0225	22.5	0.0200	20.0	50.00
8.5	181.02	2805.8	0.00036	356	0.0189	18.9	0.0168	16.8	59.46
9.0	256.00	3968.0	0.00025	252	0.0159	15.9	0.0141	14.1	70.71
9.5	362.04	5611.6	0.00018	178	0.0133	13.3	0.0119	11.9	84.09
10.0	512.00	7936.0	0.00013	126	0.0112	11.2	0.0100	10.0	100.0
10.5	724.08	11223.2	0.000089	89.1	0.0094	9.4	0.0084	8.4	118.9
11.0	1024.00	15872.0	0.000063	63.0	0.0079	7.9	0.0071	7.1	141.4
11.5	1448.15	22446.4	0.000045	44.6	0.0067	6.7	0.0060	5.9	168.2
12.0	2048.00	31744.1	0.000032	31.5	0.0056	5.6	0.0050	5.0	200.0
12.5	2896.31	44892.9	0.000022	22.3	0.0047	4.7	0.0042	4.2	237.8
13.0	4096.00	63488.1	0.000016	15.8	0.0040	4.0	0.0035	3.5	282.8
13.5	5792.62	89785.8	0.000011	11.1	0.0033	3.3	0.0030	3.0	336.4
14.0	8192.00	126976.3	0.000008	7.9	0.0028	2.8	0.0025	2.5	400.0

The accuracy of the measurement methods has been discussed and even criticised for decades. While These standards generally cannot be evaluated as they do not have a referee method within the standard[6], the ASTM standard is reliable when it is applied for comparison purposes. In this study, the Interception method was used as the main tool for grain size analysis. The other two methods were conducted for “standard heat treatment” only for data validation. Also, EBSD characterisations and HKL Channel 5 grain size analysis was carried out to reveal the further grain size distribution.

3.6.2 Precipitation Measurement

The size of the precipitate was measured in diameter, and each measurement was drawn horizontally. An example of standard treatment is given in Figure 3.20. In this micrograph, each precipitation size was measured horizontally as marked by red lines. 50 Particles were picked for each sample and measurements were recorded in the image analysis software, ImageJ.

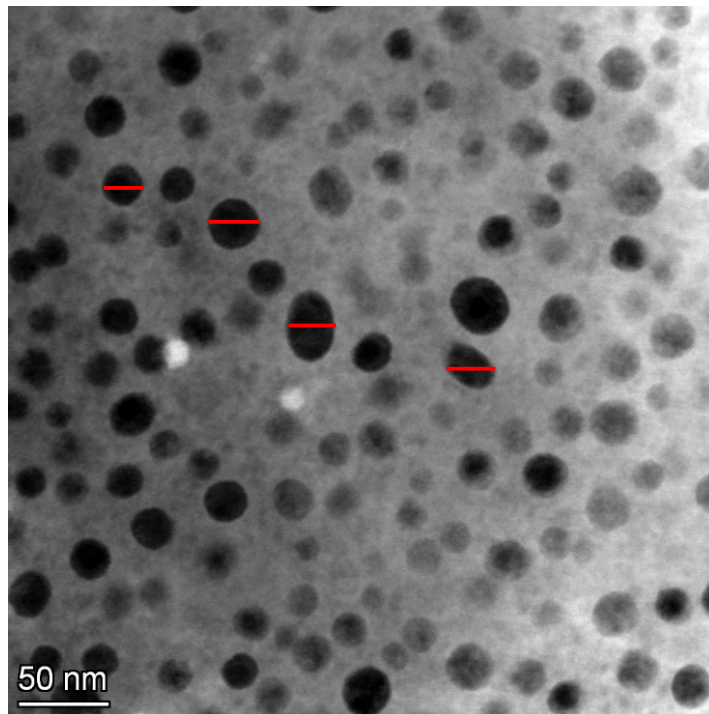


Figure 3.20 STEM bright field image of standard treatment sample

Chapter 4 Results

A series of heat treatments were designed with different aging times and temperatures, to study the evolution of grains and precipitation coarsening during aging as described in Chapter 3.2. Three groups with 730°C, 830°C and 930°C aging temperatures with different aging times were carried out. These aging temperatures were picked according to the equilibrium phase diagram of Haynes 282 as illustrated in Chapter 2.2. This chapter will state the experimental results of static heat treatments and dynamic hot compression tests. The mechanism of grain evolution and characterisation results will be illustrated in Chapter 4.1. The precipitation coarsening mechanism will be discussed in Chapter 4.2 and followed by the experimental results. Chapter 4.3 will explain the recrystallisation mechanism of nickel-based alloys and will illustrate the mechanical testing and characterisation results.

4.1 Grain Evolution in Static Heat Treatments

Prior to the grain size analysis, the grain size measurement standard and techniques were investigated. The details has been described in Chapter 3.6.1.

The as-received Haynes 282 was manufactured through a 2-pass ring-rolling forge process, as mentioned in Chapter 3.1. Figure 4.1 (a) is as-received materials, in which it can be seen that the grains are compressed and squeezed along the ring-roll direction after ring-roll forging. This leads to a columnar grain feature. Figure 4.1 (b) illustrates the microstructure of solution annealed samples. After solution treatment, the microstructure is annealed and equiaxed. Because the equiaxed grains possess the best strength but lower plasticity while the columnar grains possess the best plasticity but lower strength[1]. Therefore, nickel superalloys, as elevated-temperature materials, normally need post heat treatments.

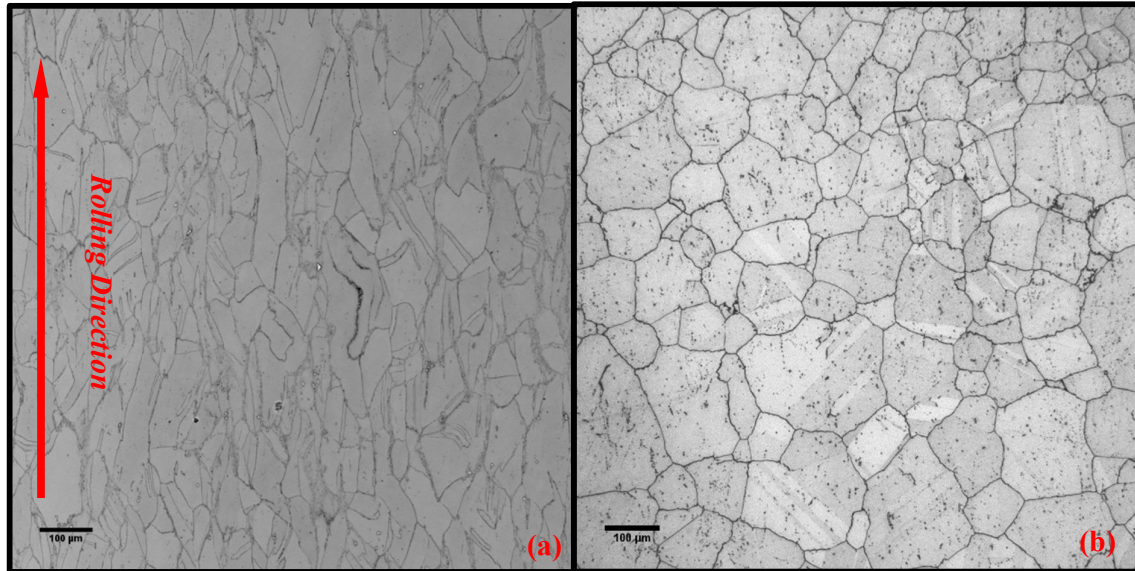


Figure 4.1 Optical images of (a) as-received sample with columnar grains; (b) Sample solution treated at 1121°C for 30mins with equiaxed microstructure

The standard heat treatment includes a 2-step aging process after solution treatment. Figure 4.2 shows the microstructure of the standard treatment sample. Compare to the solution treated sample, there was no significant grain growth. It should be noted that plenty of small grains recrystallized as highlighted with red circles, which indicates that the AGG happened during the heat treatment. A group of SEM images shows the grain boundary carbides were well dissolved into the matrix after the solution (Figure 4.3(a)) and well precipitated out after standard heat treatment (Figure 4.3(b)). Figure 4.3, on the other hand, proved the successful solution treatment and the standard heat treatment.

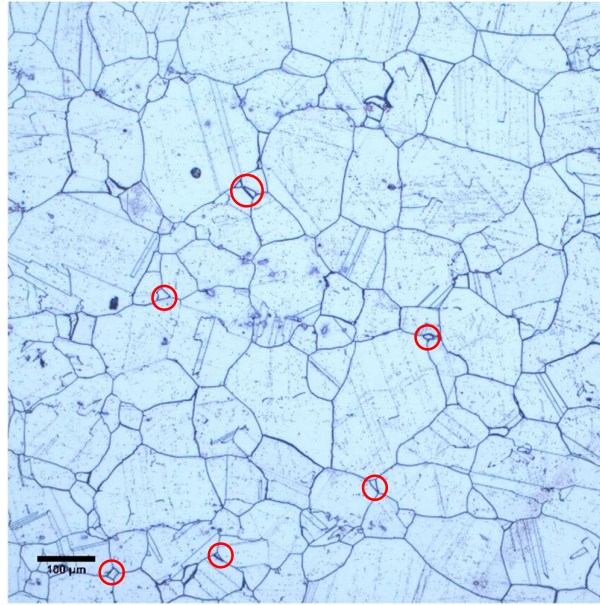


Figure 4.2 Optical image revealing the grain evolution of standard heat treatment after solution treatment

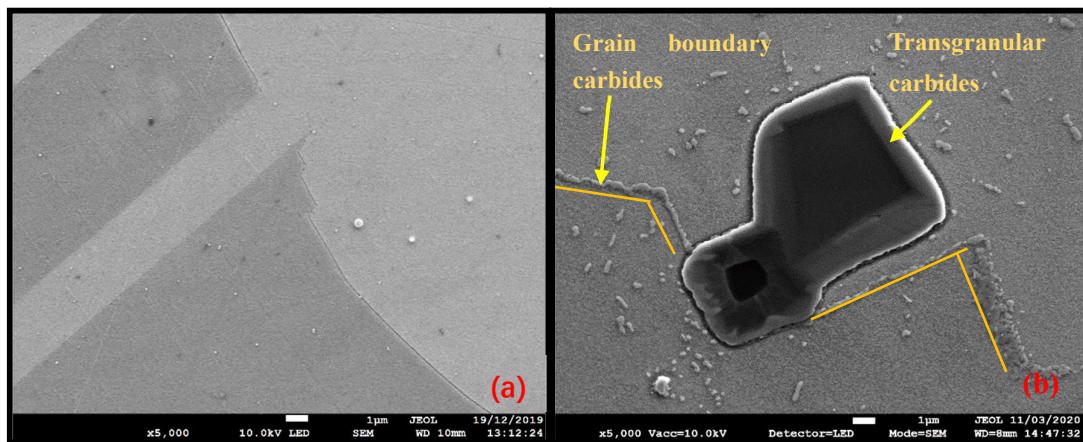


Figure 4.3 (a) Solutioned sample captured under SEM showing a microstructure free of boundary carbides; (b) Grain boundary carbides and a large transgranular carbide spotted after standard heat treatment

The images of standard treatment were then analysed with regard to the grain size afterwards. And three methods were applied to standard treated samples.

An example image analysed by **Jeffries Planimetric Method** is shown in Figure 4.4. A circle was drawn randomly on 3 images with blue dots marking the intercepted grains and yellow dots marking the grains within the circle. In this image, $n_1=37$, $n_2=27$ (n_1 : number of grains completely inside the test circle, n_2 : number of grains intercepting the circle), magnification calculated at 135X and circle area calculated at 0.5mm^2 . And according to equation (3.3), (3.4) and (3.5), ASTM grain size No. $G=3.62$. Referring to Table 3.4, the average grain diameter is just below $106.8\mu\text{m}(G=3.5)$. Table 4.1 summarizes the essential values of this method.

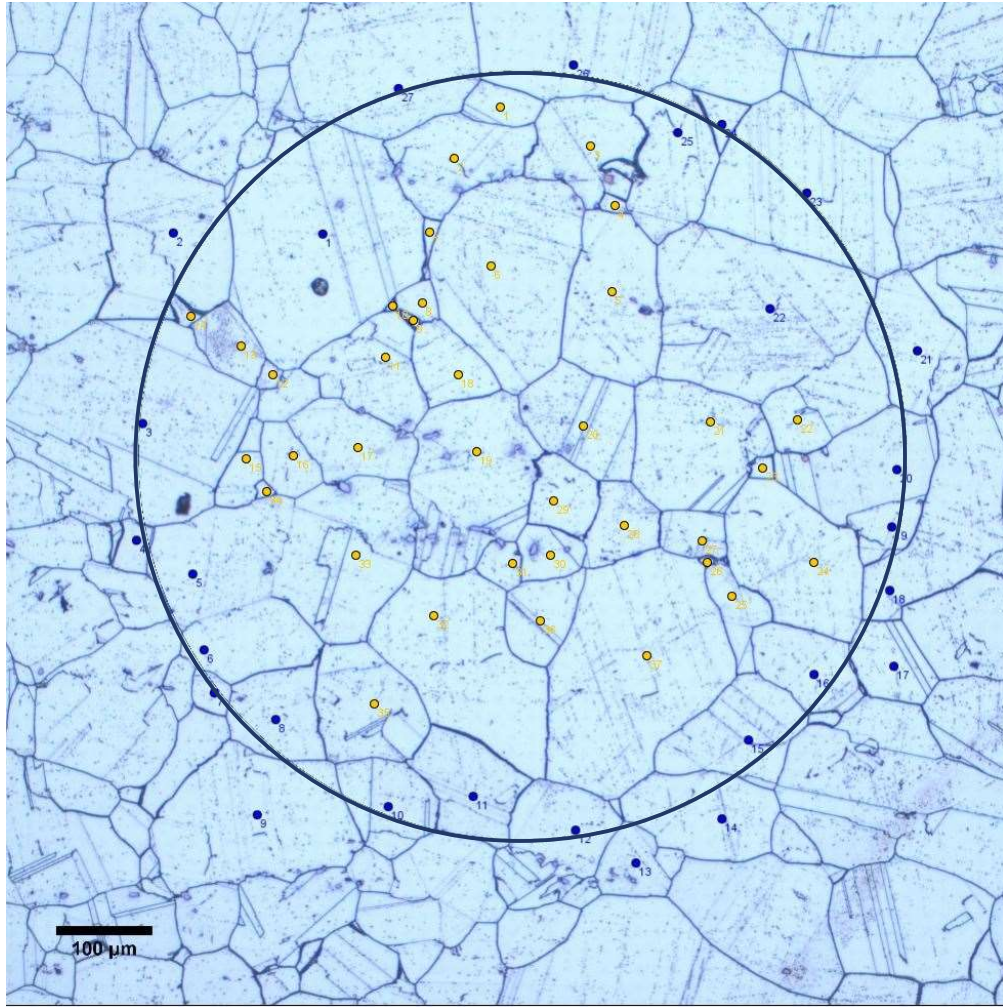


Figure 4.4 Image of standard treated sample analysed by Jeffries Planimetric Method

Table 4.1 Values obtained and calculated in Jeffries Planimetric method

scale bar(mm)	0.10	image	whole grains	half grains	total
scale bar length(mm)	13.50	1	37.00	27.00	50.50
magnification	135.00	2	32.00	25.00	44.50
radius length(mm)	54.00	3	35.00	28.00	49.00
radius(mm)	0.40	Mean	34.67	26.67	48.00
Area(mm ²)	0.50	Na=Grains in Area/mm ²	95.49		
Jeffries factor	1.99	G	3.62		

The **comparison method** was conducted on the Zeiss ZEN Core software, an example image that illustrates this method was captured, see Figure 4.5. Four images from the software database were placed around the analysed image. In this case, the grain size that was analysed lies between the image of No.3 and No.4. It should be noted that the size of relatively big grain is close to No.3 although the small grains are smaller than those in No.3 image. Therefore, the grain size can be determined between No.3 to 4 by means of the comparison method, where the diameter lies between 89.8µm-127µm according to Table 4.2.

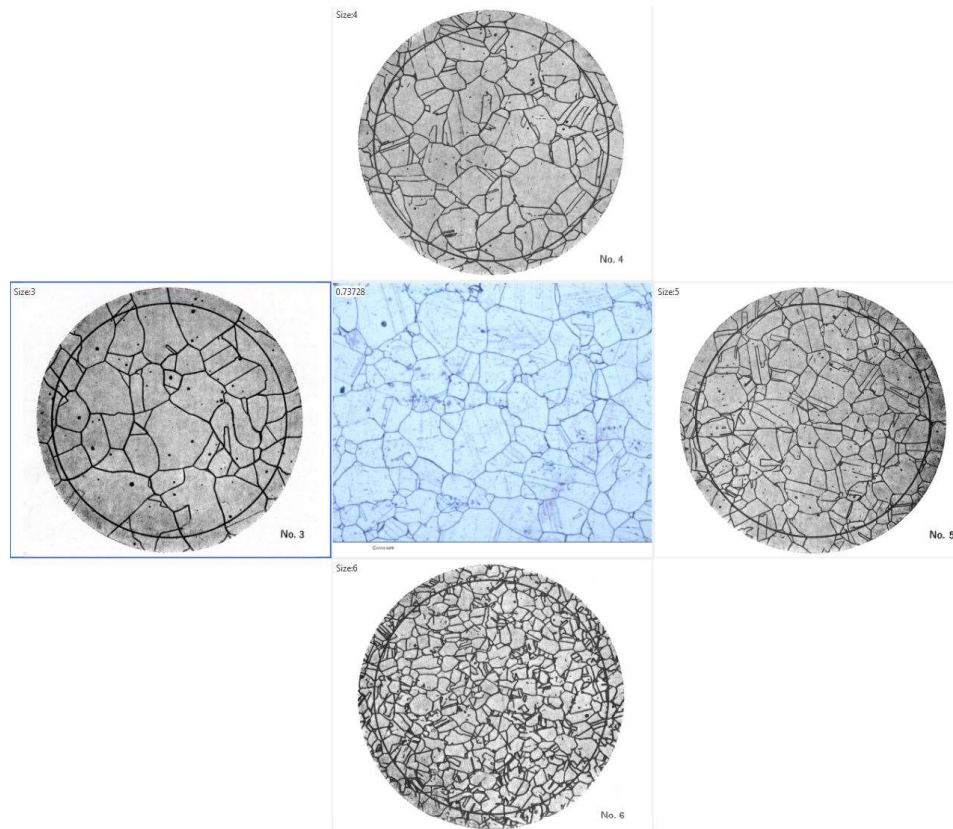


Figure 4.5 Comparison method to determine the grain size

The **interception method** was also finished on Zeiss ZEN Core software. 3 images were analysed per sample and 5 interception lines were drawn on each image. The results were calculated by software and a report can be exported. Figure 4.6 shows the 5 parallel lines and red dots that mark the intersections of those lines and grain boundaries. The total intercept length on one image is 4044.404 μ m. Tables 4.2 and 4.3 are the summarised results showing a mean grain size No.4. A further calculation was carried out according to equation 4.6 to get more accurate results, see Table 4.4.

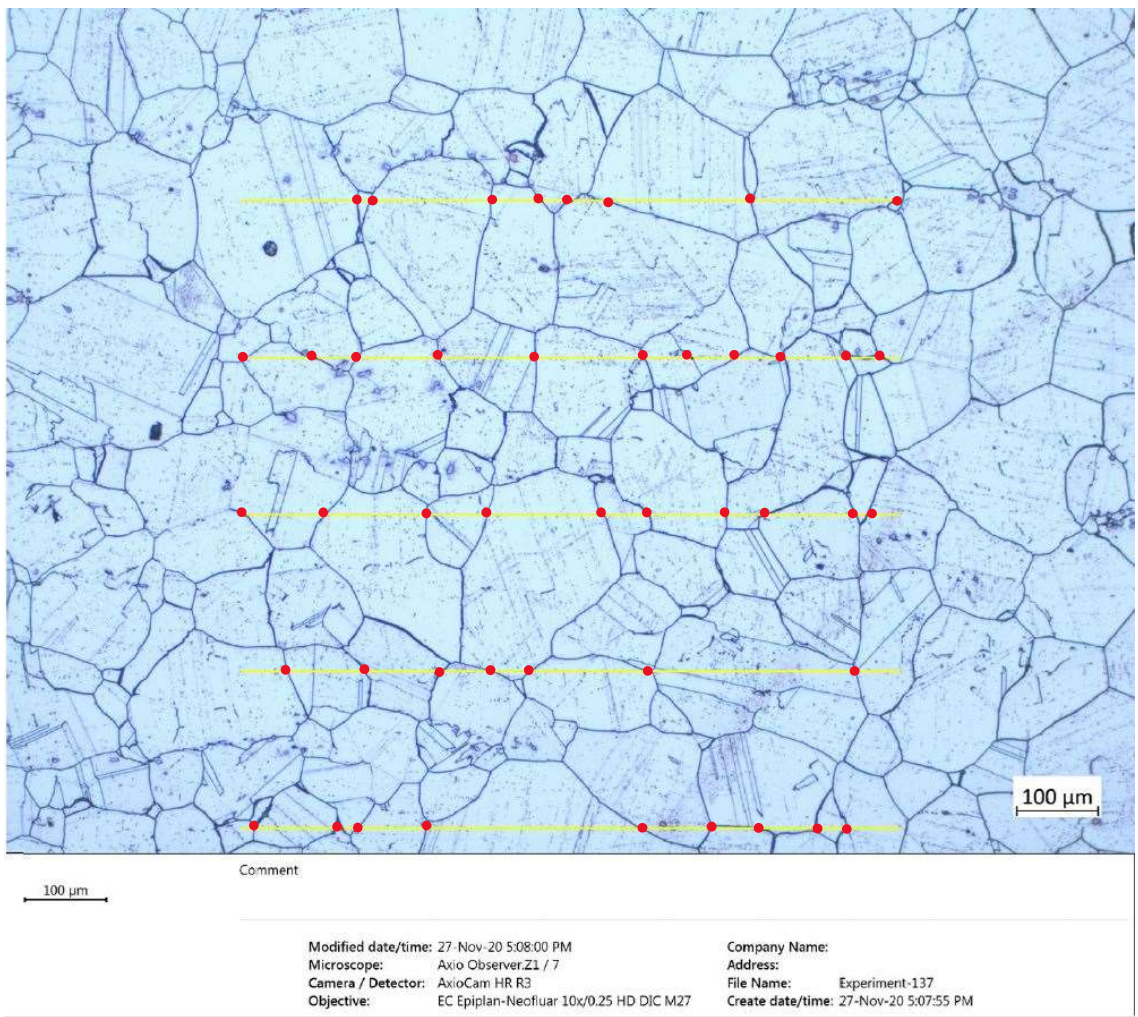


Figure 4.6 Image with interception line and red dots indicating grain boundary intersections

Based on the results from 3 grain size analysis methods, a grain size No. between 3-4 can be concluded. The Jeffries Planimetric method and Interception method provide more precise results of 3.62 and 3.77 respectively. It is worth mentioning that while there are deviations in Table 4.3, they are not available in further calculations shown in Tables 4.4 and 4.5. However, the errors were minimised by collecting enough data. For example, in the interception method, minimum of 3 images were used and 5 interception lines were applied on each image. Additionally, each image included approximately 50 interceptions.

Table 4.2 Interception method results for 3 images

Image	Grain Size No. [μm^2]	Number of Intersections
Image 01	3.5	46
Image 02	4.0	50
Image 03	4.0	51

Table 4.3 Summary of interception method

Mean Grain Size No.	Total Intercept Length [μm]	Standard Deviation
4.0	12133.212	0.248

Table 4.4 A further calculation using equation 3.7

numebr of intersections	46	50	51
interception length(mm)	4.791	3.997	3.997
R_i	9.60	12.51	12.76
G	3.24	4.00	4.06
Mean	3.77		

The grain evolution analysis of Haynes 282 after static heat treatments, carried out using an optical microscope, provides insights into the microstructural changes. Figure 4.7 offers an overview of the observed grain evolution, showing the effects of different heat treatment conditions. To support this analysis, Table 4.5 and Figure 4.8 present detailed quantitative data, offering a more comprehensive understanding of the grain size evolution.

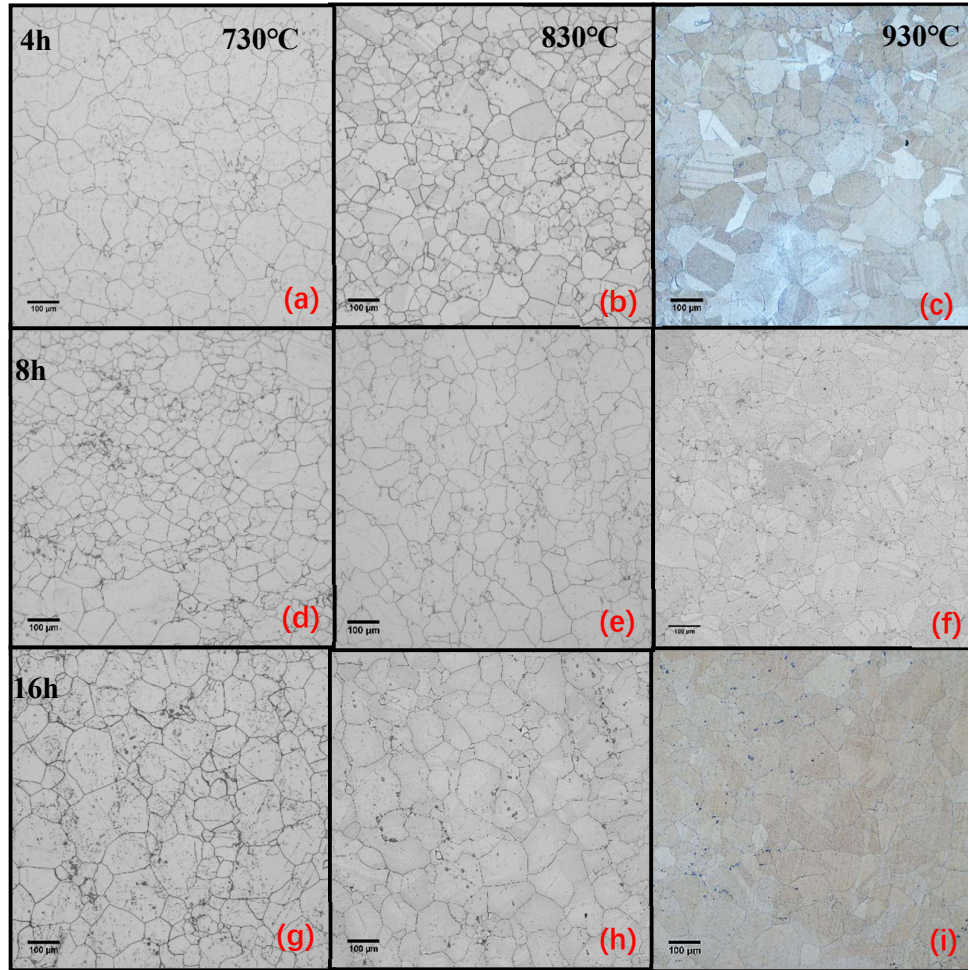


Figure 4.7 OM images of 9 1-step aging heat treatments, (a) 730°C/4h; (b) 830°C/4h; (c) 930°C/4h; (d) 730°C/8h; (e) 830°C/8h; (f) 930°C/8h; (g) 730°C/16h ; (h) 830°C/16h; (i) 930°C/16h

As expected, the impact of temperature on grain size is evident, with higher temperatures promoting grain growth. For instance, in the 8-hour aging heat treatments, the grain size increased from an initial value of grain size No. 5.32 to No. 4.66. However, the grain growth behaviour in the 4-hour aging group is unusual, as the grains did not exhibit continuous growth. Nonetheless, it is interesting to note that even in this group, the largest grains were consistently observed at the temperature of 930°C. This suggests that specific thermal conditions play a crucial role in governing the dynamics grain growth in Haynes 282.

Furthermore, an examination of the impact of aging duration reveals that longer aging times generally result in larger grain sizes. Remarkably, the 16-hour aging provided the largest grains across all temperature groups. However, a notable exception to this trend is observed at 830°C and 930°C groups, where a decrease in average grain size is observed at 8-hour aging and an increase at 930°C. These contrasting observations can be attributed to the emergence of smaller grains, as visually confirmed by the optical microscope images. The relationship between grain growth, grain size distribution, and thermal conditions in Haynes 282 needs further investigation, which will be discussed in the subsequent chapter.

Table 4.5 Summarised ASTM E112-13 grain size No. corresponding to Figure 4.7

Temperature Time	730°C	830°C	930°C
4h	4.68	5.18	4.47
8h	5.32	5.1	4.66
16h	4.50	4.37	4.28

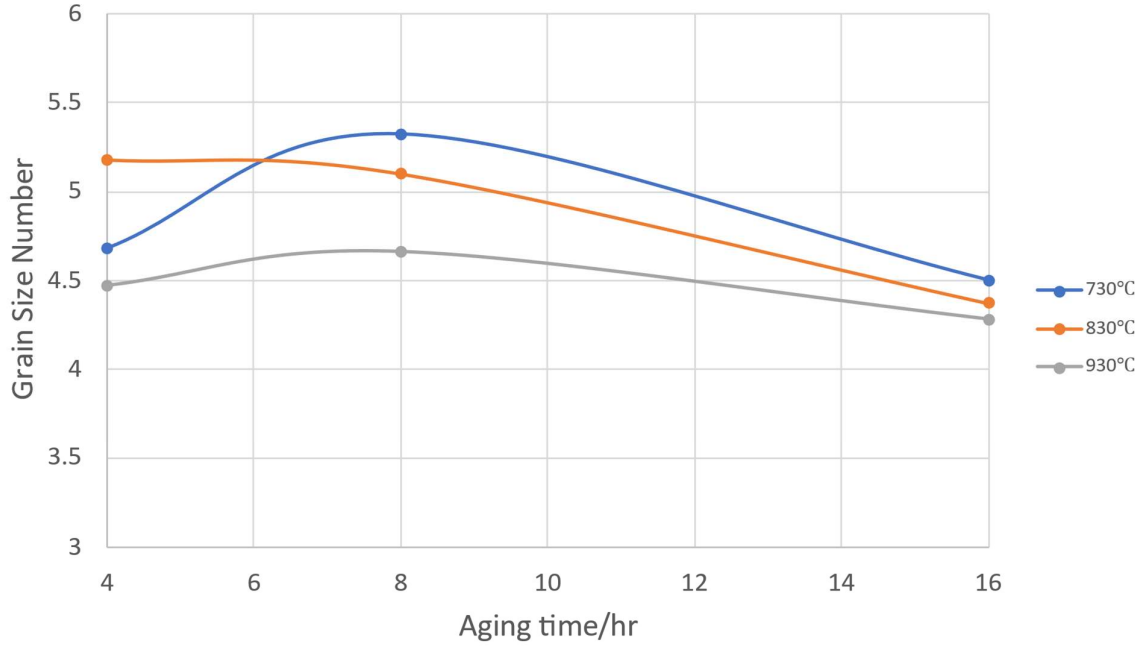


Figure 4.8 Diagram of grain size evolution for 1-step heat treatments

4.2 Precipitation Coarsening in Static Heat Treatments

Figure 4.9 presents an illustration of the evolution of precipitates during nine 1-step aging treatments conducted in this study. Evidently, substantial growth of particles occurs as the aging temperature increases. However, the precise value of precipitation size with varying aging times requires further characterization and measurements. In addition, the limited size of γ' precipitates in the 730°C group prevented obtaining accurate results. Hence, high-magnification images were acquired using TEM, as depicted in Figure 4.10.

A summary of the precipitate measurements is provided in Table 4.6. For instance, in the 730°C group, the average precipitation size, in terms of diameter, increased from 17.51nm to 23.49nm as the aging time progressed from 4 hours to 16 hours. Similar trends can be observed in the 830°C and 930°C groups. On the other hand, when comparing different aging temperatures within an 8-hour aging group, the precipitation size increased from 20.32nm to 85.08nm as the

temperature increased from 730°C to 930°C. Notably, in the 730°C and 830°C aging treatments, only tertiary γ' precipitates (with sizes below 100nm) were observed. However, during the 930°C aging treatment, tertiary γ' transformed into secondary and primary γ' precipitates, with sizes ranging from 100nm to 400nm and exceeding 400nm, respectively.

Furthermore, the precipitates exhibited growth with longer aging times, consistent with the phenomenon known as Ostwald Ripening. This theory posits that, in solution, small particles dissolve into the matrix and subsequently re-precipitate onto larger particles to attain a stable state. The Ostwald Ripening process has been commonly employed to describe the coarsening behaviour of γ' precipitates in nickel alloy [2,3].

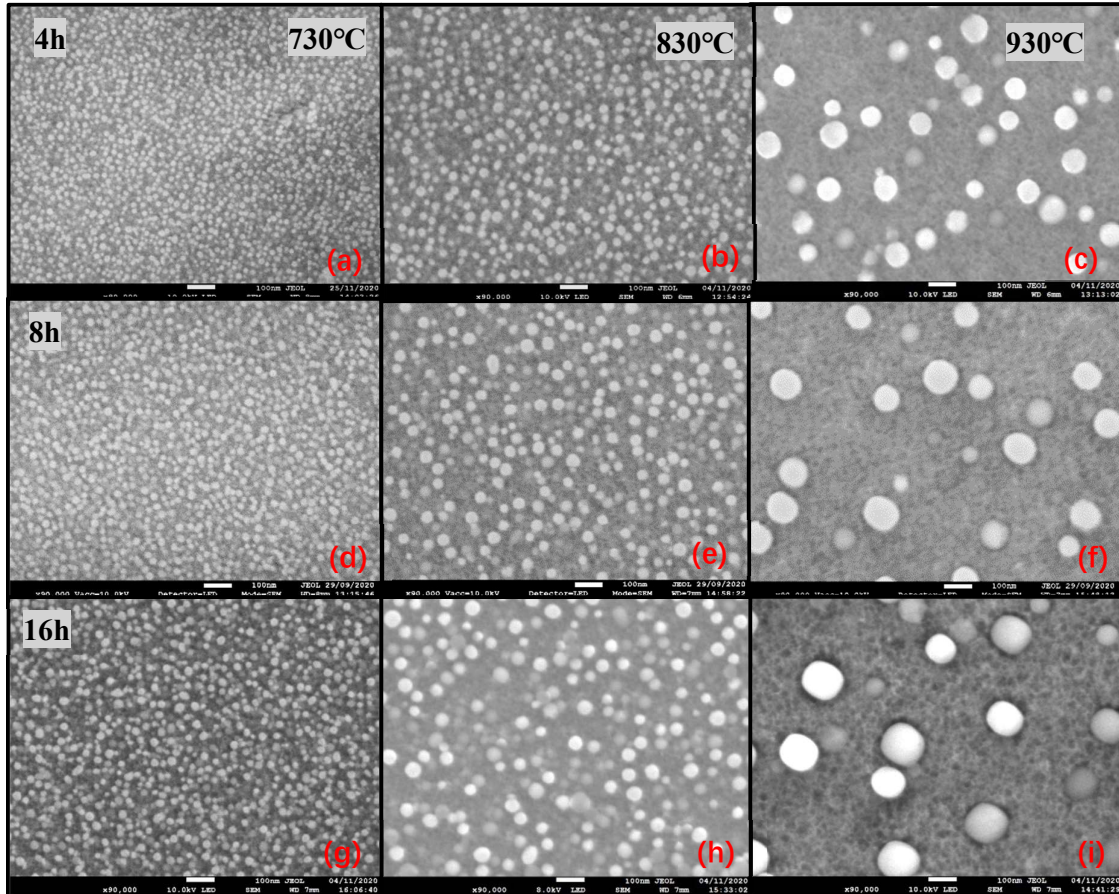


Figure 4.9 SEM images of γ' morphology and distribution of 9 heat treatments (a) 730°C/4h; (b) 830°C/4h; (c) 930°C/4h; (d) 730°C/8h; (e) 830°C/8h; (f) 930°C/8h; (g) 730°C/16h; (h) 830°C/16h; (i) 930°C/16h

Figure 4.11 presents a graph depicting the precipitate size distribution in terms of diameter versus aging time. In addition to the above results, it is evident that the size distribution becomes broader with increased aging time. For example, in the 830°C group, the difference between the maximum and minimum values increased from 20.59nm to 27.42nm as the aging time extended from 4 hours to 16 hours.

Table 4.6 Precipitate measurements summary of 9 designed heat treatments

Temperature(°C)	730			830			930		
Aging time(hr)	4	8	16	4	8	16	4	8	16
Mean(d/nm)	17.51	20.32	23.49	25.98	31.19	43.29	72.96	85.08	108.92
Min(d/nm)	10.68	15.43	15.80	16.19	17.36	27.59	44.07	50.80	63.08
Max(d/nm)	21.99	25.97	31.53	36.78	40.73	55.01	103.10	112.07	149.50

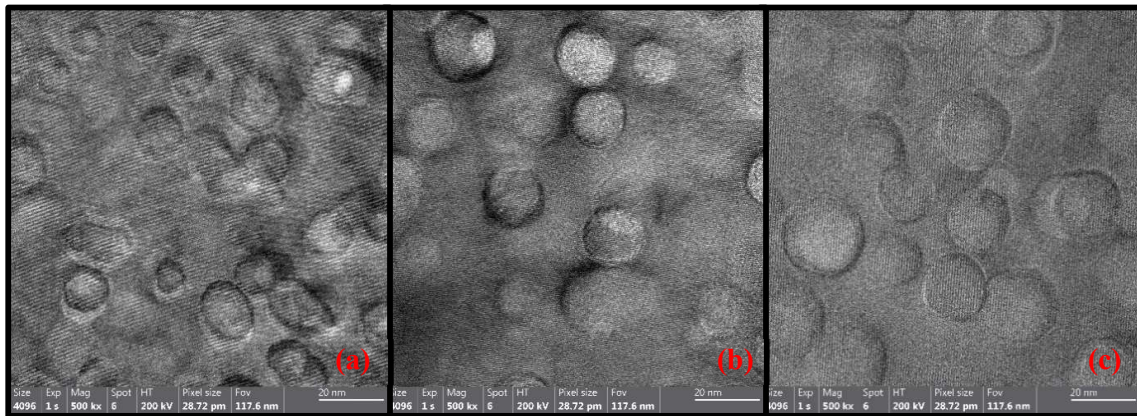


Figure 4.10 TEM characterization of γ' precipitates after 730°C aging process, (a) 4 hours; (b) 8 hours; (c) 16 hours

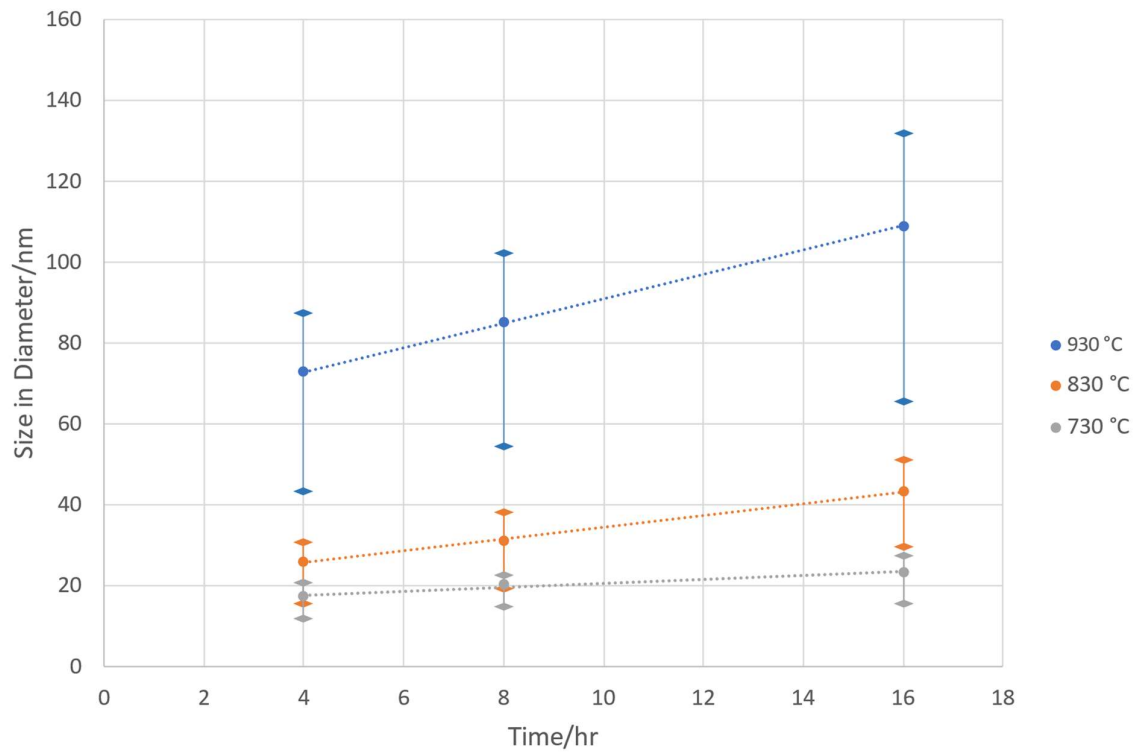


Figure 4.11 Precipitation size versus aging time at different temperatures, with error bars indicating size distribution.

4.3 Dynamic Hot Compression

4.3.1 Mechanical Response

The stress-strain curves at temperatures 730°C, 830°C and 930°C were given in Figure 4.12(a), (b) and (c) respectively. The general flow stress behaviour for compression testing is normally controlled by several metallurgical mechanisms such as work hardening, dynamic recovery and dynamic recrystallisation[4,5]. In the initial stage of the compression, the deformation is controlled by work hardening because of the increasing dislocation density, and the flow stress rises rapidly. With the development of deformation, dislocation accumulation (work hardening) and dislocation cancellation (DRV) occur simultaneously. In the meantime, DRX is triggered when dislocation density exceeds its critical point[6,7]. And DRV together with DRX contribute to the softening effect in stress-strain curve. The rise of flow stress thereby becomes slower. Then the curve reaches its peak which marks the critical point of dislocation density accumulation, known as critical stress (σ_c). At this point, the work hardening and softening effect reach their dynamic equilibrium state. With strain continuing to increase, flow stress goes down as the softening effect dominates the deformation. Eventually, work hardening and dynamic softening reach their equilibrium state again as the flow stress becomes stable with strain increasing[8-11].

When comparing flow stress curves with different temperatures, the current work compares 730°C and 930°C tests, the softening effect shows a different sensitivity to different temperatures. For 730°C, all 3 curves were dominated by work hardening effect which means the softening effect has not overtaken the work hardening effect. In terms of 930°C, all 3 tests gave intact flow stress curves, this indicates that dynamic softening occurred more easily at 930°C than at 730°C.

Moreover, the dynamic softening acted differently under different strain rates. See Figure 4.12, in areas marked blue, the flow stress is smaller at a lower strain rate (which is a fact commonly accepted), but it acted in the opposite way in areas marked red. In addition, the flow stress

reaches its critical point earlier on curves at a lower strain rate, where $0.0005s^{-1}$ and $0.005s^{-1}$ curve reaches its critical point at strain 0.34 and 0.40 respectively. $0.05s^{-1}$ curve had not reached its critical point at strain 0.5. This can be explained by the flow stress behaviour described in previous paragraph. DRV happened with work hardening while DRX happened when dislocation density reached its critical point. The work hardening mechanism dominates the early stage of deformation. Hence, slower deformation gives more time and allow sufficient dislocation to accumulate, this leads to a higher critical stress at a lower strain rate. And meanwhile, slower deformation allows dislocation density to reach its critical point (triggered DRX) at a lower strain level. Furthermore, the adiabatic heating effect can also play an important role. Extra internal heat will be generated when compressing, and the higher strain rate gives less time for heat to dissipate, and with higher temperature, the stress will be lower. Hence, the adiabatic heating effect also potentially contributes to the observation that higher strain rates lead to lower flow stress.

The work hardening rates ($\theta = d\sigma/d\epsilon$) of 930°C tests at different strain rates were calculated based on true stress and true strain. Then q was plotted against s in order to show the σ_c . The σ_c can be determined by intercepting the curve when $q=0$, in which the effect of work hardening reached the equilibrium state with dynamic softening. According to Figure 4.13, σ_c is 519.5MPa, 345.3MPa and 300.5MPa for strain rate $0.05s^{-1}$, $0.005s^{-1}$ and $0.0005s^{-1}$ respectively.

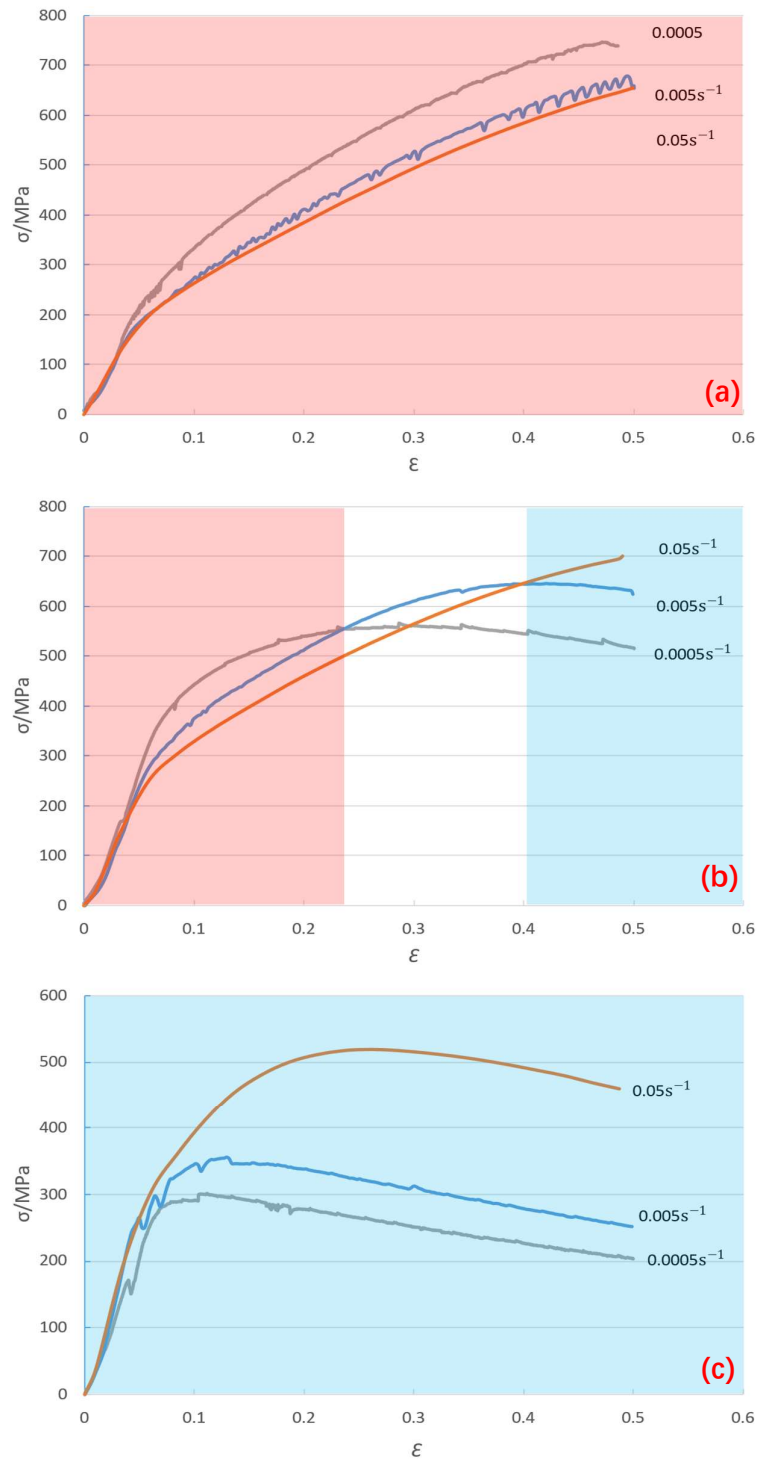


Figure 4.12 Engineering stress-strain curve of hot compression tests at (a) 730°C, (b) 830°C, (c) 930°C

The microstructural investigation on hot compression samples was mainly characterised by EBSD techniques and analysed by Channel 5 HKL software. 2mm x 2mm EBSD maps were acquired at centre area of each sample, and close-up mapping was also carried out to reveal details about DRX and local grain evolution. Besides, the shape and barreling effects of the deformed samples were captured by optical camera and shadowgraph. Figures 4.14 below is an image from the camera and Figure 4.19 is data obtained from shadowgraph. It can be seen that samples deformed at 930°C have obvious barreling effects and slight barreling effects can be seen from 830°C samples deformed at low strain rate. In addition, different levels of elastic springbacks were spotted on samples deformed under 730°C and 830°C at strain rates of $0.05s^{-1}$ and $0.005s^{-1}$. As can be seen from Figure 4.16 (a) and (b), tests for 730°C and 830°C at strain rate of $0.05s^{-1}$ and $0.005s^{-1}$ had higher peak stress, and the higher the peak stress, the more elastic deformation as a proportion of the total deformation, hence more elastic springback.

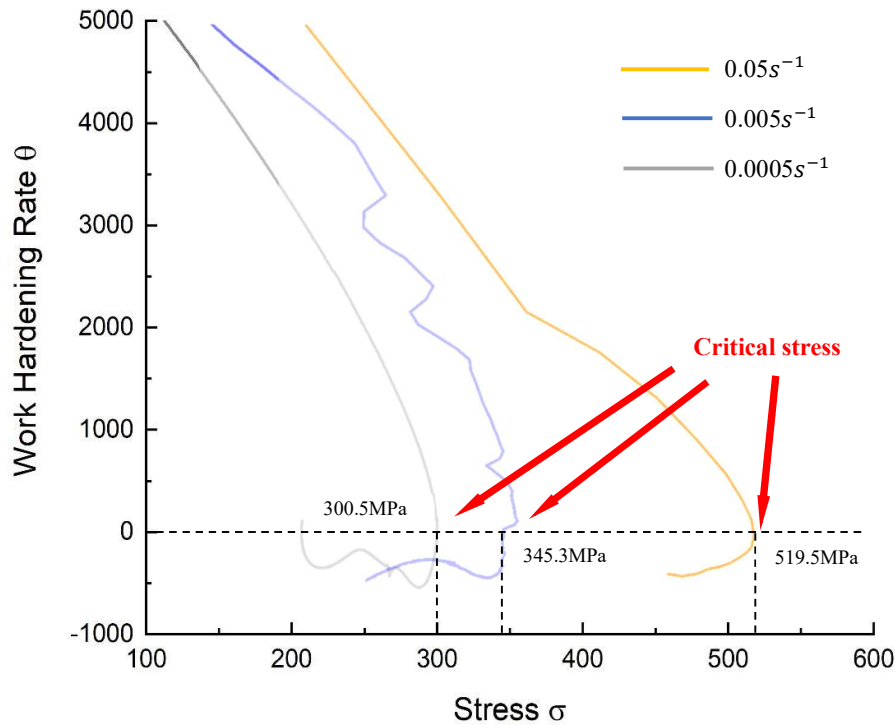


Figure 4.13 Work hardening rate against true stress at 930°C with different strain rate

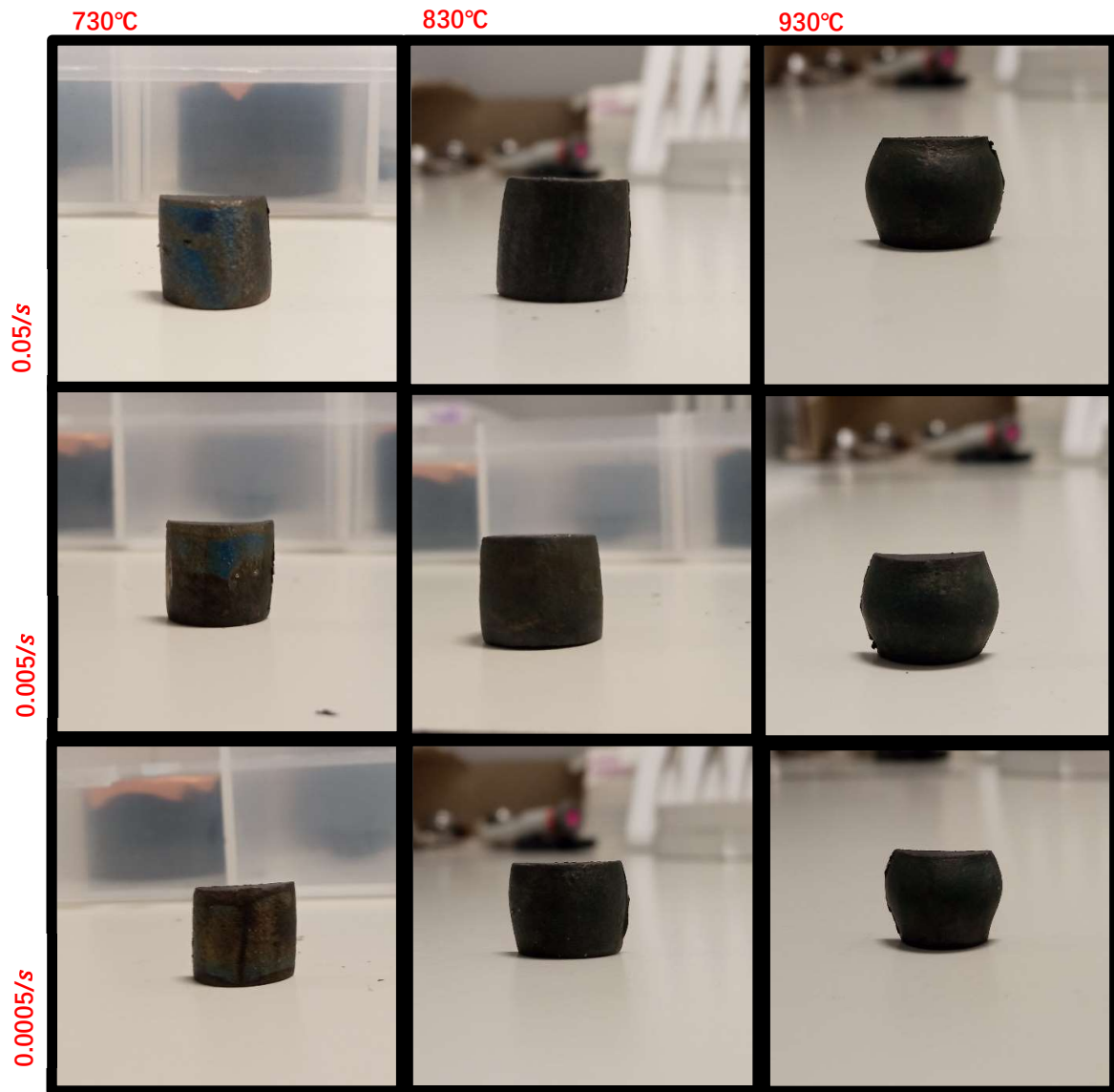


Figure 4.14 Optical images of deformed samples

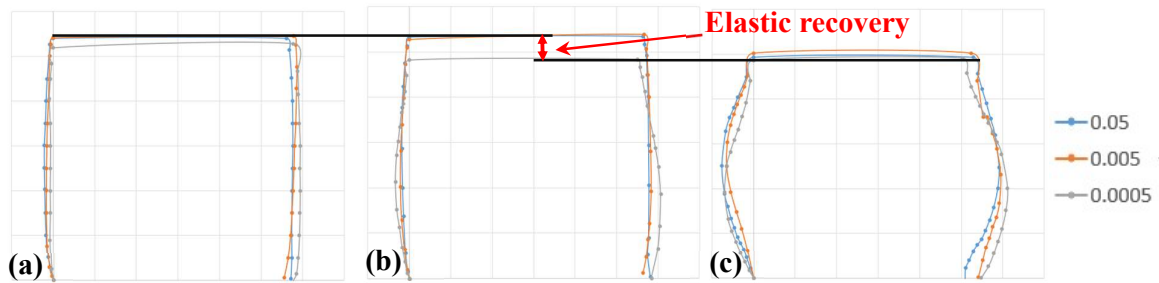


Figure 4.15 Shadowgraph data compares the shape of deformed samples with different strain rate at (a) 730°C; (b) 830°C; (c) 930°C.

4.3.2 Grain Characterisation Results

The 2mm x 2mm EBSD scans are shown in Figure 4.16. Scans were acquired at centre area of each sample since most strain concentrates in the centre of the samples. Figure 4.16 is a series of band contrast images of nine hot compression tests, where rows from top to bottom correspond to strain rate at $0.05s^{-1}$, $0.005s^{-1}$, $0.0005s^{-1}$, and column from left to right corresponds deformation temperature at $730^{\circ}C$, $830^{\circ}C$, $930^{\circ}C$ respectively. From Figure 4.16,

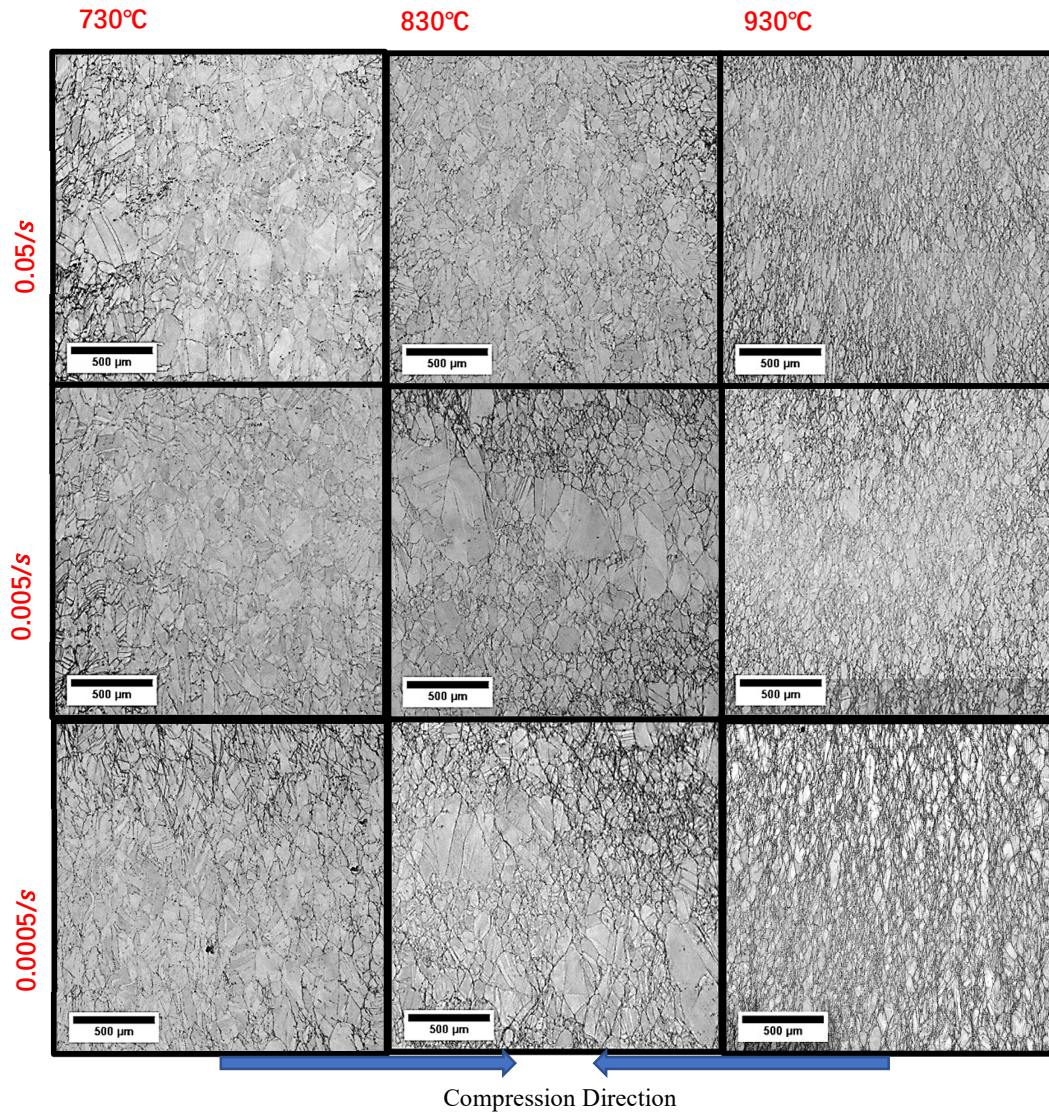


Figure 4.16 Band contrast images of microstructure at centre of hot compression samples, rows from top to bottom corresponds to strain rate at $0.05s^{-1}$, $0.005s^{-1}$, $0.0005s^{-1}$, and column from left to right corresponds deformation temperature at $730^{\circ}C$, $830^{\circ}C$, $930^{\circ}C$.

the grain morphology and evolution can be revealed preliminarily. A grain size calculation was carried out using interception method horizontally. The grain size was measured manually by ImageJ as the ASTM standard is not suitable for elongated grains. The results are listed in Table 4.7.

Contrary to grain growth, dynamic recrystallisation generates new small grains, therefore, leading to a decrease in grain size. It can be seen that under different strain rates, grain size decreased with the increase of deformation temperatures. For example, grain size decreased from 53.93 μm to 22.13 μm with temperature rose from 730°C to 930°C at a strain rate of 0.05/s. On the other hand, no evident relationship is found between grain size and strain rate.

A noticeable variation in the maximum grain size can be seen from the experimental results. Specifically, at a strain rate of 0.05 s^{-1} , the maximum grain size exhibits similar values for both the 730°C and 830°C tests. However, a significant increase is observed at a strain rate of 0.005 s^{-1} for the 830°C test, followed by a slight decrease at a strain rate of 0.0005 s^{-1} . Interestingly, during the 930°C tests, the values stabilize. This phenomenon suggests the occurrence of AGG during the 830°C test at a strain rate of 0.005 s^{-1} , which is subsequently suppressed by the development of dynamic recrystallization (DRX) mechanisms.

Table 4.7 Results of grain size calculated by interception method horizontally

Temperature Strain Rate	730°C	830°C	930°C
0.05/s	53.93 μm (max 299.58 μm)	50.07 μm (max 257.48 μm)	22.13 μm (max 109.14 μm)
0.005/s	59.99 μm (max 259.46 μm)	67.00 μm (max 392.74 μm)	27.17 μm (max 70.65 μm)
0.0005/s	56.23 μm (max 257.29 μm)	57.21 μm (max 328.81 μm)	25.17 μm (max 71.33 μm)

Chapter 5 Discussion

Following the results chapter, this chapter will look at the discussion of the results, including the interpretation of results, the comparison with prior research and the limitations. For the alignment with results chapter, this chapter will be separated into four parts, grain evolution, precipitation coarsening, dynamic hot compression and followed by a general comment.

5.1 Grain Size Evolution

As described in the literature review, nickel-based superalloys are well known for their excellent elevated temperature performance. As a newly developed nickel alloy, Haynes 282 is a precipitate-strengthened material for high temperature structural applications. It possesses a unique combination of creep strength, thermal stability, weldability, and fabricability not found in currently available commercial alloys.

As an essential microstructure feature to capture, grain size has significant effects on most mechanical properties. For example, hardness, yield strength, tensile strength, fracture resistance, fatigue, etc. These properties are all enhanced with smaller grains. Fine (smaller) grains will create more grain boundaries, and more grain boundaries mean more obstacles to dislocation movement, therefore, there will be higher stress required for plastic deformation. This is well known as Grain Boundary Strengthening (or Hall-Petch Strengthening)[1]. On the other hand, at elevated temperatures, small grains can be detrimental to creep property as grain boundaries act as sites for the nucleation of creep cavities and the formation of voids such as triple point cracks. Grain boundaries can also provide preferential diffusion paths to enable dislocation recovery mechanisms such as climb. The nickel alloys used for turbine blades are single crystals because of this[2,3]. Grain growth happens at elevated temperatures during aging or annealing. As mentioned in literature reviews, the driving force for grain growth is depending on the grain boundary energy as small grain stores higher energy than big grain. However, this common theory can be interrupted and divided into normal or continuous grain growth (CGG) and abnormal or discontinuous grain growth (AGG). AGG happens when a subset of grain possesses higher grain boundary energy or lower local particle density[4]. As a

precipitate-strengthened and carbide-riched material, Nickel alloy is observed to have AGG behaviours[5–8].

Both grain strengthening and grain growth can be achieved during thermo-mechanical procedures (TMP) and can be altered by post heat treatments. Various phenomena occur during hot processing, including recovery, dynamic recovery (DRV), recrystallization, discontinuous and continuous dynamic recrystallization (DDRX and CDRX), geometric dynamic recrystallization (GDRX) [6], as mentioned in literature reviews. Since Nickel alloys have a low stacking fault energy[9], so DDRX is the major phenomenon during recrystallization. And the serrations and bulging at grain boundaries are the main features for DDRX to occur, which will evolve into twins [6].

Figure 4.10 provides insights into the evolution of grain size concerning aging temperatures and durations. Notably, smaller grains were observed in all groups except for the one aged at 930°C. This can be explained by referring to the equilibrium phase diagram of Haynes 282 as illustrated in the literature review. Upon surpassing approximately 860°C, the dissolution of $M_{23}C_6$ starts to dissolve, and particularly, the dissolution of M_6C is completed at temperatures above 800°C. Consequently, during aging at 930°C, the grain can grow in a carbide-free phase. This observation underscores the significance of secondary phases in the occurrence of abnormal grain growth (AGG) in nickel-based alloys. This phenomenon is attributed not only to secondary particles serving as nucleation sites in recrystallization but also to their contribution to the Zener Pinning effect, which impedes normal grain growth [4, 6, 10].

Moreover, the heterogeneity of grains became apparent following heat treatments. Table 4.7 and Figure 4.11 provide a summary of the calculated grain size results obtained using the interception method. It can be observed that, following 4 hours of aging at 730°C, AGG predominantly influenced the recrystallization of small grains, a phenomenon also known as discontinuous recrystallization. With an extended aging time of 8 hours, AGG continued to

occur, resulting in a decrease in average grain size. Comparing the grain size after 8 hours and 16 hours of aging, it is noteworthy that the latter exhibited a larger grain size. This can be attributed to the attainment of a critical density of AGG grains, triggering continuous grain growth (CGG).

Regarding aging at 830°C, the grain size further increased due to the dominance of CGG with longer aging durations. This can be attributed to the higher temperature, which introduces more energy, accelerating the progress of recrystallization. Therefore, during the 4-hour aging period, AGG had already reached its critical level, leading to the subsequent dominance of CGG with further aging. As mentioned earlier, the samples aged at 930°C exhibited a microstructure with limited carbides, resulting in CGG predominantly driving grain growth and thus exhibiting a relatively homogeneous microstructure. These findings align with the results presented by V. Randle et al. [11].

5.2 Precipitation Coarsening Mechanism

Apart from grain size and carbide distribution, the excellent high temperature properties of Haynes 282 are strongly influenced by the presence of γ' precipitates. As reported in Chapter 2.1, γ' is a strengthening phase in nickel-based alloys as a result of the nature of its crystal lattice. In the lattice of γ' , atoms of strengthening elements such as Al and Ti replace the lattice position of Ni forming an intermetallic phase, therefore creating lattice distortion and strengthening effects[12,13]. Moreover, it's worth noting that the crystal structure of the γ' phase is arranged in an ordered manner, unlike the disordered structure of the γ phase. As explained in Chapter 2.1.3, this dissimilarity in crystal order prevents dislocations from penetrating through the γ' phase while passing through the γ matrix. As a result, a stable microstructure is created, which plays a vital part in preserving the high-temperature properties of nickel-based superalloys[12–14]. The morphology, size and fraction of γ' precipitates, are

the main features to characterize when analysing γ' . It can be influenced by, first, the alloying elements. The higher percentage of γ' strengthening elements such as Al, Ti and Ta, the higher fraction of γ' and different alloying elements will result in different lattice misfits, which consequently results in different γ' morphology. And it was found that the smaller the lattice misfit, the larger the γ' particle needs to grow to form cuboidal morphology[12,15]. Secondly, the materials forming process (for example casting, forging, welding or powder sintering) will also affect the microstructure. Lastly, the morphology of γ' can also be altered by post heat treatment. The γ' precipitates can be dissolved during solution treatment, which normally occurs between 1121°C-1149°C. Subsequently, γ' starts to precipitate out from the matrix below 1000°C and become stabilized through the aging process[16,17]. However, γ' precipitates can be coarsened with further aging, where small precipitate particles dissolve again and precipitate out into large particles. This phenomenon is explained and known as the Ostwald Ripening mechanism[18,19]. Consequently, this process needs to be carefully controlled to get an optimized γ' morphology, size and fraction.

LSW theory, initially proposed by Lifshitz and Slyozov[18] and further developed by Wagner[20], has emerged as a valuable tool for examining the coarsening kinetics of γ' precipitates [17]. The classic LSW theory is based on several assumptions: (a) the particles exist in a spherical form within the liquid system; (b) the inter-particle spacing is sufficiently large to prevent any significant inter-particle reactions; (c) the volume fraction of precipitates is low, ideally close to zero [18]. Although achieving a precisely zero volume fraction in alloys is impractical, previous investigations have demonstrated the applicability of the classic LSW theory to the majority of nickel-based alloys [17,19].

Furthermore, researchers have conducted validations and introduced modifications to the LSW theory. Ardell [21] proposed a modified LSW theory (MLSW), which stated that as the volume fraction of precipitates increases, the particle growth rate also increases, accompanied by a

broader distribution of particle sizes. Another modified approach, the Lifshitz-Slyozov encounter modified (LSEM) model, was proposed by Davies et al.[22]. This model suggests a slight increase in the particle growth rate and a broader particle size distribution. These phenomena can be observed in Figure 4.15, where the broader size distribution corresponds to an increased growth rate.

These advancements and modifications in LSW theory offer valuable insights into the complex coarsening behaviour of precipitates, capturing the dynamic relationship between growth rate, volume fraction, and particle size distribution. Furthermore, this theory provides a foundation for conducting additional numerical analyses to deepen the understanding of the coarsening kinetics.

Numerical Modelling of γ' Precipitates Evolution

The matrix-diffusion controlled precipitation mechanism can be characterized by either classical or modified LSW theories, both of which suggest that the coarsening of precipitates can be explained using a power law:

$$(R_t^n - R_0^n) \propto t \quad (1)$$

where R_t is the average particle radius at time t , R_0 is the average particle radius at $t=0$, n is a temporal exponent and its value is decided by a different precipitation mechanism. According to Wu et al.[23], the precipitation mechanism in nickel-based superalloys is dominated by the matrix-diffusion controlled process. Therefore, in this study, $n=3$. The expression of classic LSW theory is shown below:

$$R_t^3 - R_0^3 = Kt \quad (2)$$

K is the coarsening rate constant which can be defined in Arrhenius equation:

$$K = A \exp \left(-\frac{E_a}{RT} \right) \quad (3)$$

Where A is a constant, E_a is the activation energy of precipitation growth, R is the gas constant and T is the aging temperature. This equation can also be written as:

$$\ln K = -\frac{E_a}{RT} + \ln A \quad (4)$$

When the natural logarithm of time(t) $\ln(t)$ is plotted against the natural logarithm of the average radius of precipitates $\ln(r)$, a clear linear relationship can be seen in Figure 5.1. Furthermore, an average slope of $0.29 \approx 1/3.4$ can be calculated which means this alloy is mainly controlled by the cube rate law of LSW theory and correlates well with Oswald ripening [22,23].

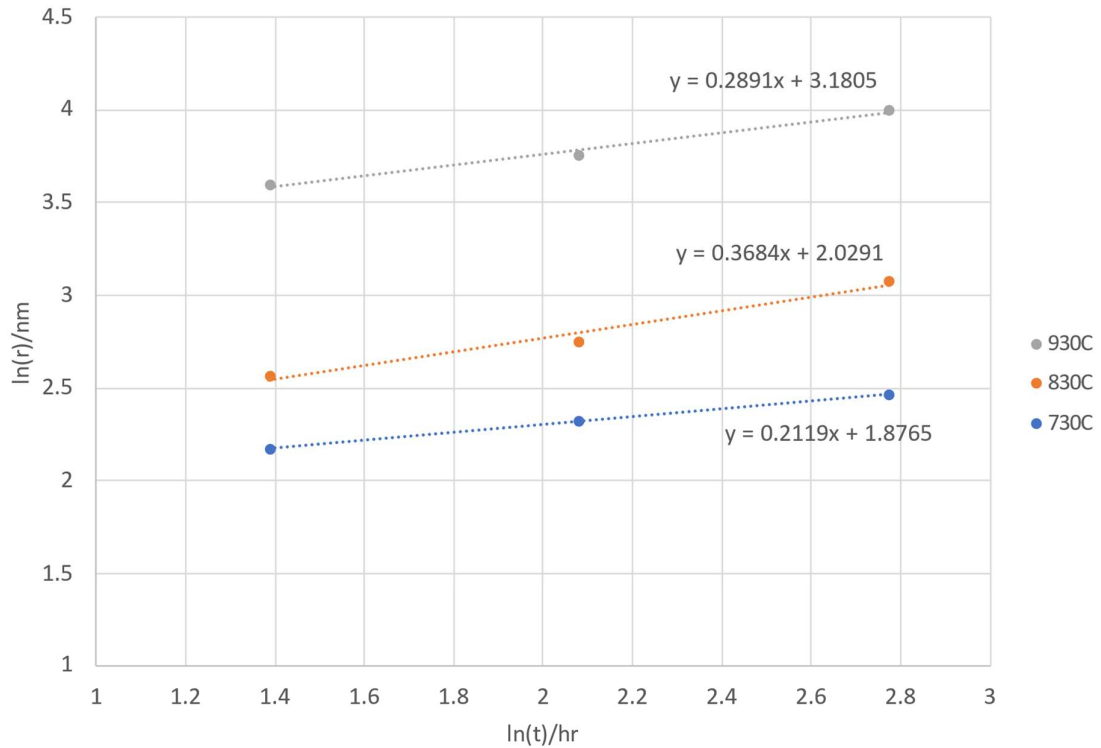


Figure 5.1 The effects of aging time on γ' precipitates size at different temperatures in logarithm

Hence, the activation energy of γ' precipitates growth can be calculated using the Arrhenius equation and by plotting $\ln(K)$ versus $1/T$, see Figure 5.2. The activation energy $E_a=238\text{KJ/mol}$ was obtained. Table 5.1 listed a few nickel alloys that have a similar chemical composition to Haynes 282, which shows that the calculated coarsening activation energy for Haynes 282 corresponds well with 247KJ/mol reported by Shuangqun et al. and 255 KJ/mol reported by Hou et al. [24,25].

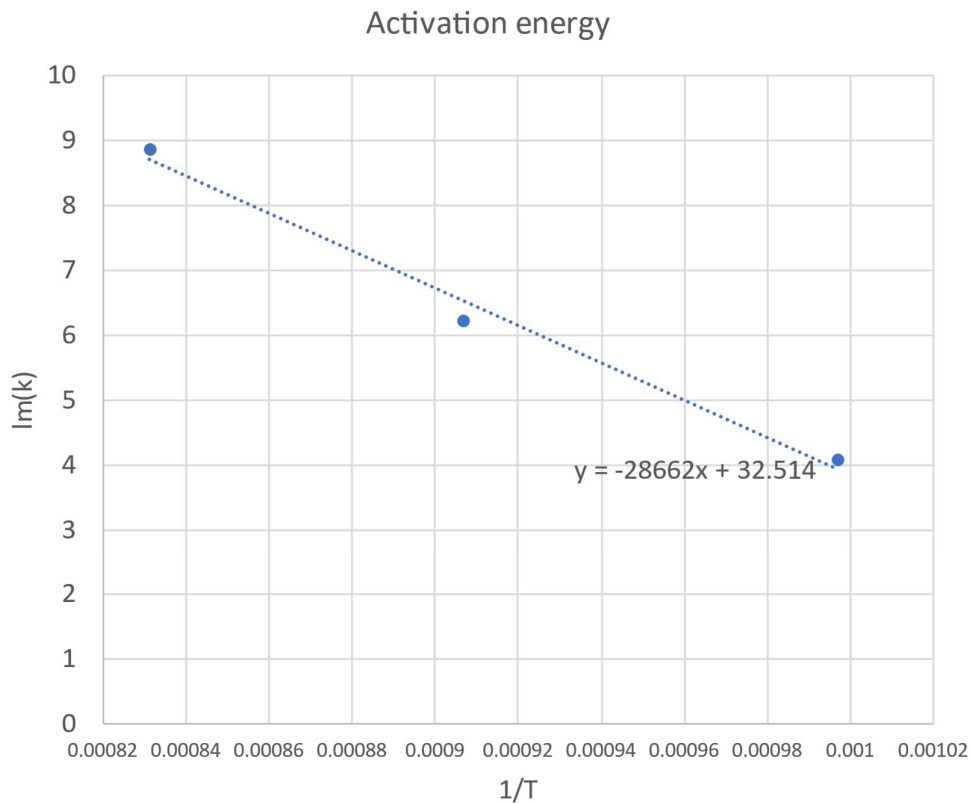


Figure 5.2 Arrhenius equation by plotting $\ln(K)$ versus $1/T$ illustrating precipitation growth in Haynes 282 alloy

Table 5.1 Activation energy for coarsening of γ' precipitates in similar nickel base alloys [24]

Element	Ni	Cr	Co	Mo	Ti	Al	Fe	Mn	Si	C	B	Activation energy for coarsening
Haynes 282	57	20	10	8.5	2.1	1.5	1.5 max.	0.3 max.	0.15 max	0.06	0.005 max.	238.3KJ/mol
Alloy 1	49	24.3	19.6	0.5	1.6	0.8	1	0.3	0.5	0.03	/	247KJ/mol
Alloy 2	57	15.5	10.8	2.1	4.6	3.2	/	/	/	0.07	0.08	255KJ/mol

5.3 Dynamic Recrystallisation

As mentioned in the literature reviews and previous chapters, various phenomena happen during TMP including recovery, dynamic recovery (DRV), recrystallization, discontinuous and continuous recrystallization (DDRX and CDRX), geometric dynamic recrystallization (GDRX) and post dynamic recrystallisation (PDRX)[26–29]. These phenomena will shape the microstructure and determine the properties of materials. Meanwhile, many factors will affect the occurrence of these phenomena, for example, the alloying elements, the initial condition of the sample, deformation temperature, dwell time, cooling methods and applied strain and strain rate[30,31]. In addition, stacking fault energy (γ_{SF} , SFE) is an essential value to consider when investigating these phenomena. Table 5.2 illustrates that nickel is widely acknowledged to possess a middle stacking fault energy. According to Emil Eriksson et. al[27], nickel-based superalloys have a relatively low stacking fault energy, resulting in deformation induced recrystallization (DDRX) being the dominant mode of recrystallization[32].

Table 5.2 SFE of metals and alloys at room temperature[32]

Materials	SFE (mJm^{-2})
Aluminium	166
Copper	78
Silver	22
Gold	45
Nickel	128
Cobalt (FCC)	15
Zinc	140
Magnesium	125
Zirconium	240

Studies had been done on Haynes 282 alloys regarding its DRX during hot compression by Eriksson et al [6,27]. They investigated the effects of carbides on DRX during hot deformation. Although the investigation cannot prove the effectiveness of carbides, they captured different recrystallisation degrees at different temperatures and strain rates both graphically and numerically. Besides, they observed both DDRX and CDRX after hot deformation and a 90s post-deformation hold was added to study the PDRX. However, most hot compression tests on Nickel alloys were conducted at temperatures between 1000°C-1200°C[33–35]. Few investigations were achieved under lower temperatures. Furthermore, the complete hot compression behaviour involves multiple stages, with several mechanisms occurring within each stage. Specifically, work hardening and softening mechanisms occupy the general hot deformation process, where the work hardening dominates in the early stage (before critical stress σ_c) and the softening dominates the later stage. And as described in the literature, softening mechanism is attributed to DRV and DRX[36,37]. Unlike previous studies, this research designed a series of hot compression tests at reduced temperatures, expected to reveal the microstructure evolution at the initial stage of hot deformation.

5.3.1 EBSD Analysis

Figure 5.3 presents the inverse pole figure (IPF) maps, offering additional support for the analysis of grain characteristics. The IPF maps provide valuable insights into grain orientation. Specifically, a magnified IPF image was captured for the 930°C test at a strain rate of 0.005 s^{-1} , as shown in Figure 5.4 (a). This magnified image provides a detailed view of distinct regions undergoing DRX as a result of hot deformation. These regions exhibit characteristic features such as necklace nucleation occurring at the grain boundary and the presence of elongated grains. Figure 5.4 (b) represents the grain orientation spread (GOS) map, which depicts the angle difference between individual grains and the average grain orientation. The colour gradient, ranging from blue to red, represents varying angles from low ($< 2^\circ$) to high ($> 8^\circ$), corresponding to recrystallized grains, sub-grains, and deformed grains, respectively. This visual representation provides further evidence of nucleation and DRX occurring at the grain boundary.

In Figure 5.5, the GOS maps for all the hot deformation tests are displayed, providing a comprehensive view of the grain evolution in terms of orientation throughout the tests. It is evident that the level of recrystallization increases with higher temperatures but lower strain rates. It is important to note that due to the resolution limitations of the maps, numerous small grains, especially in the 930°C tests, could not be clearly defined.

Additionally, it is worth mentioning that the interpretation of blue colour in Figure 5.5 does not exclusively indicate recrystallized grains due to the colour bar scale used. Therefore, further generated HUE histograms, Figure 5.6, were given here to support the illustration of grain evolutions. The histogram was formed using ImageJ and is corresponding to Figure 5.5. They were separated by yellow and dark dot lines into recrystallised grains (left side of yellow dot line), sub-grains (between blue and yellow dot line) and deformed grains (right side of blue dot

line) respectively. A continuous progression of DRX was observed throughout the prescribed temperature range, providing clear evidence of its evolution.

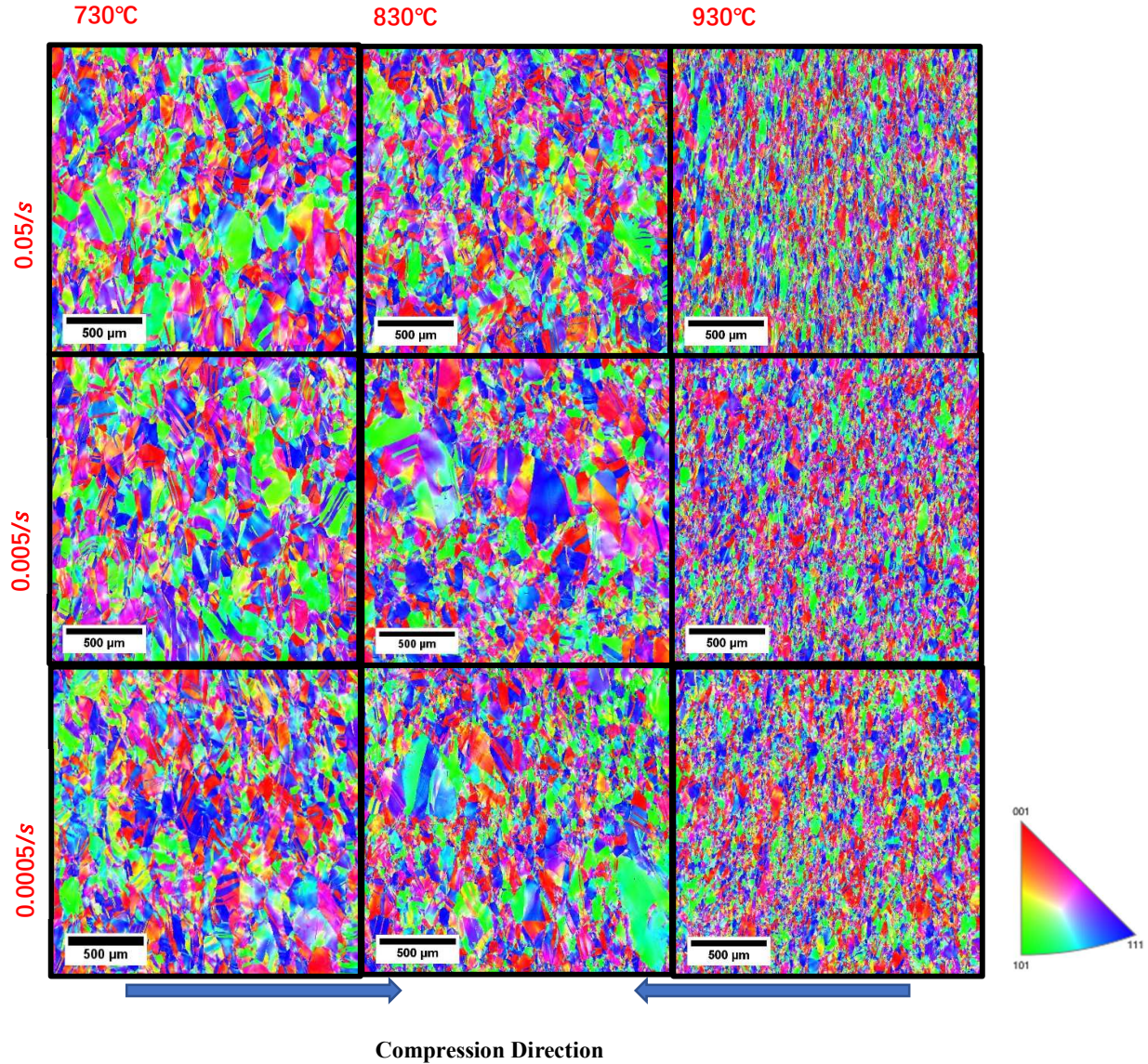


Figure 5.3 IPF maps of microstructure at centre of hot compression samples, rows from top to bottom corresponds to strain rate at $0.05s^{-1}$, $0.005s^{-1}$, $0.0005s^{-1}$, and column from left to right corresponds deformation temperature at 730°C, 830°C, 930°C.

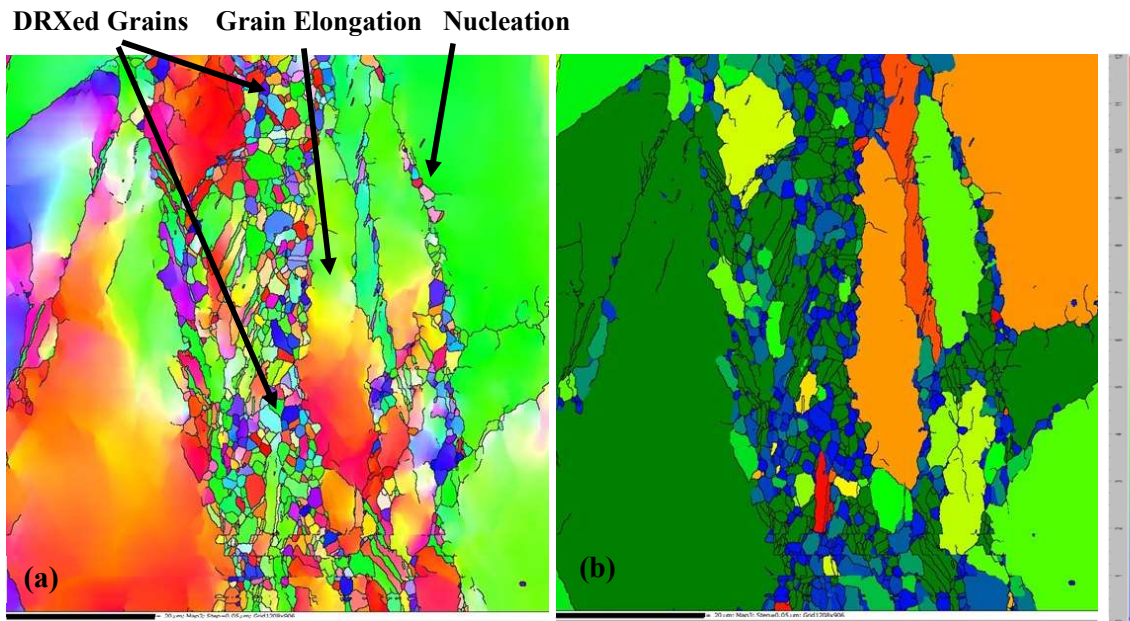


Figure 5.4 Close-up images from 930°C tests at 0.05s^{-1} strain rate, (a) IPF map; (b) Grain

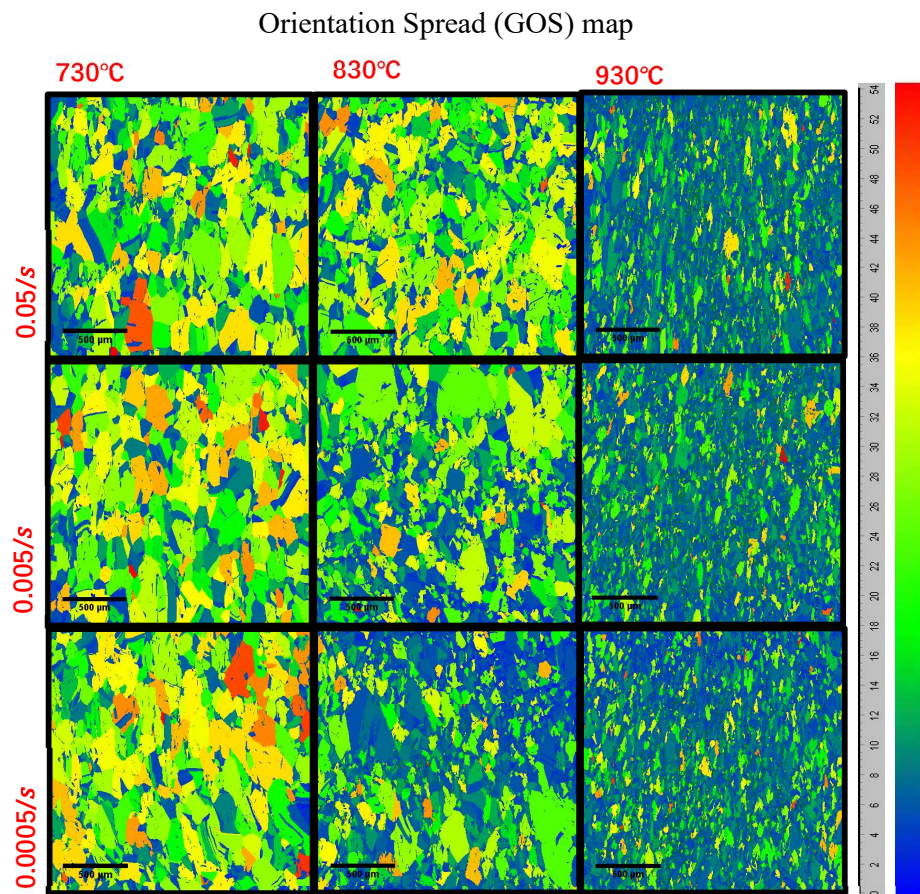


Figure 5.5 GOS maps showing the difference in grain orientation under different deformation temperature and strain rate

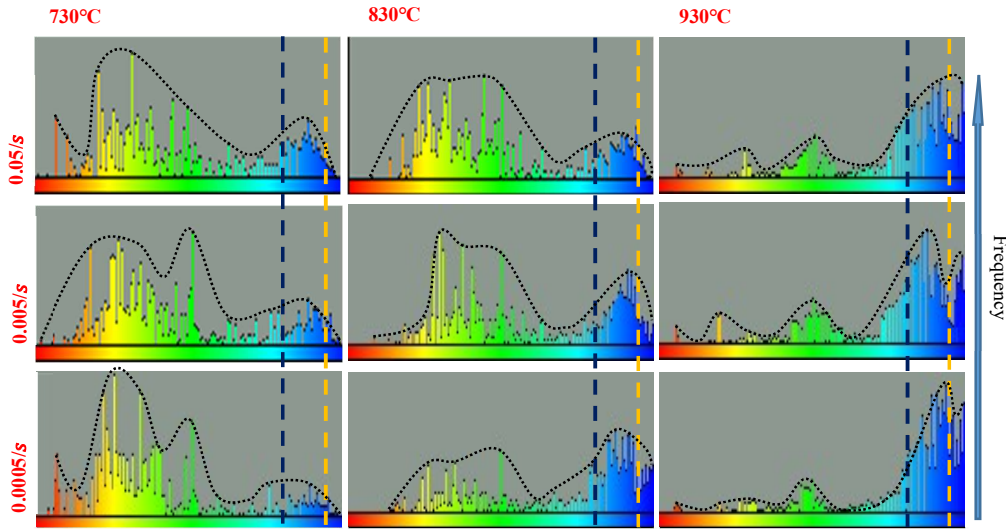


Figure 5.6 Hue histograms for GOS maps with yellow dot line separates recrystallised grain and sub-grains and dark dot line separates sub-grains with deformed grains

5.3.2 GND Analysis

A detailed investigation was conducted using higher magnification EBSD to elucidate the microstructural evolution. Figure 5.7 shows the IPF and GND (geometrically necessary dislocation) maps for various deformation conditions at strain rates of 0.05 s^{-1} and deformation temperatures of 730°C , 830°C , and 930°C . In Figure 5.7(a), no signs of nucleation were observed, indicating a microstructure devoid of DRX. However, at higher temperatures, the emergence of sub-grains (Figure 5.7(c)) signifies the occurrence of deformation and the initiation of DRX. With further development, the presence of necklace nucleation at the grain boundaries, indicative of DDRX, becomes evident. Geometrically necessary dislocations (GNDs) have been extensively studied and are commonly understood to represent additional dislocation storage necessary to accommodate lattice curvature in response to non-uniform plastic deformation [38,39]. Thus, the presence of GNDs is inevitable during plastic deformation. As illustrated in Figure 6.10(b), (d), and (e), GNDs (green colour) predominantly occupy the grain boundaries. During hot deformation, the increase in GND density is attributed

to work hardening, and their distribution may expand due to the initial DRX and subsequent grain evolution[23]. The corresponding GND density histograms generated by HKL Channel-5 are presented in Figure 5.8. It can be seen that GNDs (green colour) increase with higher deformation temperatures.

Furthermore, a comparison between different strain rates at 830°C is provided, see Figure 5.9 and Figure 5.10. Following deformation at a strain rate of 0.05 s^{-1} , further microstructural evolution was captured at a lower strain rate of 0.005 s^{-1} , as shown in the magnified image. In this case, a limited amount of nucleation occurred, accompanied by boundary serrations indicating the onset of subsequent nucleation. Ultimately, a similar microstructure featuring the necklace mechanism was observed at the lowest strain rate. However, when comparing the GND maps in Figure 5.7 to Figure 5.10, it becomes apparent that GND density is more sensitive to strain rate than temperature. This behaviour can be attributed to the nature of GNDs accumulation, as they tend to accumulate over time, hence, a lower strain rate gives higher GNDs. On the other hand, despite the fact that higher temperatures can accelerate dislocation movement, higher temperatures would weaken the effectiveness of work hardening, therefore would weaken GND accumulation. Hence, the results indicate that the promoting effect of temperature is not as significant as that of strain rate.

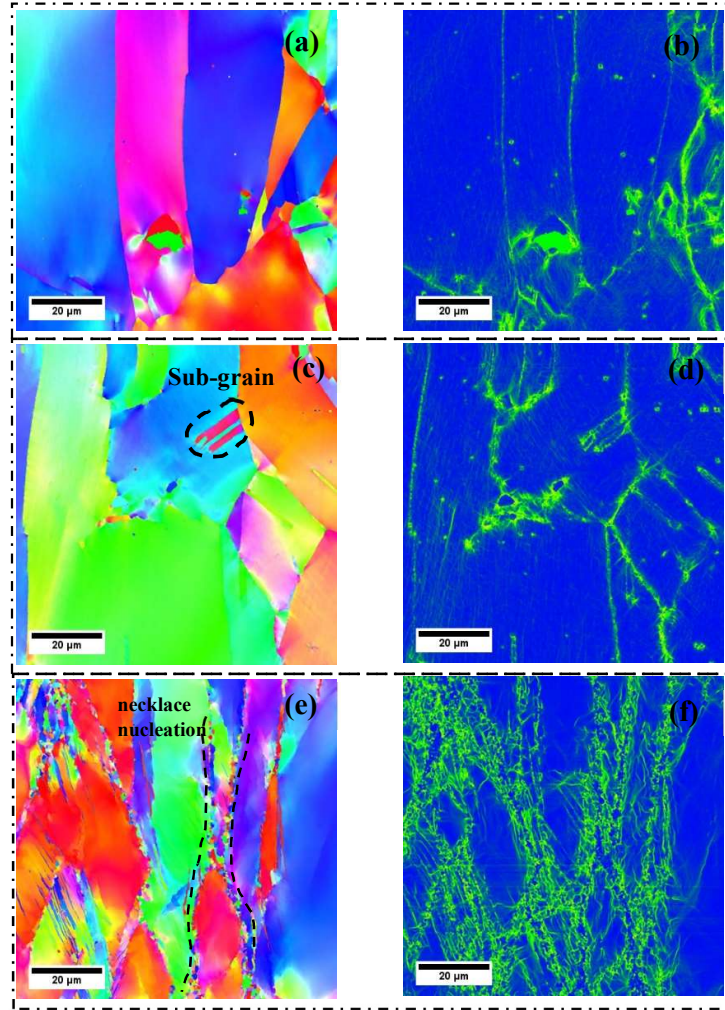


Figure 5.7 IPF and GND maps for strain rate of $0.05s^{-1}$ and deformation temperature at (a) (b) 730°C, (c) (d) 830°C and (e) (f) 930°C respectively

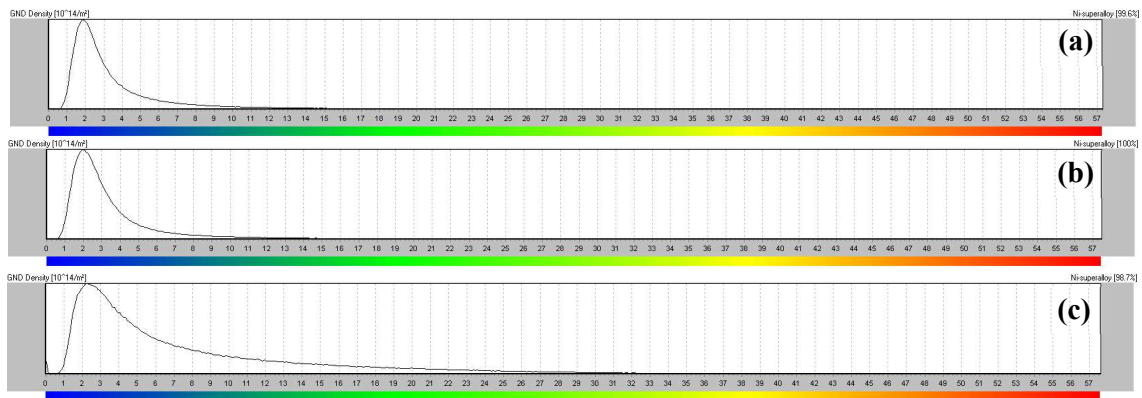


Figure 5.8 The distribution of GND density at strain rate of $0.05s^{-1}$, (a) 730°C; (b) 830°C; (c) 930°C

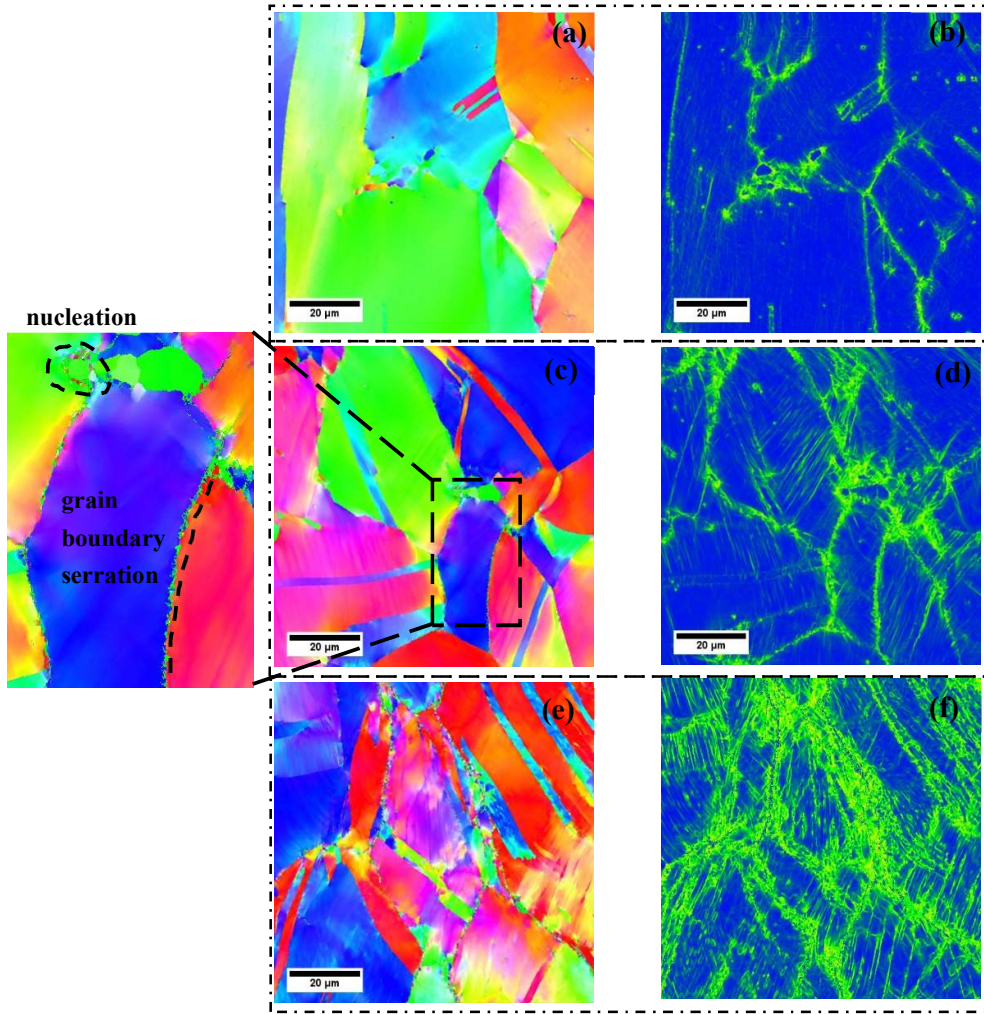


Figure 5.9 IPF and GND maps for deformation temperature of 830°C and strain rate at (a) (b) $0.05s^{-1}$, (C) (d) $0.005s^{-1}$ and (e) (f) $0.0005s^{-1}$ respectively

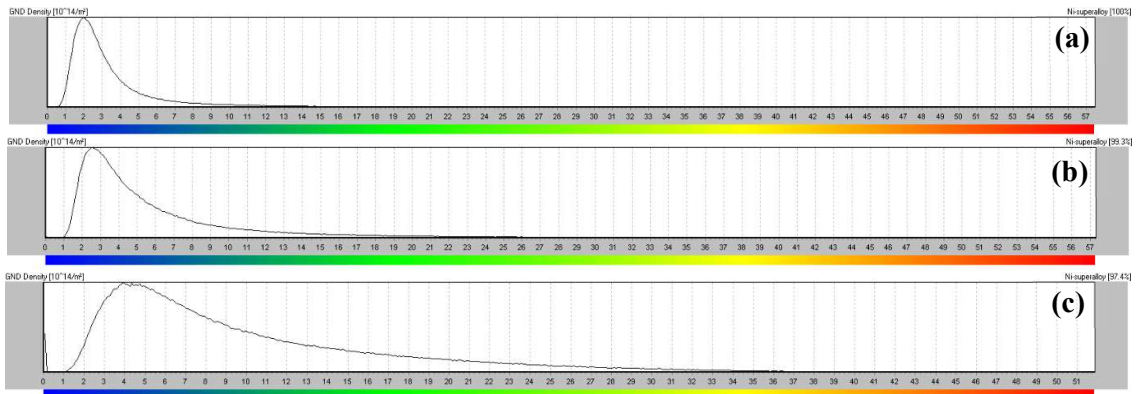


Figure 5.10 The distribution of GND density at deformation temperature of 830°C and strain rate at (a) $0.05s^{-1}$, (b) $0.005s^{-1}$ and (c) $0.0005s^{-1}$ respectively

5.4 General Comments

Haynes 282 is conventionally produced by forging or casting[15,40], and recently, additively manufactured Haynes 282 was also developed and adopted in several researches[41–45]. However, post heat treatments are always necessary in order to obtain optimised microstructure no matter which production process is applied. The objective of this research is to examine the impact of thermo-mechanical processing on this alloy. The doctoral thesis focuses on investigating the refinement and evolution of the microstructure following static post-heat treatments, as outlined in Chapters 4.1, 5.1 and 4.2, 5.2. Additionally, Chapters 4.3, 5.3 provide insight into the recrystallisation mechanism and stress-strain behaviour of Haynes 282 during thermo-mechanical processing.

The static heat treatments include the industry applied conventional standard treatment (1121°C/30mins/WQ+1010°C/2h/AC+788°C/8h/AC)[15], and a series of designed heat treatments (1121°C/30mins/WQ+730°C, 830°C, 930°C/4h,8h,16h/AC). Previous studies have been dedicated to investigating the impact of heat treatments on the microstructure of Haynes 282[17,46,47]. Ceena Joseph et al.[46] compared the standard treatment with heat treatments without solution treatment or with a lower aging temperature. However, the as-received Haynes 282 was in a rolled and solution treated condition. Therefore, the comparison between treatments with and without solution treatment may provide limited results. But the study recorded and proved that carbides were formed during second stage aging (788°C/8h/AC) in standard treatment. Therefore, in this study, the solution treatment was retained to eliminate any residual stress and inhomogeneous structure in as-received condition[46]. The design of 1-step aging was inspired by Kyeong-Yong Shin et al.[47]. In Shin's research, a solution treatment + 1-step aging (800°C/4h/AC) strategy was planned to be more economical. The outcomes showed that 1-step aging successfully produced about 20% γ' precipitates and provided good mechanical properties[47]. In addition, few studies have characterised or recorded the microstructure evolution of Haynes 282 aging treatment under different times and

temperatures. Hence, a series of designed 1-step aging was conducted and results and analysis were given in Chapters 4 and 5.

The grain evolution and growth mechanism were discussed in Chapter 5.1. The grain size was measured by different methods, including the Jeffries Planimetrics method, comparison method and interception method. These 3 methods are relatively traditional ways applied to determine grain size, and they were commonly used on nickel-based superalloys and other metals[48], [49]. However, the conventional method of grain size analysis for Haynes 282 does not provide specific results. Therefore, 3 traditional methods were applied to standard treatment samples to compare their reliability and efficiency. In this study, it is found that Jeffries Planimetrics method and Interception method provided more accurate results than the comparison method as the comparison method only had a 1 decimal places accuracy while Jeffries Planimetrics method and Interception method had 2 decimal places accuracy. Besides, a considerable number of tiny grains formed in Haynes 282, which cannot be reflected on the comparison charts. With regards to efficiency, the comparison method was the most straightforward way and Jeffries Planimetrics method was the most complex. Hence, considering the reliability and efficiency of the 3 methods, the Interception method was selected for further analysis. The characterisation and diagram results were given in Figures 4.10 and 4.11. Apart from grain size analysis, the grain growth mechanism of Haynes 282 was also revealed. A number of grain growth analyses of nickel-based superalloys have been posted and found that most nickel-based superalloys have abnormal grain growth (AGG)[5-7]. However, the grain growth behaviour of Haynes 282 has not been discussed yet. In this study, according to the results summarised in Chapter 5.1, the grain growth mechanism of Haynes 282 was revealed. According to Figure 4.10, 4.11 and Table 4.7, in 730°C aging treatments, a predominant influence of AGG on small grain recrystallization can be observed. Extending the aging time to 8 hours promoted AGG, leading to a reduction in average grain size. During 16 hours of aging, the latter exhibited larger grains attributed to the critical density of small grains, and this repressed the AGG and triggered

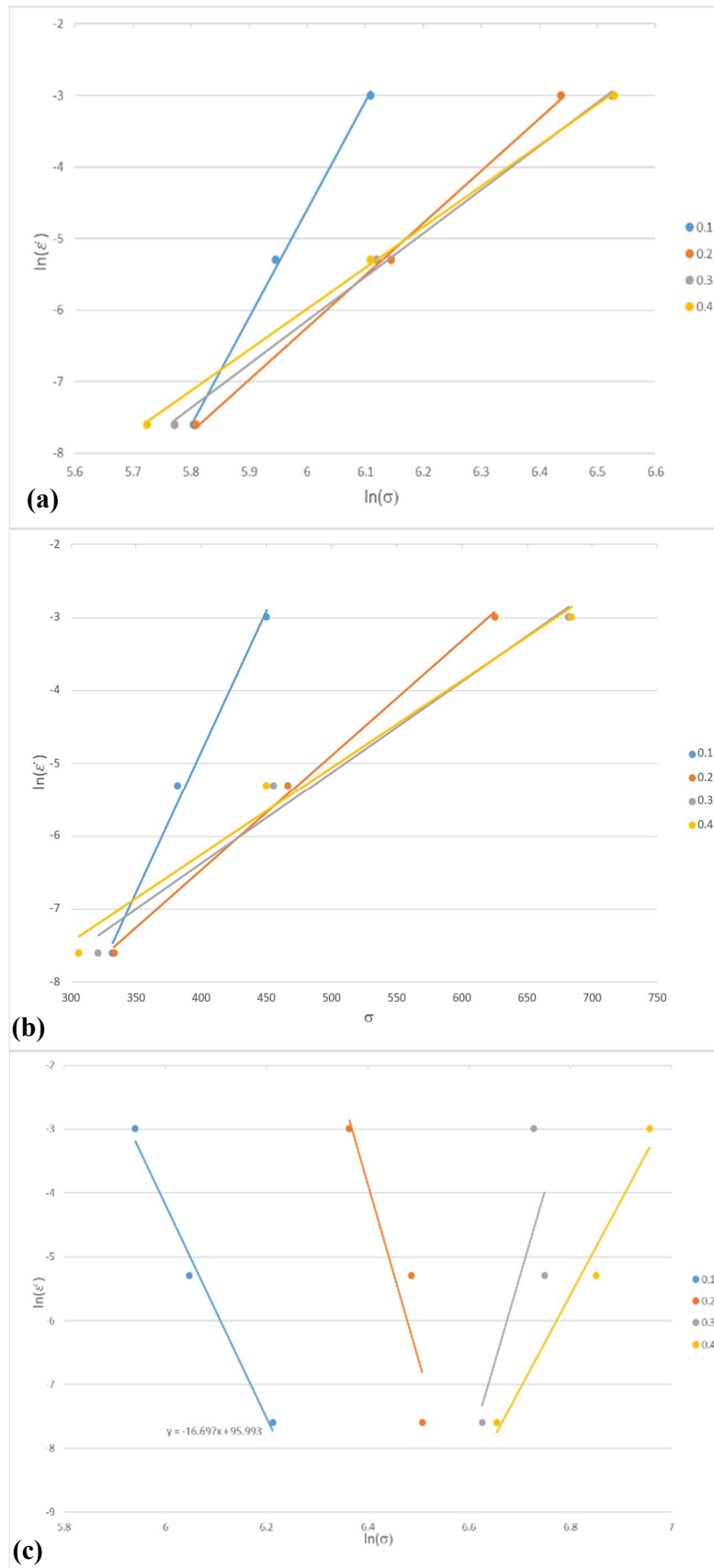
CGG. AGG dominated shorter aging treatments (4h and 8h) while CGG dominated 16h aging treatment. After 830°C aging treatments, grain growth followed the CGG mechanism as the number of small grains decreased and grain size increased with longer aging time. Finally, the grain growth became slower in 930°C tests although a slight decrease was seen after 8h aging. These results correspond well with the findings presented by V. Randle et al.[11]. They found that CGG happens at a temperature of approximately $0.65T_m$ (melting temperature), 845°C for Haynes 282. And growth became slower at higher temperatures and finally stagnated after $0.75T_m$, 975°C for Haynes 282. They also stated that AGG may occur transiently at some temperatures with shorter aging times. And CGG will replace AGG when small grains become impinged[11]. The results in this study verify this conjecture which AGG occurs at lower temperatures and is repressed with the development of CGG.

Following the investigation of grain size evolution, the γ' precipitates coarsening analysis was carried out based on the static heat treatments and recorded. As a major feature, γ' precipitation of nickel-based superalloys has been investigated for decades[50–55]. M. Fahrman et al.[52] compared two different simulation tools (TC-PRISMA and PanPrecipitation2014) for precipitation coarsening under two different thermal procedures. They validated the capabilities of those tools and obtained a γ/γ' interfacial energy of 20 mJ/m^2 . Jeffrey A. Hawk et al.[54] presented newly designed Haynes 282 B and C with different Ti/Al ratios. They carried out long term aging treatments which aged up to 9835h and phase field modelling was applied to predict γ' development and compared with the experimental results. Besides, the γ' coarsening mechanism was discussed and concluded that two newly designed alloys followed the trans-interface diffusion-controlled (TIDC) mechanism. Kevin Vattappara et al.[55] applied a novel physical simulation method, arc heat treatment, on Haynes 282. They obtained a unique graded morphology of γ' precipitation, which is similar to the results presented in this study. However, rather than using the numerical modelling method, they correlated the experimental results with TC Prisma software simulated results. Although there

have been numerous studies on the coarsening behaviour of γ' precipitation in Haynes 282, this research still has its contribution to this field. In Chapter 4.2, by implementing the planned static heat treatments, a sequence of graded microstructures demonstrating the γ' evolution was documented, as illustrated in Figures 4.13 and 4.14. Precipitation size was carefully measured and summarised into diagrams, see Figure 4.15. The precipitation coarsening mechanism was discussed, and numerical simulation was applied according to the summarised results. LSW theory and the Arrhenius equation were used for numerical modelling and an activation energy of 238KJ/mol was obtained. Table 5.3 listed values of the activation energy of other nickel alloys, which showed a good agreement with the activation energy calculated in this study. Besides, the experimental results correlate well with the LSW theory and its modified theories. A series of precipitation coarsening behaviour with different temperatures and times was observed in this study, which the particles coarsened at the expense of small ones and the size distribution became broader with the development of precipitation coarsening. Therefore, LSW and its modified theories is believed to be the optimal option of the numerical modelling of nickel-based alloys. Also, the relation between precipitation size with aging time was determined. According to the average slope, $0.29 \approx 1/3.4$, of Figure 5.1, which implied $(R)^{3.4} \propto t$. Therefore, a matrix diffusion-controlled coarsening mechanism was concluded[23, 56].

Alongside the static heat treatments, a series of dynamic hot compression tests were also designed and carried out. Chapter 4.3 presented the experimental process and results of these tests. Previous researches of thermal mechanical processing (TMP) and dynamic recrystallisation (DRX) of metals have been done previously[8, 57]. Similar works have also been conducted on nickel-based superalloy and Haynes 282 [6, 27, 58], e.g. Emil Eriksson et al.[27] designed hot compression tests at two different temperatures (1060°C and 1080°C) with three different strain rates ($5s^{-1}$, $0.5s^{-1}$ and $0.05s^{-1}$) on Haynes 282. Additionally, they found strain rate was the major governing factor for DRX at lower strain rate ($0.5s^{-1}$ and $0.05s^{-1}$) while temperature was the major factor at higher strain rate ($5s^{-1}$). Both DDRX and

CDRX were observed after hot compression. Hot deformation tests, such as Emil Eriksson's works, were mostly completed at relatively high temperatures. This inspired the investigation of hot deformation tests at relatively low temperatures. Tao Wang et al.[59] studied the TMP and DRX mechanism of GH4720Li nickel-based superalloy. They used the Arrhenius-type constitutive modelling to characterise the flow stress behaviour of this alloy and the activation energy of hot deformation was calculated. A discontinuous dynamic recrystallisation (DDRX) was recognised for this alloy under 1140°C tests. Same modelling method was attempted in this study, unfortunately, the activation energy cannot be obtained as a different strain-stress behaviour developed which is caused by the design of low temperature hot deformation tests. See Figure 5.11 (c) and (d), the curves do not exhibit constant slopes for further calculation. Hence, the activation energy at different strains for hot compression was not concluded in this study. Despite this, an interesting phenomenon was found in this study at 730°C and an early stage of 830°C. The flow stress is larger at 930°C and high strains at 830°C, but it acted differently at 730°C and low strains at 830°C. This phenomenon may be explained by the combination of work hardening and dynamic softening, and the adiabatic heating effect was also believed to be another non-negligible reason in this matter. It was also found that abnormal grain growth (AGG) occurred before DRX which led to an increase in maximum grain size. However, this was recorded by interception grain size measurement and EBSD maps. In order to validate this finding, higher resolution EBSD maps and computational grain size analysis would be necessary. Besides, only DDRX was observed in terms of the mechanism of DRX, where necklace nucleation was distributed at the boundary of large, elongated grains. This differed from the results reported in Emil Eriksson's works, which could potentially be explained by differences in temperature for deformation. The flow stress behaviour of Haynes 282 was also found to vary at different temperatures, likely due to a combination of work hardening and dynamic softening, as well as the adiabatic heating effect.



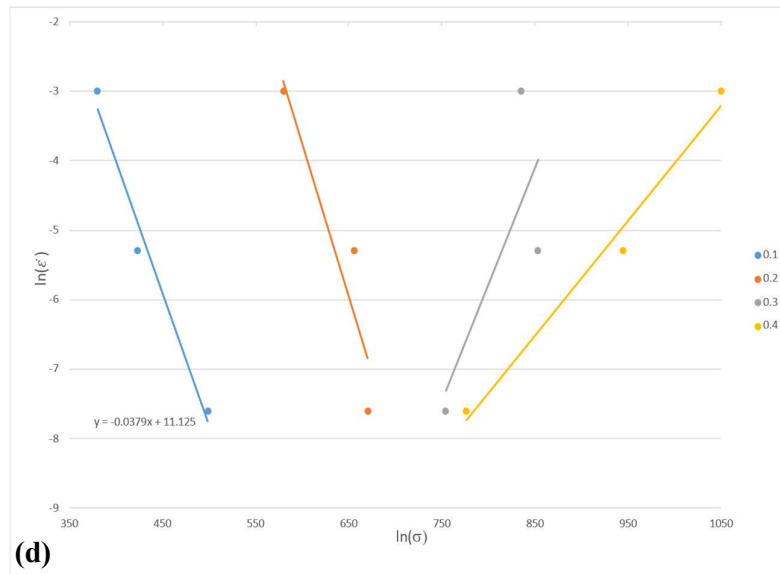


Figure 5.11 Diagrams represent $\ln(\dot{\epsilon}) - \ln(\sigma)$ and $\ln(\dot{\epsilon}) - \sigma$ at different strain (0.1, 0.2, 0.3 and 0.4) were generated using Arrhenius-type constitutive modelling, Figure (a) (b) were drawn out of 930°C tests, which showed a linear relationship between strain rate and true stress; Figure (c) (d) were drawn out of 830°C tests, and these curves cannot provide constant slopes for further activation energy calculation.

Chapter 6 Conclusions

Summarise, Haynes 282 superalloy possesses desirable advantages in the application for elevated temperature due to its combination of excellent creep strength, thermal stability, weldability, and fabricability. The research conducted in this study involved static heat treatments and dynamic hot compression tests to analyze and characterise the microstructure evolution, strain-stress behaviours, and recrystallization mechanisms observed in the Haynes 282 superalloy. Gaps in scientific research of Haynes 282 superalloy were filled, new interesting phenomena were reported and future works were suggested. The outcomes of static heat treatments can be concluded as follows.

- According to grain size analysis, abnormal grain growth (AGG) was observed to dominate the early stage of grain growth for aging temperatures at 730°C and 830°C. This was believed to be caused by the presence of secondary phase e.g., carbides. After AGG reached its critical level, normal grain growth (continuous grain growth, CGG) was observed causing an increased grain size in the later stage for aging temperatures at 730°C and 830°C. No significant AGG was observed for aging temperature at 930°C. On the one hand, higher temperature accelerated the grain growth process leading to a higher degree of coarsening. On the other hand, during 930°C aging, limited and unstable carbides present in the microstructure result in fewer nucleation cores. Consequently, CGG dominates grain growth behaviour in 930°C tests. A further EBSD analysis would be needed for the validation of the grain size distribution, so as to prove the grain growth mechanism proposed in this study.
- Fine spherical γ' dispersion was captured in standard treatment and the size distribution lay between 13.4nm-36.7nm with average particle size at 22.0nm. For the nine designed heat treatments, γ' size remained at tertiary level in 730°C and 830°C treatments while γ' evolved to secondary level in 930°C treatments. The precipitate coarsening

correlated well with Ostwald Ripening theory and the size distribution correlates well with modified LSW models. A diffusion-controlled coarsening mechanism which follows LSW theory is determined for Haynes 282 superalloy. And activation energy was calculated to be 238KJ/mol. TIDC (trans-interface diffusion-controlled) mechanism was not observed in this study.

In terms of dynamic hot compression tests, the deformation temperature was set lower than common hot compression tests for nickel-based superalloys. The main conclusions are listed below.

- Samples that underwent deformation at 730°C and 830°C with $0.05s^{-1}$ and $0.005s^{-1}$ strain rate exhibited predominantly elastic deformation. For tests at 930°C, regular stress-strain patterns were obtained. Nevertheless, for tests at 830°C, it was found that the flow stress acted differently, in which flow stress was larger at a lower strain rate in early stage of deformation, while it acted opposite in later stage. This is believed to be caused by the combination of low DRX temperature and low strain rate. The work hardening rate against true stress at 930°C with varying strain rates is presented. The σ_c values are determined to be 519.5MPa, 345.3MPa and 300.5MPa for strain rate of $0.05s^{-1}$, $0.005s^{-1}$ and $0.0005s^{-1}$, respectively. Moreover, it is found that the grain size obtained from tests at 930°C was much smaller than other samples, which was a result of more plastic deformation induced at higher temperatures. An increase in maximum grain size in the sample deformed at 830°C with $0.005s^{-1}$ strain rate was recorded. It is believed that it was caused by AGG, which occurred before DRX started. GOS maps provided clear grain evolution with respect to grain orientation throughout the testing process. The results showed that the recrystallization degree increases with the increase in temperature and the decrease in strain rate. Boundary serrations, sub-grains and a small amount of nucleation emerge at early stage of deformation, followed by necklace nucleation at grain boundaries indicating a DDRX mechanism. Lastly, GND tends to

inhabit grain boundaries and GND density increased with the development of work hardening and initial DRX. It is also found that GND is more sensitive to strain rate than deformation temperature.

Chapter 7 Future Work

The limitations and future works were listed below:

- Cooling process is also a nonnegligible factor that will affect grain growth. Therefore, heat treatments with different cooling rates would also be an interesting topic for Haynes 282. Also, the role of secondary phases in grain evolution needs to be investigated further by means of in-situ techniques. For example, high temperature in-situ SEM and EDS would be suggested. Moreover, further long-term aging under service temperature (649°C-927°C) would be suggested to investigate the performance of Haynes 282 superalloy[1–3]. In addition, EBSD techniques have been a popular method for grain size analysis[4–6]. This is not only because it provides more noticeable images but also because it provides size distribution both in length and area by post processing. A further EBSD analysis for the validation of the grain growth mechanism proposed in this study would be helpful.
- Although a strong relationship between precipitation size and aging parameters is concluded in this thesis, the coarsening mechanism for longer aging remains unknown for Haynes 282 superalloy. According to Yuting et al.[7], some Nickel-based superalloys such as Allvac 718 plus possess a mixed coarsening mechanism, which has diffusion-controlled coarsening (follows LSW theory) in early stage and Trans-Interface Diffusion-controlled (TIDC) in later stage[7]. Investigating further requires not only further heat treatments but also techniques like Atom Probe Tomography (APT) to determine atom distribution. This would be an interesting topic to continue which can be expected to find out the co-relationship between the two coarsening mechanisms.
- In terms of hot deformation testing, single-pass hot compression tests were applied in this study. However, multi-pass DRX is showing its advantages in the investigation of materials design[8,9]. Industrial Haynes 282 alloy possesses an inhomogeneous grain

distribution, research on multi-pass hot deformation may give a new idea to solve the problem. In addition, the deformation temperature in this study was relatively low thus leading to unusual stress-strain curves at 730°C and 830°C. Consequently, the activation energy calculation obtained via Arrhenius-type constitutive modelling[10] cannot work. Hence, further hot deformation at higher temperatures between 1000°C-1200°C is needed for the activation energy determination. Lastly, the DRX behaviour can be examined through many characterisation methods and analysis techniques. For example, TEM can be essential for GND analysis as it provides vital attributes in counting dislocation loops[4]. Once GNDs are identified, their density and distribution can be quantified using image analysis software.

References

Chapter 2

- [1] R. C. Reed, *The Superalloys Fundamentals and Applications*, Cambridge: Cambridge University, 2006.
- [2] J. H. Goldman and E. Wood, "Protective coatings," in *Superalloys II*, New York, 1987, pp. 359-384.
- [3] A. Pineau and S. Antolovich, "High temperature fatigue of nickel-base superalloys—a review with special emphasis on deformation modes and oxidation," *Eng. Fail. Anal.*, vol. 16(8), pp. 2668-2697, 2009.
- [4] M. Hardy, B. Zirbel, G. Shen and R. Shankar, "Developing damage tolerance and creep resistance in a high strength nickel alloy for disc applications," *Superalloys 2004*, pp. 83-90, 2004.
- [5] G. Liu, "The Effects of Microstructure and Microtexture Generated during Solidification on Deformation Micromechanism in IN713C Nickel-Based Superalloy," Swansea University, 2018.
- [6] A. Suzuki and T. Pollock, "High-temperature strength and deformation of γ/γ' two-phase Co–Al–W-base alloys," *Acta Mater.*, vol. 56(6), pp. 1288-1297, 2008.
- [7] M. J. Donachie and S. J. Donachie, *Superalloys: a technical guide*, ASM international, 2002.
- [8] D. Hull and D. J. Bacon, in *Introduction to Dislocation*, Fourth Ed., Butterworth-Heinemann, 1965, pp. 5-20.
- [9] A. Kelly and K. M. Knowles, *Crystallography and Crystal Defects*, Chichester, West Sussex, UK, 2012.
- [10] B. H. Kear, A. F. Giamei, J. M. Silcock and R. K. Ham, "Slip and climb processes in gamma prime precipitation hardened nickel-base alloys," *Scripta Metallurgica*, vol. 2, pp. 287-294, 1968.
- [11] B. H. Kear, A. Giamei and G. Leverant, "On intrinsic/extrinsic stacking fault pairs in the L12 lattice," *Scripta Metallurgica*, vol. 3, pp. 123-130, 1969.

- [12] M. Mughrabi, "Cyclic slip irreversibilities and the evolution of fatigued damage," *Metallurgical and Materials Transactions*, vol. 20, pp. 431-453, 2009.
- [13] J. Hyzak and I. Bernstein, "The effect of defects on the fatigue crack initiation process in two P/M superalloys: Part I. Fatigue origins," *Metall. Trans*, vol. A 13(1), pp. 33-43, 1982.
- [14] J. Hyzak and I. Bernstein, "The effect of defects on the fatigue crack initiation process in two P/M superalloys: Part II. Surface-subsurface transition," *Metall. Trans.*, vol. A 13(1), pp. 45-52, 1982.
- [15] E. S. Huron and P. G. Roth, "The influence of inclusions on low cycle fatigue life in a P/M nickel-base disk superalloy," *Superalloys*, pp. 359-368, 1996.
- [16] P. Lukáš and L. Kunz, "Specific features of high-cycle and ultra-high-cycle fatigue," *Fatigue & Fracture of Engineering Materials & Structures*, vol. 25(8-9), pp. 747-753, 2002.
- [17] U. Krupp, "Fatigue crack propagation in metals and alloys: microstructural aspects and modelling concepts," John Wiley & Sons, 2007.
- [18] M. Risbet, X. Feaugas, C. Guillemer-Neel and M. Clavel, "Use of atomic force microscopy to quantify slip irreversibility in a nickel-base superalloy," *Scripta Materialia*, vol. 49 (6), pp. 533-538, 2003.
- [19] P. Lukas and L. Kunz, "Role of persistent slip bands in fatigue," *Philosophical Magazine*, Vols. 21 (3-5), pp. 317-330, 2004.
- [20] S. Suresh, "Fatigue of materials," Cambridge University Press, Cambridge, 1991.
- [21] B. Larrouy, P. Villechaise, J. Cormier and O. Berteau, "Grain boundary–slip bands interactions: Impact on the fatigue crack initiation in a polycrystalline forged Ni-based superalloy," *Acta Mater*, vol. 99, pp. 325-336, 2005.
- [22] J. P. Poirier, "Creep of Crystals: High Temperature Deformation Processes in Metals, Ceramics and Minerals," Cambridge University Press, Cambridge, 1985.
- [23] J. Weertman, "Creep of indium, lead and some of their alloys," *Transactions of the Metallurgical Society of AIME*, vol. 218, pp. 207-218, 1960.
- [24] J. R. Weertman, "Mechanical properties, strongly temperature," John Wiley & Sons., New York, 1965.

- [25] T. B. Hopkins and B. E. Gibbons, "Creep behaviour and microstructure of Ni-Cr base alloys," *Metal Science*, vol. 18, pp. 273-280, 1984.
- [26] J. P. Dennison, R. J. Llewellyn and B. Wilshire, "The creep and fracture behaviour of some dilute nickel alloys at 500 and 600 °C," *Journal of the Institute of Metals*, vol. 94, pp. 130-134, 1966.
- [27] K. Kruger, "HAYNES 282 alloy," Haynes International, Inc., Kokomo, IN, United States, pp. 511-545.
- [28] Y. Yang and R. Thomas, "Microstructural evolution in cast Haynes 282 for applications in advanced power plants," *Advances on Materials Technology for Fossil Power Plants*, pp. 143-154, 2014.
- [29] L. Pike and S. Srivastava, "Oxidation behavior of wrought gamma-prime strengthened alloys," *Materials Science Forum*, vol. 595–598, p. 661–671, 2008.
- [30] Y. Wu, C. Li, X. Xia, H. Liang, Q. Qi and Y. Liu, "Precipitate coarsening and its effects on the hot deformation behavior of the recently developed γ' -strengthened superalloys," *Journal of Materials Science & Technology*, vol. 67, pp. 95-104, 2021.
- [31] Y. Yang, R. Thomson, R. Leese and S. Roberts, "Microstructural evolution in cast Haynes 282 for applications in advanced power plants," *Adv. Mater. Technol. Foss. Power Plants*, pp. 143-154, 2014.
- [32] I. Lifshitz and V. Slyozov, "The kinetics of precipitation from supersaturated solid solutions," *J. Phys. Chem. Solids*, vol. 39, no. 1-2, pp. 35-50, 1961.
- [33] A. Ardell, "The effect of volume fraction on particle coarsening: theoretical considerations," *Acta Mater*, vol. 20, pp. 61-71, 1972.
- [34] C. K. L. Davies, P. Nash and R. N. Stevens, "Precipitation in Ni-Co-Al alloys," *Acta Mater.*, vol. 15, pp. 1521-1532, 1980.
- [35] A. J. Ardell and V. Ozolins, "Trans-interface diffusion-controlled coarsening," *Nature Materials*, vol. 4, pp. 309-316, 2005.

- [36] Y. Wu, Y. Liu, C. Li, X. Xia, J. Wu and H. Li, "Coarsening behavior of γ' precipitates in the $\gamma'+\gamma$ area of a Ni₃Al-based alloy," *Journal of Alloys and Compounds*, vol. 771, pp. 526-533, 2019.
- [37] W. F. Smith, J. Hashemi and F. Presuel-Moreno, *Foundations of Materials Science and Engineering*, 4th ed., McGraw-Hill, 2006.
- [38] W. D. Callister, *Fundamentals of Materials Science and Engineering*, John Wiley & Sons, Inc, 2001.
- [39] D. A. Hanaor, W. Xu, M. Ferry and C. C. Sorrell, "Abnormal grain growth of rutile TiO₂ induced by ZrSiO₄," *Journal of Crystal Growth*, vol. 359, pp. 83-91, 2012.
- [40] S.-J. L. Kang, *Sintering: Densification, Grain Growth and Microstructure*, Elsevier Butterworth-Heinemann, 2005.
- [41] A. Bhattacharya, "Grain boundary velocity and curvature are not correlated in Ni polycrystals," vol. 374, no. 6564, pp. 189-193, 2021.
- [42] K. Huang and R. Logé, "A review of dynamic recrystallization phenomena in metallic materials," *Materials and Design*, vol. 111, pp. 548-574, 2016.
- [43] A. Dehghan-Manshadi, M. Barnett and P. Hodgson, "Hot Deformation and Recrystallization of Austenitic Stainless Steel: Part I. Dynamic Recrystallization," *Metallurgical and Materials Transactions A*, vol. 39, pp. 1359-1370, 2008.
- [44] D. Ponge and G. Gottstein, "Necklace formation during dynamic recrystallization: mechanisms and impact on flow behavior," *Acta Materialia*, vol. 46, no. 1, pp. 69-80, 1998.
- [45] M. Ohashi, T. Endo and T. Sakai, "Effect of Initial Grain Size on Dynamic Recrystallization of Pure Nickel," *J. Japan Inst. Metals*, , vol. 54, no. 4, pp. 435-441, 1990.
- [46] C. B. Carter and S. M. Holmes, "The stacking-fault energy of nickel," *The Philosophical Magazine: A Journal of Theoretical Experimental and Applied Physics*, vol. 35, no. 5, pp. 1161-1172, 1977.
- [47] E. Eriksson and M. H. Colliander, "Dynamic and Post-Dynamic Recrystallization of Haynes 282," *Metals*, vol. 11, no. 122, 2021.

- [48] D. P. Pope and S. S. Ezz, “Mechanical properties of Ni₃Al and nickel-base alloys with high volume fraction of gamma prime,” *International Metals Reviews*, vol. 29, no. 1, pp. 136-167, 1984.
- [49] W. D. Jenkins, T. G. Digges and C. R. Johnson, “Creep of High-Purity Nickel,” *Journal of Research of the National Bureau of Standards*, vol. 53, no. 6, pp. 329-352, 1954.
- [50] R. Pei, S. Korte-Kerzel and T. Al-Samman, “Normal and abnormal grain growth in magnesium: Experimental observations and simulations,” *Journal of Materials Science & Technology*, vol. 20, no. 1, pp. 257-270, 2020.
- [51] L. M. Pike, “HAYNES® 282™ Alloy: A New Wrought Superalloy Designed for Improved Creep Strength and Fabricability,” *ASME Turbo Expo 2006: Power for Land, Sea, and Air*, vol. 4, pp. 1031-1039, 2006.
- [52] A. H. Clauer and B. A. Wilcox, “Steady-state creep of dispersion-strengthened,” *Metal Science*, vol. 1, pp. 86-90, 1967.

Chapter 3

- [1] G. F. Vander Voort, G. M. Lucas, and E. P. Manilova, “Metallography and Microstructures of Heat-Resistant Alloys,” *Metallogr. Microstruct.*, vol. 9, pp. 820–859, 2018, doi: 10.31399/asm.hb.v09.a0003737.
- [2] A. B. Parsa, M. Ramsperger, A. Kostka, C. Somsen, C. Körner, and G. Eggeler, “Transmission electron microscopy of a CMSX-4 Ni-base superalloy produced by selective electron beam melting,” *Metals (Basel)*, vol. 6, no. 11, pp. 1–17, 2016, doi: 10.3390/met6110258.
- [3] E. R. Davies, *Introduction to texture analysis*, Second. CRC press, Boca Raton, FL, 2008. doi: 10.1142/9781848161160_0001.
- [4] T. Maitland and S. Sitzman, “Electron Backscatterd Diffraction (EBSD) Technique and Materials Characterization Examples,” in *Scanning Microscopy for Nanotechnology : Techniques and Applications*, *Scanning Microsc. Nanotechnol. Tech. Appl.*, Springer, New York, NY, 2007, pp. 41–76.

- [5] D. B. Williams and C. B. Carter, “Transmission Electron Microscopy a Textbook for Materials Science”. 2009.
- [6] George F. Vander Voort, “Grain Size Measurement,” in Practical applications of quantitative metallography, J. H. S. J. J.L. McCall, Ed. American Society for Testing and Materials, Philadelphia, USA, 1984, pp. 85–131. doi: 10.1520/STP30216S.
- [7] P. Ibañez, “Grain Size Astm E112,” ingintegral.
https://www.ingintegral.com/reporte_aplicacion/ASTM E 112 E-book_EN.pdf (accessed Jun. 01, 2022).
- [8] “Grain Size Analysis and Evaluation.”
<https://www.keyence.co.uk/ss/products/microscope/vhx-casestudy/automobile/grain-size.jsp> (accessed Jun. 01, 2022).
- [9] A. D. Rollett, “Texture, Microstructure & Anisotropy,” 2014.
<https://slideplayer.com/slide/3854543/>

Chapter 4

- [1] K. Wang, D. Wang, and F. Han, “Effect of crystalline grain structures on the mechanical properties of twinning-induced plasticity steel,” *Acta Mech. Sin. Xuebao*, vol. 32, no. 1, pp. 181–187, 2016, doi: 10.1007/s10409-015-0513-7.
- [2] W. Ostwald, *Lehrbuch der Allgemeinen Chemie*. Leipzig : Engelmann, 1885.
- [3] W. Ostwald, “Studien über die Bildung und Umwandlung fester Körper,” *Zeitschrift für Phys. Chemie*, vol. 22, pp. 289–330, 1897.
- [4] D. D. Chen, Y. C. Lin, Y. Zhou, M. S. Chen, and D. X. Wen, “Dislocation substructures evolution and an adaptive-network-based fuzzy inference system model for constitutive behavior of a Ni-based superalloy during hot deformation,” *J. Alloys Compd.*, vol. 708, pp. 938–946, 2017, doi: 10.1016/j.jallcom.2017.03.029.
- [5] X. Yuan and L. Chen, “Hot deformation at elevated temperature and recrystallization behavior of a high manganese austenitic TWIP steel,” *Acta Met.*, vol. 51, p. 651, 2015.
- [6] Y. Xu, L. Hu, and Y. Sun, “Deformation behaviour and dynamic recrystallization of AZ61 magnesium alloy,” *Alloy. Compd*, vol. 580, p. 262, 2013.

- [7] B. Li, Y. Du, Z. Chu, W. Zhou, and X. Yang, “Research on dynamic recrystallization behavior of Ni[sbnd]Fe[sbnd]Cr based alloy,” *Mater. Charact.*, vol. 169, p. 1175, 2020, doi: 10.1016/j.matchar.2020.110653.
- [8] X. Q. Yin et al., “Mechanism of continuous dynamic recrystallization in a 50Ti-47Ni-3Fe shape memory alloy during hot compressive deformation,” *J. Alloys Compd.*, vol. 693, no. 426, pp. 426–431, 2017, doi: 10.1016/j.jallcom.2016.09.228.
- [9] J. Yu, Z. Zhang, Q. Wang, X. Yin, J. Cui, and H. Qi, “Dynamic recrystallization behavior of magnesium alloys with LPSO during hot deformation,” *J. Alloys Compd.*, vol. 704, no. 382, pp. 382–389, 2017, doi: 10.1016/j.jallcom.2017.01.321.
- [10] Y. X. Liu, Y. C. Lin, and Y. Zhou, “2D cellular automaton simulation of hot deformation behavior in a Ni-based superalloy under varying thermal-mechanical conditions,” *Mater. Sci. Eng. A*, vol. 691, pp. 88–99, 2017, doi: 10.1016/j.msea.2017.03.039.
- [11] Y. C. Lin, S. C. Luo, L. X. Yin, and J. Huang, “Microstructural evolution and high temperature flow behaviors of a homogenized Sr-modified Al-Si-Mg alloy,” *J. Alloys Compd.*, vol. 739, pp. 590–599, 2018, doi: 10.1016/j.jallcom.2017.12.278.

Chapter 5

- [1] W. F. Smith and J. Hashemi, *Foundations of Materials Science and Engineering (SI Units)*, 4th ed. McGraw-Hill, 2011. [Online]. Available: <http://books.google.com/books?id=2pVbSAAACAAJ&pgis=1>
- [2] W. J. Harrison, “Creep of Non-Ferrous Metals,” in *Encyclopedia of Materials: Metals and Alloys*, Elsevier, 2021, pp. 494–504. doi: 10.1016/B978-0-12-819726-4.00085-5.
- [3] W. J. Harrison, M. T. Whittaker, and C. Deen, “Creep behaviour of waspaloy under nonconstant stress and temperature,” *Energy Mater. Mater. Sci. Eng. Energy Syst.*, vol. 8, no. 3, pp. 323–326, 2013, doi: 10.1179/1433075X13Y.0000000137.
- [4] D. Hanaor, W. Xu, M. Ferry, and C. C. Sorrell, “Abnormal grain growth of rutile TiO₂ induced by ZrSiO₄,” *J. Cryst. Growth*, vol. 359, no. 1, pp. 83–91, 2012, doi: 10.1016/j.jcrysgro.2012.08.015.

- [5] A. Bhattacharya et al., “Grain boundary velocity and curvature are not correlated in Ni polycrystals,” *Science* (80-.), vol. 374, no. 6564, pp. 189–193, 2021, doi: 10.1126/science.abj3210.
- [6] E. Eriksson, J. Andersson, and M. Hörnqvist Colliander, “The Effect of Grain Boundary Carbides on Dynamic Recrystallization During Hot Compression of Ni-Based Superalloy Haynes 282 TM,” *Metall. Mater. Trans. A Phys. Metall. Mater. Sci.*, vol. 53, no. 1, pp. 29–38, 2022, doi: 10.1007/s11661-021-06524-x.
- [7] P. Podany, Z. Novy, and J. Dlouhy, “Recrystallization behaviour of a nickel-based superalloy,” *Mater. Tehnol.*, vol. 50, no. 2, pp. 199–205, 2016, doi: 10.17222/mit.2014.163.
- [8] K. Huang and R. E. Logé, “A review of dynamic recrystallization phenomena in metallic materials,” *Materials and Design*, vol. 111, pp. 548–574, 2016. doi: 10.1016/j.matdes.2016.09.012.
- [9] C. B. Carter and S. M. Holmes, “The stacking-fault energy of nickel,” *Philos. Mag.*, vol. 35, no. 5, pp. 1161–1171, 1977, doi: 10.1080/14786437708232942.
- [10] E. R. Davies, *Introduction to texture analysis*. 2008. doi: 10.1142/9781848161160_0001.
- [11] V. Randle, P. R. Rios, and Y. Hu, “Grain growth and twinning in nickel,” *Scr. Mater.*, vol. 58, no. 2, pp. 130–133, 2008, doi: 10.1016/j.scriptamat.2007.09.016.
- [12] Roger C. Reed, *The superalloys Fundamentals and Applications*, First edit. 2006.
- [13] M. J. Donachie and S. J. Donachie, *SUPERALLOYS Second Edition*. 2002.
- [14] D. Hull and D. J. Bacon, *Introduction to Dislocations*, 4th ed. Butterworth-Heinemann, 2011. doi: 10.1016/C2009-0-64358-0.
- [15] Haynes International, “HAYNES® 282® alloy.”
- [16] J. Andersson, G. Sjöberg, and M. Chaturvedi, “Hot ductility study of Haynes® 282® superalloy,” *7th Int. Symp. Superalloy 718 Deriv. 2010*, vol. 2, pp. 539–554, 2010, doi: 10.1002/9781118495223.ch41.
- [17] Y. Yang, R. C. Thomson, R. M. Leese, and S. Roberts, “Microstructural evolution in cast Haynes 282 for application in advanced power plants,” *Adv. Mater. Technol. Foss. Power Plants - Proc. from 7th Int. Conf.*, pp. 143–154, 2014.

- [18]M. Lifshitz and V. V. Slyozov, “The kinetics of precipitation from supersaturated solid solutions,” J. Phys. Chem. Solids, vol. 19, no. 1–2, pp. 35–50, 1961.
- [19]A. Baldan, “Progress in Ostwald ripening theories and their applications to nickel-base superalloys. Part I: Ostwald ripening theories,” J. Mater. Sci., vol. 37, pp. 2171–2202, 2002.
- [20]C. Wagner, “Theorie der Alterung von Niederschlägen durch Umlösen (Ostwald-Reifung),” Zeitschrift für Elektrochemie, Berichte der Bunsengesellschaft für Phys. Chemie, vol. 65, no. 7–8, pp. 581–591, 1961, doi: 10.1002/bbpc.19610650704.
- [21]A. Ardell, “The effect of volume fraction on particle coarsening: theoretical considerations,” Acta Mater., vol. 20, pp. 61–71, 1972, [Online]. Available: [https://doi.org/10.1016/0001-6160\(72\)90114-9](https://doi.org/10.1016/0001-6160(72)90114-9)
- [22]C. K. L. Davies, P. Nash, and R. N. Stevens, “Precipitation in Ni-Co-Al alloys - Part 1 continuous precipitation,” J. Mater. Sci., vol. 15, no. 6, pp. 1521–1532, 1980, doi: 10.1007/BF00752134.
- [23]Y. Wu, C. Li, X. Xia, H. Liang, Q. Qi, and Y. Liu, “Precipitate coarsening and its effects on the hot deformation behavior of the recently developed γ' -strengthened superalloys,” J. Mater. Sci. Technol., vol. 67, pp. 95–104, 2021, doi: 10.1016/j.jmst.2020.06.025.
- [24]S. Zhao, X. Xie, G. D. Smith, and S. J. Patel, “Gamma prime coarsening and age-hardening behaviors in a new nickel base superalloy,” Mater. Lett., vol. 58, no. 11, pp. 1784–1787, 2004, doi: 10.1016/j.matlet.2003.10.053.
- [25]H. Jieshan, G. Jianting, and Z. Lanzhang, “Influence of γ' Phase Coarsening on Tensile Properties during Long-Term Aging Process of K44 Nickel-Based Superalloy,” Acta Metall. Sin., vol. 42, no. 5, pp. 481–486, 2006.
- [26]R. D. Doherty et al., “Current issues in recrystallization: A review,” Mater. Sci. Eng. A, vol. 238, no. 2, pp. 219–274, 1997, doi: 10.1016/S0921-5093(97)00424-3.
- [27]E. Eriksson, “Dynamic and Post-Dynamic Recrystallization of Haynes 282 below the Secondary Carbide Solvus,” Metals (Basel), vol. 11, no. 122, 2021, [Online]. Available: <https://doi.org/10.3390/met11010122>

- [28] T. Sakai, A. Belyakov, R. Kaibyshev, H. Miura, and J. J. Jonas, “Dynamic and post-dynamic recrystallization under hot, cold and severe plastic deformation conditions,” *Prog. Mater. Sci.*, vol. 60, no. 1, pp. 130–207, 2014, doi: 10.1016/j.pmatsci.2013.09.002.
- [29] S. Gourdet and F. Montheillet, “Particle stimulated nucleation during dynamic and metadynamic recrystallisation of Ni-30%Fe-Nb-C alloy,” *Mater. Sci. Eng.*, vol. 283(1), pp. 274–288, 2017, [Online]. Available: [https://doi.org/10.1016/S0921-5093\(00\)00733-4](https://doi.org/10.1016/S0921-5093(00)00733-4)
- [30] S. L. Semiatin et al., “Plastic flow and microstructure evolution during thermomechanical processing of a pm nickel-base superalloy,” *Metall. Mater. Trans. A Phys. Metall. Mater. Sci.*, vol. 44, no. 6, pp. 2778–2798, 2013, doi: 10.1007/s11661-013-1675-1.
- [31] Y.C. Lin and X. M. Chen, “A critical review of experimental results and constitutive descriptions for metals and alloys in hot working,” *Materials (Basel)*, vol. 32(4), pp. 1733–1759, 2011, [Online]. Available: <https://doi.org/10.1016/j.matdes.2010.11.048>
- [32] L. E. Murr, *Interfacial phenomena in metals and alloys*. United States, 1975. [Online]. Available: <https://www.osti.gov/biblio/4146281>
- [33] J. Zhao, H. Ding, W. Zhao, M. Huang, D. Wei, and Z. Jiang, “Modelling of the hot deformation behaviour of a titanium alloy using constitutive equations and artificial neural network,” *Comput. Mater. Sci.*, vol. 92, pp. 47–56, 2014, doi: 10.1016/j.commatsci.2014.05.040.
- [34] P. Yang, C. Liu, Q. Guo, and Y. Liu, “Variation of activation energy determined by a modified Arrhenius approach: Roles of dynamic recrystallization on the hot deformation of Ni-based superalloy,” *J. Mater. Sci. Technol.*, vol. 72, pp. 162–171, 2021, doi: 10.1016/j.jmst.2020.09.024.
- [35] Y. C. Lin et al., “EBSD study of a hot deformed nickel-based superalloy,” *J. Alloys Compd.*, vol. 640, pp. 101–113, 2015, doi: 10.1016/j.jallcom.2015.04.008.
- [36] X. Q. Yin et al., “Mechanism of continuous dynamic recrystallization in a 50Ti-47Ni-3Fe shape memory alloy during hot compressive deformation,” *J. Alloys Compd.*, vol. 693, no. 426, pp. 426–431, 2017, doi: 10.1016/j.jallcom.2016.09.228.

- [37]Y. Xu, L. Hu, and Y. Sun, “Deformation behaviour and dynamic recrystallization of AZ61 magnesium alloy,” *Alloy. Compd.*, vol. 580, p. 262, 2013.
- [38]H. Gao and Y. Huang, “Geometrically necessary dislocation and size-dependent plasticity,” *Scr. Mater.*, vol. 48, no. 2, pp. 113–118, 2003, doi: 10.1016/S1359-6462(02)00329-9.
- [39]S. Biroasca et al., “The dislocation behaviour and GND development in a nickel based superalloy during creep,” *Int. J. Plast.*, vol. 118, no. July 2018, pp. 252–268, 2019, doi: 10.1016/j.ijplas.2019.02.015.
- [40]K. L. Kruger, HAYNES 282 alloy. Elsevier Ltd, 2017. doi: 10.1016/B978-0-08-100552-1.00015-4.
- [41]B. Lim et al., “Additively manufactured Haynes-282 monoliths containing thin wall struts of varying thicknesses,” *Addit. Manuf.*, vol. 59, no. PA, p. 103120, 2022, doi: 10.1016/j.addma.2022.103120.
- [42]A. S. Shaikh, F. Schulz, K. Minet-Lallemant, and E. Hryha, “Microstructure and mechanical properties of Haynes 282 superalloy produced by laser powder bed fusion,” *Materials Today Communications*, vol. 26. 2021. doi: 10.1016/j.mtcomm.2021.102038.
- [43]J. Boswell, J. Jones, N. Barnard, D. Clark, M. Whittaker, and R. Lancaster, “The effects of energy density and heat treatment on the microstructure and mechanical properties of laser additive manufactured Haynes 282,” *Mater. Des.*, vol. 205, p. 109725, 2021, doi: 10.1016/j.matdes.2021.109725.
- [44]K. A. Unocic, M. M. Kirka, E. Cakmak, D. Greeley, A. O. Okello, and S. Dryepondt, “Evaluation of additive electron beam melting of haynes 282 alloy,” *Mater. Sci. Eng. A*, vol. 772, 2020, doi: 10.1016/j.msea.2019.138607.
- [45]R. Otto, V. Brøtan, A. S. Azar, and O. Åsebø, “Processing of Haynes® 282® alloy by laser powder bed fusion technology,” in *Proceedings of the TMS 2019 148th Annual Meeting & Exhibition Supplemental Proceedings*, 2019, pp. 503–510. doi: 10.1007/978-3-030-05861-6_47.

- [46]C. Joseph, C. Persson, and M. Hörnqvist Colliander, “Influence of heat treatment on the microstructure and tensile properties of Ni-base superalloy Haynes 282,” *Mater. Sci. Eng. A*, vol. 679, no. June 2016, pp. 520–530, 2017, doi: 10.1016/j.msea.2016.10.048.
- [47]K. Y. Shin, J. H. Kim, M. Turner, B. O. Kong, and H. U. Hong, “Effects of heat treatment on the microstructure evolution and the high-temperature tensile properties of Haynes 282 superalloy,” *Mater. Sci. Eng. A*, vol. 751, no. February, pp. 311–322, 2019, doi: 10.1016/j.msea.2019.02.054.
- [48]G. F. Vander Voort, “Grain Size Measurement Methods: A Review and Comparison,” *Microscopy and Microanalysis*, vol. 19, no. S2, pp. 1760–1761, 2013.
- [49]P. Ibañez, “Grain Size Astm E112,” *ingintegral*. https://www.ingintegral.com/reporte_aplicacion/ASTM E 112 E-book_EN.pdf (accessed Jun. 01, 2022).
- [50]M. J. Anderson et al., “On the modelling of precipitation kinetics in a turbine disc nickel based superalloy,” *Acta Mater.*, vol. 191, pp. 81–100, 2020, doi: 10.1016/j.actamat.2020.03.058.
- [51]M. N. J. Lapin, M. Gebura, T. Pelachová, “Coarsening kinetics of cuboidal γ precipitates in single crystal nickel base.pdf,” *Kov. Mater*, vol. 46, pp. 313–322, 2008.
- [52]M. G. Fahrman and D. A. Metzler, “Simulation of γ' Precipitation Kinetics in a Commercial Ni-Base Superalloy,” *Jom*, vol. 68, no. 11, pp. 2786–2792, 2016, doi: 10.1007/s11837-016-2097-5.
- [53]R. Nozato, T. Morigaki, and H. Tsubakino, “Kinetics of Precipitation of Nickel From Lead-Nickel Solid Solution,” *Trans. Japan Inst. Met.*, vol. 24, no. 1, pp. 18–23, 1983, doi: 10.2320/matertrans1960.24.18.
- [54]J. A. Hawk, T. Le Cheng, J. S. Sears, P. D. Jablonski, and Y. H. Wen, “Gamma Prime Stability in Haynes 282: Theoretical and Experimental Considerations,” *J. Mater. Eng. Perform.*, vol. 24, no. 11, pp. 4171–4181, 2015, doi: 10.1007/s11665-015-1711-y.

- [55] K. Vattappara, V. A Hosseini, C. Joseph, F. Hanning, and J. Andersson, “Physical and thermodynamic simulations of gamma-prime precipitation in Haynes® 282® using arc heat treatment,” *J. Alloys Compd.*, vol. 870, p. 159484, 2021, doi: 10.1016/j.jallcom.2021.159484.
- [56] A. J. Ardell, “Trans-interface-diffusion-controlled coarsening of γ' particles in Ni–Al alloys: commentaries and analyses of recent data,” *J. Mater. Sci.*, vol. 55, pp. 588–610, 2020.
- [57] X. Yuan and L. Chen, “Hot deformation at elevated temperature and recrystallization behavior of a high manganese austenitic TWIP steel,” *Acta Met.*, vol. 51, p. 651, 2015.
- [58] T. Wang, Z. Wan, Y. Sun, Z. Li, Y. Zhang, and L. Hu, “Dynamic Softening Behavior and Microstructure Evolution of Nickel Base Superalloy,” *Jinshu Xuebao/Acta Metall. Sin.*, vol. 54, no. 1, pp. 83–92, 2018, doi: 10.11900/0412.1961.2017.00241.
- [59] T. Wang, Z. Wan, Y. Sun, Z. Li, Y. Zhang, and L. Hu, “Dynamic Softening Behavior and Microstructure Evolution of Nickel Base Superalloy,” *Jinshu Xuebao/Acta Metallurgica Sinica*, vol. 54, no. 1, pp. 83–92, 2018. doi: 10.11900/0412.1961.2017.00241.

Chapter 7

- [1] K. L. Kruger, HAYNES 282 alloy. Elsevier Ltd, 2017. doi: 10.1016/B978-0-08-100552-1.00015-4.
- [2] V. Randle, P. R. Rios, and Y. Hu, “Grain growth and twinning in nickel,” *Scr. Mater.*, vol. 58, no. 2, pp. 130–133, 2008, doi: 10.1016/j.scriptamat.2007.09.016.
- [3] K. Y. Shin, J. H. Kim, M. Turner, B. O. Kong, and H. U. Hong, “Effects of heat treatment on the microstructure evolution and the high-temperature tensile properties of Haynes 282 superalloy,” *Mater. Sci. Eng. A*, vol. 751, no. February, pp. 311–322, 2019, doi: 10.1016/j.msea.2019.02.054.
- [4] S. Biroasca et al., “The dislocation behaviour and GND development in a nickel based superalloy during creep,” *Int. J. Plast.*, vol. 118, no. July 2018, pp. 252–268, 2019, doi: 10.1016/j.ijplas.2019.02.015.
- [5] Y. C. Lin, S. C. Luo, L. X. Yin, and J. Huang, “Microstructural evolution and high temperature flow behaviors of a homogenized Sr-modified Al-Si-Mg alloy,” *J. Alloys Compd.*, vol. 739, pp. 590–599, 2018, doi: 10.1016/j.jallcom.2017.12.278.

- [6] D. S. Weaver and S. L. Semiatin, "Recrystallization and grain-growth behavior of a nickel-base superalloy during multi-hit deformation," *Scr. Mater.*, vol. 57, no. 11, pp. 1044–1047, 2007, doi: 10.1016/j.scriptamat.2007.07.033.
- [7] Y. Wu, C. Li, X. Xia, H. Liang, Q. Qi, and Y. Liu, "Precipitate coarsening and its effects on the hot deformation behavior of the recently developed γ' -strengthened superalloys," *J. Mater. Sci. Technol.*, vol. 67, pp. 95–104, 2021, doi: 10.1016/j.jmst.2020.06.025.
- [8] G. He, F. Liu, L. Huang, Z. Huang, and L. Jiang, "Controlling grain size via dynamic recrystallization in an advanced polycrystalline nickel base superalloy," *J. Alloys Compd.*, vol. 701, pp. 909–919, 2017, doi: 10.1016/j.jallcom.2017.01.179.
- [9] B. Fang et al., "Critical strain and models of dynamic recrystallization for FGH96 superalloy during two-pass hot deformation," *Mater. Sci. Eng. A*, vol. 593, pp. 8–15, 2014, doi: 10.1016/j.msea.2013.11.016.
- [10] T. Wang, Z. Wan, Y. Sun, Z. Li, Y. Zhang, and L. Hu, "Dynamic Softening Behavior and Microstructure Evolution of Nickel Base Superalloy," *Jinshu Xuebao/Acta Metallurgica Sinica*, vol. 54, no. 1, pp. 83–92, 2018. doi: 10.11900/0412.1961.2017.00241.